Defect energies, band alignments, and charge carrier recombination in polycrystalline Cu(In,Ga)(Se,S)$_2$ alloys

DISSERTATION

zur Erlangung des akademischen Grades

Doctor rerum naturalium

(Dr. rer. nat.)

genehmigt von

der Fakultät Mathematik und Naturwissenschaften

der Technische Universität Dresden

von

Mircea Cassian Turcu

geboren am 29. September 1970 in Temesburg, Rumänien

Acknowledgments

I would particularly like to express my gratitude to my supervisor Dr. U. Rau, leader of the device analysis group at the Institute for Physical Electronics (*ipe*), University of Stuttgart, for his continued guidance, patient advice, and valuable assistance throughout this work.

I would like to thank Prof. Dr. K. Leo, head of the Institute of Applied Photophysics, Technical University of Dresden, for initiating this work, for supplying the framework, and for help in many situations.

I also like to thank Dr. H. W. Schock for many useful discussions and ideas regarding my work, for constructive criticism, and for support within the compound semiconductors group which he leads at the *ipe*.

I am very grateful to Prof. Dr. J. H. Werner, head of the *ipe*, for encouraging my work and for the access to all facilities at the *ipe*.

I am very thankful to Prof. Dr. I. Muscutariu from West University of Timisoara, Romania, for help in different situations, for support and for encouragement.

I thank I. Kötschau (*ipe*) for supplying an important part of the samples used in this work and O. Pakma (Faculty of Arts and Science, University of Mugla, Turkey) for together performing some measurements. I also thank my colleagues at the *ipe* for fruitful collaboration and for help during my work.

I am indebted to my family for continuous support, encouragement, and unconditioned love without which this work would not have been possible.

Table of contents

Symbols and abbreviations

ac	alternating current
AS	admittance spectroscopy
b_V, b_C, b_g,	bowing coefficient of valence/conduction band edge, of bandgap energy
C	heterojunction capacitance
CNL	charge neutrality level
CV	capacitance-voltage
D(E)	energetic distribution of defects in the band gap
D_e	diffusion constant for electrons
DAP	donor-acceptor pair
DLTS	deep level transient spectroscopy
DME	dielectric midpoint energy
E_A, E_a	thermal activation energy of defects, of recombination
E_{BP}	branch point energy
E_{dg}	dielectric gap energy
E_F	Fermi level energy position
E_g	band gap energy
E_{pin}^{n}, E_{pin}^{p}	*n*-type and *p*-type doping pinning levels
EQE	external quantum efficiency
e_T	emission rate of traps
E_T	bulk defect level of electronic transition N_2
E_V, E_C	valence and conduction band edges
E_{00}	tunneling energy
f	frequency of the electrical signal
f_i	inflexion frequency of the capacitance spectra
FF	fill factor
FWHM	full width at half maximum
h	Planck constant, 6.62617×10^{-34} J·s ($\hbar = h/2\pi$)
$\hbar\omega$	emitted photon energy (photoluminescence)
I	emitted photoluminescence intensity

j_r, j_{SC}	recombination current density, short circuit current density
j_0	reverse saturation current or reverse saturation current density
JV	current-voltage
k	wavevector
k_B	Boltzmann constant, 1.38066×10^{-23} J/K
L_e	diffusion length for electrons
m_e, m_h, m_0	electron and hole effective mass, electron rest mass
m^*	effective tunneling mass
N_A	doping density
N_v, N_c	effective density of states in the valence and conduction band
n_{id}	ideality factor
N_1, N_2	electronic transition detected by AS in chalcopyrites
N_T	concentration of the bulk acceptor N_2
PL	photoluminescence
P	excitation power (photoluminescence)
q	elementary charge, 1.60218×10^{-19} C
s, p, sp^3	atomic orbitals and hybrids
S_{if}	interface recombination velocity for holes
T	absolute temperature
V	applied voltage
V_{bi}	built-in voltage
V_{OC}	open circuit voltage
v_{th}	thermal velocity of charge carriers
w	space charge width
x	Ga/(Ga+In) ratio of Cu(In,Ga)(Se,S)$_2$ alloys
y	S/(S+Se) ratio of Cu(In,Ga)(Se,S)$_2$ alloys
χ	electron affinity
ΔE_F^{if}	energy distance $E_C - E_F$ at the CdS/absorber interface
ΔE_V, ΔE_C	valence and conduction band offset between bulk chalcopyrite alloys
ΔE_V^{if}, ΔE_C^{if}	valence and conduction band offset at the CdS/absorber interface
Δ_T	shift of PL peak energy under increasing temperature
Δ_P	shift of PL peak energy under increasing excitation power
ϵ_d	dangling bond energy

$\epsilon_s,\ \epsilon_p$	p-state, s-state atomic orbital energy
ε_s	static dielectric constant
ε_0	vacuum dielectric constant, 8.85418×10^{-14} F/cm
ξ_0	temperature-independent pre-exponential factor of inflexion frequency
ϕ_b^p	hole barrier at the CdS/absorber interface
$\phi_n,\ \phi_p$	Schottky barrier height at metal/n-type or metal/p-type semiconductor
ϕ_m	metal work function
φ_0	energy position of the charge neutrality level
η	solar cell efficiency
λ	wavelength
σ_p	thermal capture cross section of defects
ω	angular frequency

Abstract

The polycrystalline Cu(In,Ga)(Se,S)$_2$ chalcopyrite alloys provide absorber materials for the to date most efficient thin film solar cell technology. Thin film ZnO/CdS/chalcopyrite solar cells are of considerable interest for photovoltaics due to low cost, potential for up-scaling, radiation hardness, long term stability, high flexibility, low weight, and high conversion efficiencies. The usage of wide-gap Cu(In$_{1-x}$Ga$_x$)(Se$_{1-y}$S$_y$)$_2$ alloys with high Ga and/or S content is desirable when aiming towards high open circuit voltage devices. However, solar cells based on wide-gap Cu-chalcopyrites generally deliver a significantly lower device performance compared to the record devices. It is still unclear whether this trend results from high defect densities of wide-gap material, from less favorable band offsets at the CdS/chalcopyrite interface, or from a change in the recombination mechanism upon alloying CuInSe$_2$ with high contents of Ga and/or S.

This work investigates the defect energies, band alignments, charge carrier recombination, and Fermi level pinning in polycrystalline Cu(In$_{1-x}$Ga$_x$)(Se$_{1-y}$S$_y$)$_2$ chalcopyrite thin films and the interrelationship with the alloy composition.

Photoluminescence spectroscopy of Cu-poor Cu(In,Ga)(Se,S)$_2$ layers generally shows broad emission lines involving donor-acceptor pair recombination, which seems to dominate the radiative recombination in the composition range under investigation. The photoluminescence maxima shift towards higher energies under decreasing temperature or under increasing excitation power.

Admittance spectroscopy of Cu-poor ZnO/CdS/Cu(In,Ga)(Se,S)$_2$ chalcopyrite devices shows that the activation energies of the dominant defect distributions involving donors at the CdS/absorber interface and deep acceptors in the chalcopyrite bulk, increase upon alloying CuInSe$_2$ with S. Following a procedure applied to III-V, II-VI and IV-IV semiconductor alloys, the band alignments within the Cu(In$_{1-x}$Ga$_x$)(Se$_{1-y}$S$_y$)$_2$ system are determined using the energy position of the bulk acceptor state as a reference. However, an intrinsic defect is chosen here as invariant and not an extrinsic impurity level like for other semiconductor systems. The band gap enlargement under Ga alloying is accommodated almost exclusively in the rise of the conduction band edge, whereas the increase of band gap upon alloying with S is shared between comparable valence and conduction band offsets. The extrapolated band

discontinuities $\Delta E_V(CuInSe_2/CuInS_2) = -0.23$ eV, $\Delta E_C(CuInSe_2/CuInS_2) = 0.21$ eV, $\Delta E_V(CuInSe_2/CuGaSe_2) = 0.036$ eV, and $\Delta E_C(CuInSe_2/CuGaSe_2) = 0.7$ eV are in good agreement with theoretical predictions. The data indicate that a bulk reference level exists in the $Cu(In_{1-x}Ga_x)(Se_{1-y}S_y)_2$ semiconductors which sets the band structure on a common energy scale, thus establishing the natural band lineups within the alloy system automatically.

Current-voltage analysis of Cu-poor $ZnO/CdS/Cu(In,Ga)(Se,S)_2$ devices reveals recombination barriers which follow the band gap energy of the absorber irrespective of alloy composition, as expected for dominant recombination in the chalcopyrite bulk. In turn, the recombination at the active junction interface prevails in Cu-rich devices which display substantially smaller barriers when compared to the band gap energy of the absorber. The contribution of tunneling determined from current-voltage and capacitance-voltage analysis is substantially enhanced under Cu-excess. The present results indicate that the Cu-stoichiometry is the driving compositional parameter for the charge carrier recombination in the chalcopyrite heterojunctions under investigations.

The Fermi level position at the $CdS/Cu(In,Ga)(Se,S)_2$ interface is determined from the energetic depth of interface donors relative to the conduction band in Cu-poor alloys, and from the interface recombination barrier with respect to the valence band in Cu-rich alloys. The results show that irrespective of changes in the Cu-stoichiometry, the interface Fermi energy position shifts upward towards the conduction band upon increasing Ga content, and remains at a relatively low value in the band gap under anion S/Se alloying.

1. Introduction

Heterojunction research is a field of strong technological importance having at the same time profound fundamental implications. The band discontinuities at the interface are the most important parameters characterizing a heterojunction, being the departure point for all subsequent considerations. The issue of how the band gap difference at the contact of two semiconductors is accommodated between the valence and conduction band discontinuities deals with collective quantum phenomena and thus touches our very understanding of the basic principles of condensed matter physics. This question is still open though few tens of years of experimental and theoretical effort have passed from the first approach to this problem [1]. As shown in Chapter 2, the band offsets of semiconductor heterojunctions depend not only on the bulk properties of the two partners, but also on the detailed electronic structure of the interface.

An especially important class of heterojunction devices with an enormous social and economic impact are the solar cells as a source of clean and renewable energy. Thin film photovoltaics, although at a lower efficiency level than the single crystalline counterpart, is favored when speaking in terms of cost, energy balance, and production capacity. From the few prominent semiconductors for thin film technology (i.e., amorphous Si, polycrystalline CdTe and Cu-chalcopyrites), the polycrystalline I-III-VI$_2$ (I=Cu; III=In,Ga; VI=Se,S) chalcopyrite alloys are especially outstanding as they provide absorber materials for the to date most efficient thin film solar cells (for recent reviews see Refs. [2,3]).

After the first synthesis of CuInSe$_2$ in 1953 [3], the development of chalcopyrite solar cells started in 1974/1975 with the first significant CdS/CuInSe$_2$ single crystal device with a power conversion efficiency of 12 % (cell area 0.8 mm^2) [4]. Besides subsequent single crystalline devices (with lower efficiencies until 1994), thin film technology emerged in 1985 with an early polycrystalline Al/ZnCdS/CuInSe$_2$/Mo solar cell with 12 % efficiency (cell area 1 cm^2) [5] obtained from coevaporation using the bi-layer process (see Chapter 3). The result was surpassed in 1987 with a 14.1 % efficient device, produced by selenization of metal precursors (cell area 3.5 cm^2) [6]. Successful technological steps made by alloying CuInSe$_2$ with Ga and/or S, by using the three-stage absorber preparation process, and by incorporating Na into the chalcopyrite (see Chapter 3) led to a considerable improvement of the efficiencies

to the 18.8 % record level for 0.5 cm^2 laboratory cells in the present [7]. The chalcopyrites have also the best potential of any thin film for large scale production, as demonstrated by stable conversion efficiencies of 16.6 % for 4 cm × 4 cm mini modules, 12.7 % for pilot production 30 cm × 30 cm modules, and aproaching 11 % for 30 cm × 120 cm production modules [8-11]. The module manufacturing costs for annual production capacities in the range of 10-100 MW$_p$ are far below 1 €·W$_p^{-1}$ at reasonable production risks and energy payback time [12-14]. In addition, thin film ZnO/CdS/chalcopyrite solar cells are of considerable interest for photovoltaics due low weight (power-to-weight ratios as high as 1400 W/kg are reported [15]), stability (device performance actually improves with aging [16,17]), high flexibility (the fabrication of devices has successfully been demonstrated on metal and polyimide foils [18]), an excellent radiation hardness (chalcopyrite solar cells tolerate more than ten times larger fluence of high-energy electrons that any other type of solar cell technology [8,19,20]), and self-healing abilities (the damage produced by ion-implantation [21] or high-energy electron irradiation [22] significantly recover by annealing).

The world champion chalcopyrite devices with 18.8 % efficiency are made from Cu(In$_{1-x}$Ga$_x$)Se$_2$ absorber alloys with $x \approx 0.25$ and band gap energy $E_g \approx 1.15$ eV. Technologically important approaches also involve alloying with S [23-28]. Whereas Cu(In,Ga)Se$_2$ alloys have been studied in some detail during recent years [29-31], much less is known about the modifications that occur in the electronic properties of CuInSe$_2$ upon S alloying. Alloys of CuInSe$_2$ with Ga and S are advantageous due to the increase of their band gap which improves their match to the solar spectrum. The usage of multinary Cu(In$_{1-x}$Ga$_x$)(Se$_{1-y}$S$_y$)$_2$ alloys with higher Ga and/or S content instead of the standard low gap material is desirable when aiming towards high open circuit voltage devices which are especially important for tandem structures and thin film modules [32-34]. The increased voltages reduce the number of necessary scribes used for monolithic integration of the cells into a module. Because of low current densities, the thickness of the front and back electrodes can be also reduced [3]. In addition, higher band gap materials perform better at elevated temperatures due to a low temperature coefficient of the maximum output power [3]. Further technological advantages of high-gap chalcopyrite alloys include an enhanced tolerance to Cu/III-valent cation stoichiometry with respect to losses in conversion efficiency (e.g., for CuInS$_2$), as well as environmental benefits due to the replacement of toxic selenium and less abundant indium by sulphur and gallium [10,33]. However, the efficiencies of the to date best thin film solar cells based on high gap chalcopyrites are still at a relatively low level (i.e., 9.3 % for CuGaSe$_2$ [35] and 12.5 % for CuInS$_2$ [36,37]) compared to the record Cu(In,Ga)Se$_2$

devices. The main drawback of wide-gap chalcopyrite devices is the fact that the open circuit voltage V_{OC} does not increase at the same rate as E_g [34]. It is still unclear whether this trend results from high defect densities of wide-gap material [29,30], from less favorable band offsets at the CdS/chalcopyrite interface [34,38], or from changes in the recombination mechanism upon alloying CuInSe$_2$ with high contents of Ga and/or S [39,40].

This thesis investigates compositional trends of defect energies, band alignments, Fermi level pinning, and recombination mechanisms in polycrystalline Cu(In$_{1-x}$Ga$_x$)(Se$_{1-y}$S$_y$)$_2$ chalcopyrite thin film alloys. The experimental approach involves admittance spectroscopy (AS), current-voltage (JV), capacitance-voltage (CV), and external quantum efficiency (EQE) analysis of ZnO/CdS/Cu(In,Ga)(Se,S)$_2$ heterojunction solar cells, as well as photoluminescence (PL) spectroscopy of bare chalcopyrite layers.

The structure of the thesis is as follows. The problem of energy band alignment at semiconductor heterostructures and its implications are bibliographically addressed in Chapter 2 which illustrates the ongoing progress towards elucidating this issue and establishes a general background necessary for further discussions. Chapter 3 briefly introduces the basic properties of Cu(In,Ga)(Se,S)$_2$ materials and devices with a special focus on band diagrams and defect structures as relevant topics for this work. Chapter 4 describes the experimental conditions for the preparation and characterization of thin film absorbers and devices. The principles of the measurement techniques, the respective evaluation procedures, and formerly settled results are gradually discussed as introductory parts of the subsequent chapters. Chapter 5 provides a photoluminescence study of the defect-related radiative recombination in thin film Cu(In,Ga)(Se,S)$_2$ alloys with insights into the effect of anion alloying upon the emission characteristics. Chapter 6 investigates the composition dependence of the dominant defect energies in Cu(In,Ga)(Se,S)$_2$ chalcopyrites by admittance spectroscopy. The use of the acceptor energy level as a reference allows the determination of band alignments within the chalcopyrite system in terms of S/(S+Se) ratio y and Ga/(Ga+In) ratio x. Chapter 7 uses current-voltage and capacitance-voltage analysis to establish the dominant recombination paths in Cu(In,Ga)(Se,S)$_2$ chalcopyrites and the interrelationship with absorber composition in terms of Cu/(In+Ga) ratio which is found as the driving compositional parameter for charge carrier recombination. The results of the thesis as a whole and future perspectives are discussed in Chapter 8.

2. Band offsets in semiconductor heterojunctions

A series of theoretical approaches have gradually emerged over the last decades in the attempt to predict, to explain, or to control the band lineups for technologically important heterojunctions. This Chapter bibliographically addresses such representative models and their implications, and establishes a general background necessary for further discussions.

2.1. Introduction

Considering the problem of energy band lineup at the contact of two materials, the characteristic quantity is the barrier height for metal-semiconductor junctions, while the discontinuities of the valence and conduction band edges are the relevant parameters for semiconductor heterojunctions. Such discontinuities play the leading role in determining the transport properties of the heterojunctions and, in general, determine the behavior and the performances of the corresponding heterojunction devices. [41].

When two semiconductors with band gap energies E_{g1} and E_{g2} are joined together to form a heterojunction, the difference E_{g1} - E_{g2} must be accommodated by the discontinuities ΔE_V^{if} and ΔE_C^{if} of the valence and conduction band edges at the junction interface such that

$$E_{g1} - E_{g2} = \Delta E_V^{if} + \Delta E_C^{if} \quad . \tag{1}$$

As illustrated in Figure 1, the following sign convention for the band offsets can be considered: the valence band discontinuity ΔE_V^{if} is positive if the valence band edge of the small-gap semiconductor is (on the energy scale) above that of the large-gap semiconductor; the opposite convention is valid for the conduction band discontinuity ΔE_C^{if} [41]. The band alignments may vary over a wide range, from the most common *straddling* [42] lineup (the small gap fits entirely into the large gap, as e.g., in the material combinations AlAs/GaAs, ZnSe/GaAs, GaP/Si), via the less common *staggered* lineup (both band edges shifted up or shifted down as we cross the interface, as e.g., for CdTe/ZnTe, CdS/InP, CdS/CuGaSe$_2$, CdS/CuInS$_2$ heterojunctions), to the rare *broken-gap* lineup (the conduction band of one

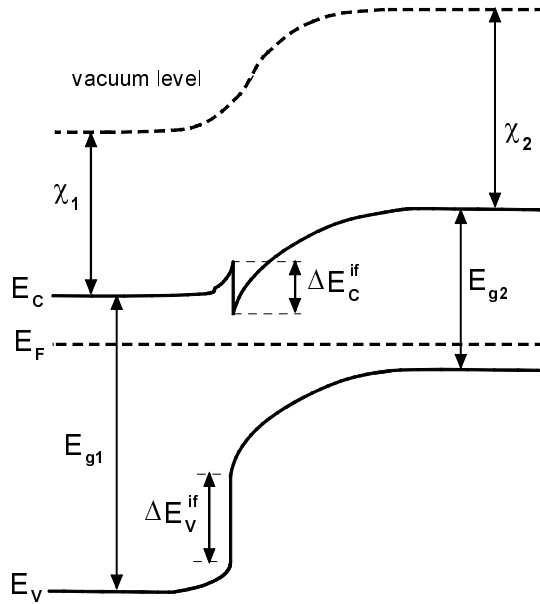semiconductor is on the energy scale under the valence band of the other, as e.g., in the case of InAs/GaSb).

Figure 1. Energy band diagram of a n-p heterojunction at equilibrium. E_C and E_V denote the conduction and valence band edges, and E_F is the Fermi level. The two semiconductors have different band gaps (E_{g1}, E_{g2}) and different electron affinities (χ_1, χ_2). The conduction and valence band discontinuities at the heterointerface are ΔE_C^{if} and ΔE_V^{if}, respectively.

2.2.   Band lineup measurement techniques

It seems that there is no an experimental technique to determine band offsets that is simultaneously simple, reliable, and universally applicable [43]. A class of techniques comprises electrical measurements by which the band offsets are extracted from capacitance-voltage or current-voltage characteristics of devices. Another group of methods is represented by photoemission and optical techniques.

2.2.1. Electrical techniques

The CV *intercept method* [43] uses a plot of C^{-2} vs. V (C is the heterojunction capacitance under an applied voltage V) which, for position-independent doping levels and if no interface charges are present, provides the built-in or diffusion voltage as the intercept voltage. The band offsets are further derived knowing the energy distances between the bulk band edges and the Fermi level for the two semiconductors. The *modified* CV *profiling technique* requires an adjacent Schottky contact placed on the outer surface of an isotype

(*n-n* or *p-p*) heterostructure whose doping profile $N_A(x)$ is known [43]. By reverse biasing the Schottky junction, the heterostructure is depleted and the CV characteristic of the Schottky junction rather than of the heterostructure is measured, yielding an *apparent free carrier concentration $n_a(x)$*. The diffusion voltage is obtained by integrating $[n_a(x) - N_A(x)](x - x_j)$, where x_j is the actual position of the heterojunction measured from the surface of the sample, and again the conduction band offset can be derived. The method is relatively insensitive to compositional gradients in the heterointerface region and to material parameters such as effective mass and permittivity [44-46]. The diffusion voltage and thus the band offsets for heterojunctions can be alternatively obtained by current-voltage measurements [47], admittance [48], or deep-level transient spectroscopy [49]. However, purely electrical measurements intrinsically perform averages in space, while the band discontinuities have a highly localized character.

2.2.2. Optical techniques

Photoemission spectroscopy probes locally the occupied electronic states near the surface and in particular the energy position of the valence band maximum. A semiconductor substrate with a thin overlayer of another semiconductor can be studied with this approach as a heterojunction in its early formation stages. The distribution in energy of the emitted photoelectrons from the sample surface (sampling depth of tens of angstroms) bombarded with ultraviolet or soft X-ray photons will contain contributions from substrate and overlayer. In particular, the region close to the upper leading edge of the energy distribution shows a double-edge structure related to the valence band maxima of the two semiconductors, allowing in this case the direct observation of the valence band discontinuity [41,50]. However, for many heterojunctions the valence band offset is small and the two edges cannot be as easily separated. In these cases, the valence band discontinuity is indirectly estimated by measuring the energy positions of the core-level peaks which often track the valence band edges if no chemical reactions take place during interface formation [41,51]. Somewhat related to the photoemission methods is the *internal photoemission*, which makes use of the photoexcitation of carriers at the heterointerface and the spectral dependence of the photocurrent is measured. Using a Schottky barrier adjacent to the heterojunction, the discontinuities are extracted from the apparent Schottky barrier height which is directly related to the photocurrent threshold [41,52-54]. Other optical measurement methods for heterojunction offsets involve absorption [55], transmission, and photoluminescence [56].

2.3.   Anderson approach - the electron affinity rule

The most straightforward mechanism to evaluate the relative position of the energy bands of two dissimilar materials is to align them both with respect to a common energy reference. If the vacuum level is taken as such reference, then we are in the frame of the electron affinity matching scheme [57]. Subsequent models showed that the deep impurity levels [58], the metal [59] (or semiconductor [60]) induced gap states, the charge neutrality level [61], the cation-vacancy level [62], the dielectric midgap level [63], or the dangling-bond energy level [64] provide substitutes for the vacuum level as well. The electron affinity approach was initiated in 1962 by a publication of Anderson [1] which proposed a coherent model to explain the electrical behavior of Ge/GaAs structures in terms of the parameters of the two heterojunction partners.

The Anderson model states that, similarly to the case of isolated semiconductors, the conduction band discontinuity for a heterojunction is the difference of the electron affinities of the two semiconductor partners

$$\Delta E_C^{if} = \chi_2 - \chi_1 \ . \tag{2}$$

The notations are illustrated in Figure 1. Similarly, the barrier height ϕ_n at metal/n-type semiconductor contact equals the difference of the metal work function ϕ_m and the electron affinity χ of the semiconductor, $\phi_n = \phi_m - \chi$, whereas at metal/p-type semiconductor contact $\phi_p = E_g - \phi_n$ holds (Schottky rule) [41]. A comparison between predicted valence band offsets according to eq. (2) and experimental values obtained mainly by photoemission measurements is presented in Figure 2 for various group-IV, III-V, II-VI, and chalcopyrite-based heterostructures [65-75]. The limitations of the electron affinity rule in predicting accurate values for the band discontinuities as seen in Figure 2 originate in neglecting the electronic structure of the interface. In addition, the method to derive a small number (~1 eV) from the difference of two large numbers (~5 eV) has a limited practical utility [57]. The interface effects modify the bulk band offsets of a heterojunction as high as hundreds of meV depending upon which semiconductor is deposited upon the other. Such behavior cannot be considered by the Anderson approach (and by other subsequent models which calculate the band discontinuities entirely in terms of bulk parameters of semiconductor partners). Particularly, the interface effects seems to be quite large for some CdS/chalcopyrite heterojunctions, since the corresponding data points considerably disagree with the electron affinity rule in Figure 2.
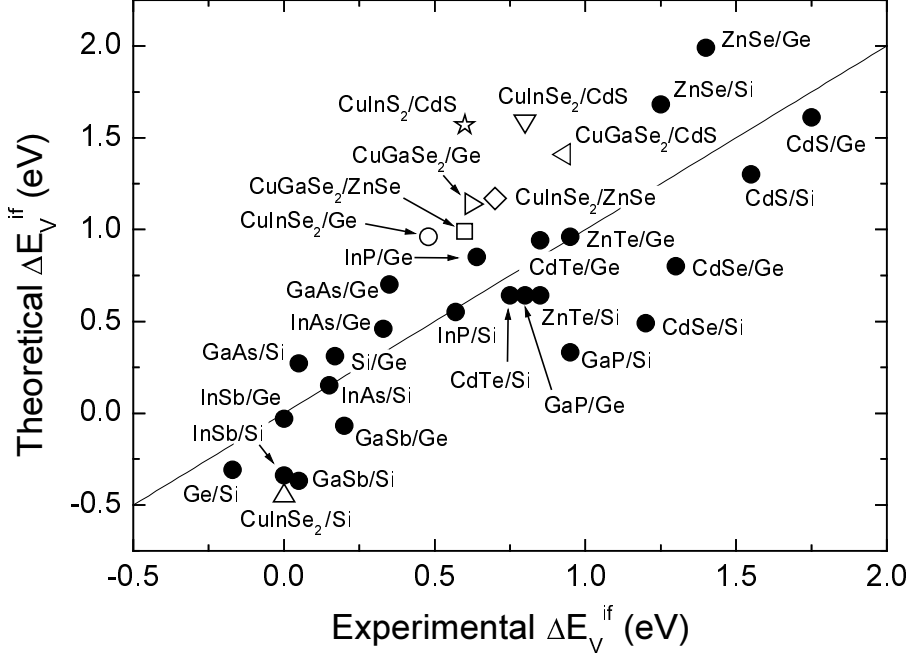
Figure 2. Comparison between experimental valence band offsets and prediction of the electron affinity rule. The data for non-chalcopyrites (full circles) are taken from Ref. [65]. The experimental valence band offsets of chalcopyrite-based heterojunctions are collected from Ref. [66] (up triangle, CuInSe2/Si; open circle, CuInSe2/Ge and right triangle, CuGaSe2/Ge), Ref. [67] (open square, CuGaSe2/ZnSe), Ref. [68] (open diamond, CuInSe2/ZnSe), Ref. [69] (left triangle, CuGaSe2/CdS), Ref. [70] (down triangle, CuInSe2/CdS), and from Ref. [71] (open star, CuInS2/CdS). The sign convention of Ref. [65] (see also Section 2.11) is adopted for the full symbols, while the data for the open symbols are determined using the sign convention in Section 2.1 and the electron affinities from Ref. [72] (Si and Ge), Ref. [73] (CuInSe2), Ref. [74] (CuGaSe2), Ref. [28] (CuInS2), and Ref. [75] (ZnSe and CdS). The straight line corresponds to perfect agreement.

One way to evaluate the interface effects is to describe them by a supplementary nonlinear term V_{dipole} (typically smaller than 100 meV) in eq. (2) [41]. Detailed theoretical calculations are necessary in this case. Another possibility is to consider metallurgical interactions at the heterojunction (or metal-semiconductor) interface leading to the formation of interface species [57]. Such mixed phases determine the existence of a unique effective work function (dominated by the anionic component in some cases) at the interface permitting the interface Fermi level to be pinned to this energetic position [57]. Further, both semiconductors should line up with respect to this single effective work function and the band offsets should again correspond to the difference of their electron affinities, so that the band offsets will be independent of interface Fermi level location. According to this modified version of the electron affinity approach of Freeouf and Woodall [57], a single effective work function at the interface will determine the band alignment of both pinned and unpinned heterojunctions.

Some of the first alternative approaches [65] to the electron affinity rule included the Adam-Nussbaum [76] and the von Ross [77] model. In the frame of the Anderson approach, the vacuum level is continuos across the heterojunction and the intrinsic Fermi level (not shown in Figure 1) displays a discontinuity at the interface. In turn, Adam and Nussbaum assumed the continuity of the intrinsic level at the heterointerface and this change resulted in a discontinuity ΔE_{VAC} of the vacuum level. The band alignment at the junction interface is then calculated analytically [76]. On the other hand, von Ross considered a discontinuity of the intrinsic Fermi level at the heterointerface like in the Anderson approach, but derived analytically a zero conduction band offset in the general case [77]. Thus, the conduction band edge was taken as continuos at the interface and the discontinuity of the valence band just as the difference in the energy gap of the two semiconductors. However, the overall agreement of both models with experimental data was worse than that of the electron affinity rule (and of other subsequent theories) [65] and the two approaches were finally outplaced.

2.4. The Frensley - Kroemer approach

Frensley and Kroemer [78] used as a reference the so-called *mean interstitial potential* defined as the arithmetic mean of the electrostatic potentials at atomic positions. This potential is not an absolute reference for the energy scale but has a constant energy position for each semiconductor partner. The difference between the mean interstitial potentials on the two sides of the heterojunction was called the *dipole potential*. The position of the bulk energy bands with respect to the mean interstitial potential is calculated using a self-consistent pseudopotential scheme [79]. Frensley and Kroemer further considered that the heterojunction band lineup is a by-product of the alignment of the mean interstitial potentials across the junction and thus derived the band offsets directly from the difference of band edges of the two semiconductors (including the correction for the dipole potential). This approach uses an ionic model of the solid in which the microscopic charge distribution is assumed to be a linear superposition of spherical ions. Within this model the average interstitial potential equals the potential at the infinity [78] and consequently some connection with the vacuum level arises. Thus, the interstitial-potential matching scheme is to some extend equivalent to the electron affinity rule. The procedure of Frensley and Kroemer requires only a knowledge of the energy-band structure of the participating semiconductors and does not invoke any surface

properties. The resulting band lineups are independent of the crystallographic orientation of the heterojunction. The calculated band offsets are in reasonable agreement with the experiment [65], however, because of the complexity of the required calculation, the approach has been superseded by subsequent models.

2.5.   The Harrison model

Another important approach to the band lineup problem has been forwarded by Harrison [80,81]. This approach places the band structure of each semiconductor on the same absolute scale using tight-binding calculations based upon universal parameters. The principle is to some extend similar to Anderson or to Frensley-Kroemer approach, since the energy band positions are calculated in terms of bulk parameters of the semiconductor partners and the valence band offsets are written as difference of the valence band maxima (which are always at the center of the Brillouin zone and thus supplementary uncertainties related to indirect band gaps are avoided). The calculated band offsets are again independent of the crystal orientation of the interface and of the order of deposition.

In the tight-binding approximation, the valence band maximum of an ideal covalent solid is

$$E_V = \frac{\in_p^c - \in_p^a}{2} - \left[\left(\frac{\in_p^c + \in_p^a}{2} \right)^2 + V_{xx} \right]^{1/2},$$

(3)

where $\in_p^c$ and $\in_p^a$ are the p-state energies of the cation and anion, and V_{xx} is an interatomic matrix element of the interaction between atomic p states and adjacent atoms [81]. The matrix element is empirically estimated as $V_{xx} \propto d^{-2}$, where d is the nearest cation-anion distance and the proportionality constant can be determined by fitting the data for known energy bands (e.g., Si and Ge). The V_{xx} and $(\in_p^c - \in_p^a)/2$ terms in eq. (3) represent covalent and polar energy components, respectively [80]. The valence band offset between two semiconductors is directly estimated from eq. (3). The agreement of the calculated heterojunction band offsets in the Harrison approach with measured values is reasonably good, even better than for the electron affinity rule or for the Frensley-Kroemer model [42,65].

The same tight-binding theory gives predictions of the band lineups for insulator-semiconductor and metal-semiconductor interfaces. According to theoretical values [81], the

semiconductor band edges fit near the center of the large insulator gap at semiconductor-insulator contacts. On the other hand, the metallic Fermi energy fits well above the conduction band minimum at metal-semiconductor contacts, in strong inconsistency with the experimental data which place the metallic Fermi energy near the semiconductor midgap. Thus, the consideration of the charge redistribution within the interface bonds during the junction formation appears as necessary. As a result, a surface dipole layer is produced which shifts the energy of the two sides of the junction relative to each other. The dipole shifts are found to be sensitive to the orientation and detailed geometry of the interface. Harrison argued that the corrections due to the interface bond dipoles for semiconductor heterojunctions are quite small on the scale of the disagreement between the predicted values and experiment (e.g., the experimental valence band offset for Si-Ge heterojunction is 0.17 eV [65], the calculated value according to eq. (3) is 0.38 eV [81], and the correction for a common (111) interface is 0.034 eV [81]). The corrections to the natural band lineups due to interface bond dipoles for metal-semiconductor contacts lower the metallic Fermi energy, reducing the mismatch significantly, but still leave the metallic Fermi energy well above the conduction band minimum (e.g., the aluminium Fermi energy is 3.4 eV above the silicon valence band maximum according to eq. (3) while the downshift of the aluminium Fermi energy due to interface dipole is 0.8 eV; the corresponding values for magnesium-silicon contact are 4.09 eV and 1.49 eV, respectively [81]). The fact that the electronic structure of the interface appeared to be an important ingredient to the problem of band lineups of metal-semiconductor structures and heterojunctions, determined the development of new approaches dealing with interface states which will influence or even determine the real band alignment.

2.6.   Virtual gap states - Tersoff approach

The free surface of a semiconductor (the same applies to the interface between two semiconductors) induces localized states in the band gap, called *virtual (intrinsic) gap states* [82,83]. The solutions of Schrödinger's equation for an infinite ideal semiconductor without surfaces are extended sinusoidal wavefunctions (Bloch waves) with real wavevectors giving rise to energy states in bands. On the other hand, wavefunctions related to surface states exponentially decay into vacuum and into the solid, and they exhibit real energies E but complex (imaginary) wavevectors k. While in the bulk real wavevectors are physically

meaningful, at surfaces, in turn, complex wavevectors are most relevant [84]. The surface (interface) states derive from the bulk bands and hence a knowledge of the bulk energy bands is necessary before the spectrum of the interface states can be calculated.

The dispersion relation $E(k)$ of the virtual states in the effective mass approximation for a one-dimensional model with two bulk bands is visualized in Figure 3(a), as follows from quantitative treatments [82-85]. The non-symmetrical shape of the $E(k)$ curve follows from different effective masses in the valence and conduction bands ($m_h \neq m_e$). Any value $k < k_{max}$ in Figure 3(a) belongs to two values of E, a nonbinding donor-like state in the upper hemisphere and a binding acceptor-like state in the lower hemisphere. Thus, any virtual gap state is a mixture of valence- and conduction-band character [60]. The state of energy $E_{BP} = E(k_{max})$ in Figure 3(a) at which the contributions from both bands are equal in magnitude is called the *branch (neutral) point* [59,84]. At this state the donor-like character changes into acceptor-like character and thus the energy E_{BP} is the Fermi level for the neutrality of the surface states. In the approximation of Figure 3(a) the energy position of the branch point is at

$$ E_{BP} = E_g \left(1 + \sqrt{m_h / m_e}\right)^{-1} \tag{4} $$

above the valence band edge [82,85]. Since the inverse magnitude of the complex wavevector k is proportional to the decay length of the respective wavefunction, the resonant state at the branch point has the smallest decay length into the bulk. If the branch point E_{BP} is different than the Fermi energy E_F in the bulk of the semiconductor, an exchange of electrons between surface states and volume arises producing a surface space charge region [82,86]. As first realized by Bardeen [86], if the density of surface states is sufficiently high ($\geq 10^{12}$ cm^{-2}), the Fermi level at the surface is pinned at a certain energy position. As a result, the barrier height at the metal-semiconductor junctions will be largely independent of the metal and approximately the same as for the free surface of the semiconductor (Bardeen limit). In this case the rectification characteristics of metal-semiconductor contacts are dominated by surface states, rather than resulting from the alignment of metal work function and electron affinity of the semiconductor with respect to the vacuum level. The physical nature of the surface states was disputed until Heine [83] derived the concept of *metal-induced gap states* [84] pointing out that at metal-semiconductor contact, metal wave functions tailing into the semiconductor gap produce effects similar to those of localized states. The net charge in these wavefunction tails, i.e., the charge transferred between metal and semiconductor, varies as a function of the position of the Fermi level within the semiconductor band gap [84]. No charge will be transferred across the interface when the Fermi level coincides with the branch point.
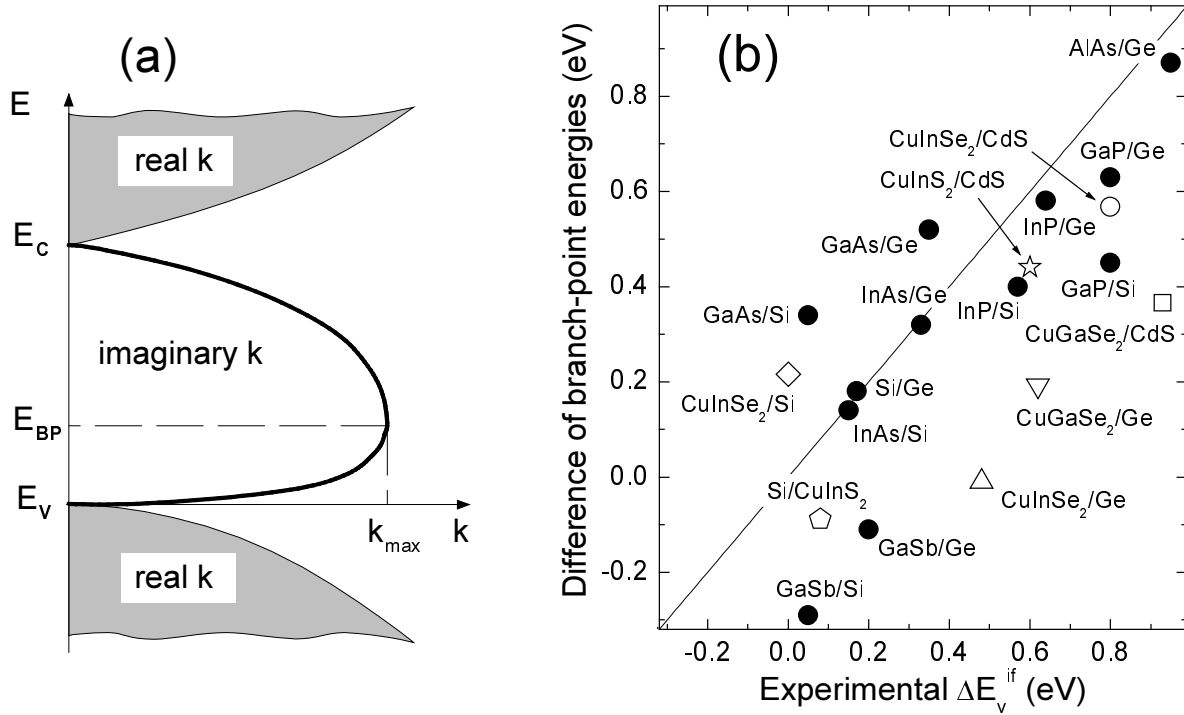
Figure 3. (a) Complex band structure of the interface states in the band gap [82-85]. The quantities E_V and E_C denote the energy position of the valence and conduction band edges when the wavevector k equals zero, and E_{BP} is the branch point energy. (b) Difference of branch-point energies of the semiconductors in contact vs. the corresponding experimental valence band offsets $\Delta E_V{}^{if}$ for different semiconductor heterostructures. The branch-point energy data (obtained by three-dimensional calculations using the Green's function description [60]) and the experimental valence band offsets for non-chalcopyrites (full circles) are taken from Ref. [87]. The experimental valence band offsets for chalcopyrite-based heterojunctions are collected from Ref. [70] (open circle, CuInSe₂/CdS), Ref. [69] (open square, CuGaSe₂/CdS), Ref. [71] (open star, CuInS₂/CdS), Ref. [66] (open diamond CuInSe₂/Si; up triangle, CuInSe₂/Ge and down triangle, CuGaSe₂/Ge), and from Ref. [88] (open pentagon, Si/CuInS₂). Unsimilar to non-chalcopyrites, the branch point energies for the open symbols are calculated using eq. (4) with the effective masses $m_e = 0.33 \cdot m_0$, $m_h = 0.55 \cdot m_0$ for Si [85], $m_e = 0.22 \cdot m_0$, $m_h = 0.39 \cdot m_0$ for Ge [85], $m_e = 0.17 \cdot m_0$, $m_h = 0.6 \cdot m_0$ for CdS [85], $m_e = 0.09 \cdot m_0$, $m_h = 0.71 \cdot m_0$ for CuInSe₂ [89], $m_e = 0.16 \cdot m_0$, $m_h = 1.3 \cdot m_0$ for CuInS₂ [90], and $m_e = 0.12 \cdot m_0$, $m_h = 0.8 \cdot m_0$ for CuGaSe₂. The full symbols follow the sign convention of Ref. [65] (see also Section 2.11), while the open symbols are determined using the sign convention in Section 2.1. The straight line corresponds to perfect agreement.

This concept was further developed by Tersoff [59] and applied to semiconductor heterojunctions [60]. When the valence or conduction band of one semiconductor overlaps the band gap of the semiconductor partner, the wavefunctions of the former semiconductor will penetrate in the latter giving rise to an interface dipole. This dipole tends to drive the band lineup towards that value which cancels the charge transfer at interface [60]. Thus, the band lineup is a byproduct of the alignment of the branch point energies of the two semiconductor partners [41], provided no extrinsic interface states exist in addition to these intrinsic interface-induced gap states. If each branch point is referred to the valence band edge of the

corresponding semiconductor, then the band offset at the heterointerface is given by the difference of the two branch point energies. A comparison between calculated valence band offsets for different heterojunctions and experimental values is shown in Figure 3(b). As considered in Refs. [60,87], this approach reaches a better accuracy in predicting experimental values than the previous models. This shows that the minimization of the interface dipoles is an important ingredient of the band lineup problem of semiconductor heterojunctions. For chalcopyrite heterostructures in particular, the predicted valence band offsets in the one-dimensional approximation of eq. (4) differ considerably from the corresponding experimental values. More refined, three-dimensional evaluations of branch point energies are necessary, as discussed in Ref. [91] where E_{BP} values of 1.2 eV, 1.3 eV, 1.2 eV, and 1.95 eV are given for $CuInSe_2$, $CuInS_2$, $CuGaSe_2$, and $CuGaS_2$, respectively. These values are substantially higher than those calculated with eq. (4), and set the respective branch-points in the upper half of the band gap. Nevertheless, other factors including extrinsic surface states and bulk defects seem to play an active role in determining the band alignment in chalcopyrite structures.

2.7.   The charge neutrality level

Flores and Tejedor approached the problem of band alignments of semiconductor heterostructures [61,92] and metal-semiconductor structures [93] in terms of charge neutrality conditions and, based on the same principle of virtual gap states as Tersoff, introduced the *charge neutrality level* (CNL), φ_0. For a given semiconductor, this level is defined as a gap energy below which interface charges in the semiconductor band gap are cancelled out by the lack of states in the valence band [93]. The CNL is a characteristic of the semiconductor and the specific position in the gap depends on the interface. The energy position of the CNL in the semiconductor gap is calculated by means of the surface Green function method for metal-semiconductor structures [93] and for semiconductor heterojunctions [61,92]. The calculations show that the flow of charge across the interface creates an interface dipole which tends to equalize both midgap energies of the semiconductors forming the heterojunction (or similarly, the metal Fermi energy and semiconductor CNL at metal-semiconductor structures) [92]. Flores and Tejedor argued that the restoring dipole at semiconductor heterojunctions depends linearly on the difference in energy between both

charge neutrality levels, the proportionality coefficient A having a value close to 2.5 and 2.1 for heterojunctions involving III-V and II-VI compounds, respectively [61]. Considering the total interface dipole as the sum of the restoring dipole and of a metal-like dipole (the last term corresponding to the dipole induced at the interface when this is treated like a metal-metal junction), the heterojunction valence band discontinuity, including corrections due to lattice effects, is written as [61,92]

$$\Delta E_V^{if} = \frac{1}{1+A} \left[\left(\chi_1 + E_{g1} \right) - \left(\chi_2 + E_{g2} \right) - D_j + A\left(\varphi_{01} - \varphi_{02} \right) \right].   \qquad (5)$$

Here E_{g1}, E_{g2}, are the band gap energies, χ_1, χ_2 and φ_{01}, φ_{02} are the electron affinities and the charge neutrality levels of the two semiconductor partners, and the quantity D_j is related to the metal-like terms for the heterojunction and for the individual semiconductors, as described in Refs. [61,92,93]. Eq. (5) gives the electron affinity rule [1] with the assumption $A = D_j = 0$. Similarly, the barrier height φ_n at metal/n-type semiconductor contact is derived as

$$\phi_n = \frac{1}{1 + A\,N_{VS}} \left[\phi_m - \chi + D_j + A N_{VS} \left(E_g - \varphi_0 \right) \right],   \qquad (6)$$

where χ, E_g, and φ_0 refer to the semiconductor, ϕ_m is the metal work function, and N_{VS} is the density of virtual states which is considered nearly independent of energy between φ_0 and the metal Fermi energy [93]. For a high density of interface states ($N_{VS} \rightarrow \infty$), $\phi_n = E_g$ - φ_0 holds (Bardeen limit [86]), while in the absence of interface states ($N_{VS} = 0$), a modified Schottky limit (due to the additional contribution of the term D_j) $\phi_n = \phi_m$ - $\chi + D_j$ is obtained. The charge neutrality approach appears to work well in predicting band discontinuities of representative metal-semiconductor structures [93].

2.8.   The dielectric midpoint energy

Cardona and Christensen [63] proposed an alternative way to define a reference level for the band alignments of semiconductor heterojunctions in connection to the screening effects on the hydrostatic deformation potentials. The band structure in the bulk and at the surface of materials is dependent on the hydrostatic pressure [94,95]. As a result, both the conduction and the valence band offsets of semiconductor heterojunctions are pressure

dependent [96]. If the criterion which determines the band offsets at semiconductor heterojunctions is the lineup of a reference level, this will be the same for all pressures [96]. When two semiconductors are brought together to form a heterojunction, the potential difference which appears will be screened by the electronic polarizability in a way similar to the hydrostatic deformation potential. These hydrostatic deformation potentials, screened by the dielectric response of the semiconductor provide the coupling constants between electrons and longitudinal acoustic phonons in the respective medium [63]. The screening of an external electrostatic potential acting equally on all band states is simply performed by dividing the potential by the zero-frequency intrinsic dielectric response function ε_s (static dielectric constant). In turn, perturbations generated by the hydrostatic strain accompanying longitudinal acoustic phonons act differently for each energy band and the screening has a more complex character. In this latter case, a fictitious state of certain energy - called *dielectric midpoint energy*, DME - in the gap is derived, for which the screening can be performed by the division by ε_s like in the standard case [63].

Cardona and Christensen [63] argued that the dielectric midpoint energy for a certain semiconductor is situated halfway between conduction and valence states at the *Penn gap* (or *dielectric gap*) E_{dg} dominating the dielectric response of the medium. According to the three-dimensional nearly free electron model of Penn [63,97], the dielectric response of a semiconductor is mainly produced by a group of filled states at a given valence band energy and a corresponding group of conduction states separated by the dielectric gap E_{dg}. The dielectric gap energy in this model approximately follows from $\varepsilon_s - 1 = (\hbar\omega_p / E_{dg})^2$ [84,97], where $\hbar\omega_p$ [98] is the plasmon energy of the valence electrons. It is also shown [63,84,99] that the dielectric gap estimated as above equals the standard band gap calculated (by first-principle theories based on local-density approximation) at *mean-value* points (or *Baldereschi* points [100]) in the first three-dimensional Brillouin zone. At such special points (the first mean-value point with the coordinates $(2\pi/a_0)(0.622, 0.295, 0)$, where a_0 is the parameter of the face-centred cubic lattice, is often used [63,99]) the value of any given periodic function in the reciprocal space becomes a very good approximation to the average value of the respective function throughout the Brillouin zone [100]. The dielectric midpoint energies, as calculated from the dielectric gaps in Ref. [63] for various group-IV, III-V, and II-VI semiconductor compounds are close to the corresponding Tersoff's branch-point energies [60]. It follows immediately the identification of the DME with the reference level E_{BP} for the band alignment of semiconductor heterojunctions. Thus, for large dielectric constant ($\varepsilon_s \rightarrow \infty$), the self-consistent band lineup should then be given by the alignment of the DME's of the

semiconductor partners, since the discontinuity of the DME at the heterointerface gives rise to a charge-transfer dipole and will be screened by the optical dielectric constant ε_s [63]. Evaluations of heterojunction band discontinuities using the concept of DME show a reasonable agreement with the experimental data [63].

2.9.   The dangling - bond approach

The dangling bond approach has been stimulated by various difficulties one faces when using the concept of intrinsic or metal-induced gap states. For example [101], there are no intrinsic surface states in the band gap of several compounds (GaAs, InP), and therefore such states cannot account for the observed Fermi level pinning in these structures; metal-induced gap states are supposed to extend into the bulk of the metal, and thus they are not defined for submonolayer metal coverage; metal-induced states do not apply at semiconductor/nonmetallic interface like GaAs/oxide which exhibits the same Fermi level pinning as metals; the Fermi level pinning for p-GaAs anneals out at the annealing temperature of a dangling-bond defect.

The dangling bond model lies in the same class of approaches which consider the charge distribution at the interface the most important factor determining the band lineup. For any solid, the surface atoms have a reduced number of nearest neighbors as the bulk atoms, resulting in non-saturated or dangling bonds at the surface. In the tight-binding theory of semiconductors [80,81], the individual electron states are written as linear combinations of atomic orbitals (a single atomic s state and three atomic p states on each atom) forming the semiconductor. In this approximation, the dangling bonds of surface atoms are identified with non-satisfied sp^3 hybrids and their back-bonds with four-fold coordinated atoms as unperturbed bulk bonds. Consequently, the individual dangling bond energy $\in_d$ of an atom in an elemental covalent semiconductor will be $\in_d = \left(\in_s + 3\in_p \right)/4$, where $\in_s$ and $\in_p$ are the usual free-atom binding energies (measured with respect to the vacuum level) [84]. In the case of a compound semiconductor, the average sp^3 hybrid energy can be defined as $\overline{\in}_d = (\in_d^a + \in_d^c)/2$, where the superscripts a and c refer to the anion and cation [102]. The dangling bond energy is an intrinsic characteristic of a given material and quantitative calculations in the tight-binding approximation show that for the majority of elemental semiconductors this energy fits in the band gap (exceptions include Si and Ge for which the

dangling bond energies are resonant with bulk valence band states) [84]. For compound semiconductors, the dangling bonds at surface anions have energies below the valence band maxima, while the dangling bond energies of their cations are always above the valence band [84,102]. In addition, cation dangling bonds are less tightly bound than anion dangling bonds and thus occupied anion and empty cation dangling bonds would be energetically favorable [84]. In the case of Cu-chalcopyrites, the dangling bond energy (with respect to the valence band maxima) of the surface chalcogen is close to an average value of -2.68 eV almost independent of the anion (S or Se) or the III-valent cation (In or Ga), whereas the dangling bond energies of the surface group-III element decrease from 5.43 eV in $CuInS_2$ over 4.87 eV ($CuGaS_2$) and 4.51 eV ($CuInSe_2$) to 3.95 eV in $CuGaSe_2$ [91]. The corresponding dangling bond energies of the surface Cu atoms are found to be higher, around $6.2 - 7.2$ eV [91].

At metal-semiconductor contacts, the semiconductor dangling bonds are coupled to the continuum of metal states, while at lattice-matched heterojunctions, the dangling bond states will couple by pairs across the interface. The dangling bond approach uses a similar principle to Tersoff approach. Specifically, the reference level for the band alignments of heterojunctions and metal-semiconductor structures is identified with the average energy of dangling bonds [64], rather than considering virtual, metal- or semiconductor-induced gap states. The zero-charge transfer condition at the metal-semiconductor interface corresponds to the alignment of the metal Fermi energy and the dangling bond energy of the semiconductor, while the two average dangling bond energies should align at semiconductor heterointerface [64,101,103]. Again, the valence band offset for semiconductor heterojunctions is predicted from the difference of the dangling bond energies with respect to the valence band edge of the semiconductor partners. As shown in Ref [64], the accuracy of the method is considerably good, even when using different sets of parameters to calculate dangling bond energies.

2.10. The deep level model

Simple models fail to explain and to predict the heterojunction band offsets whereas full theories are quite complex [41]. As a result, empirical or semi-empirical approaches have emerged in the attempt to give solutions to the band lineup problem and to organize in a better manner the existing data. One of the most important approaches of this type is the deep-level model initiated in 1985 by Zunger [104] and independently by Langer and Heinrich [105],

based on theoretical considerations of Caldas et al. [106]. The basic idea was to replace the traditional system (shown in Figure 4(a)) of referring impurity-related deep levels to the band edges of semiconductors by a more natural vacuum-referred system. The latter choice revealed that deep energy levels induced by a given impurity in different semiconductors of the same family (e.g., III-V or II-VI) are largely independent of the host material as long as they are measured from the vacuum level [58]. A similar pinning behavior is found when investigating doping limits in various compounds [107]. Thus, in this approach the impurity levels provide a substitute for the vacuum level. The valence band offset at the interface between two semiconductors from the same class is then given by just the difference in the energy level positions of a transition metal impurity (with respect to the valence band edge) in the two compounds [105]. In addition, a strong correlation exists between the alignment of impurity levels and Schottky barrier heights in various compounds [108]. The deep level model offers in the same time a more natural classification scheme of the experimental data related to deep defects in semiconductors. This material invariance of impurity levels allows the evaluation of band alignments within a given semiconductor system with respect to the impurity level instead of using the vacuum level (or other equivalent level) as reference. This is shown schematically in Figure 4(b) for a generic semiconductor system AB [58,104].
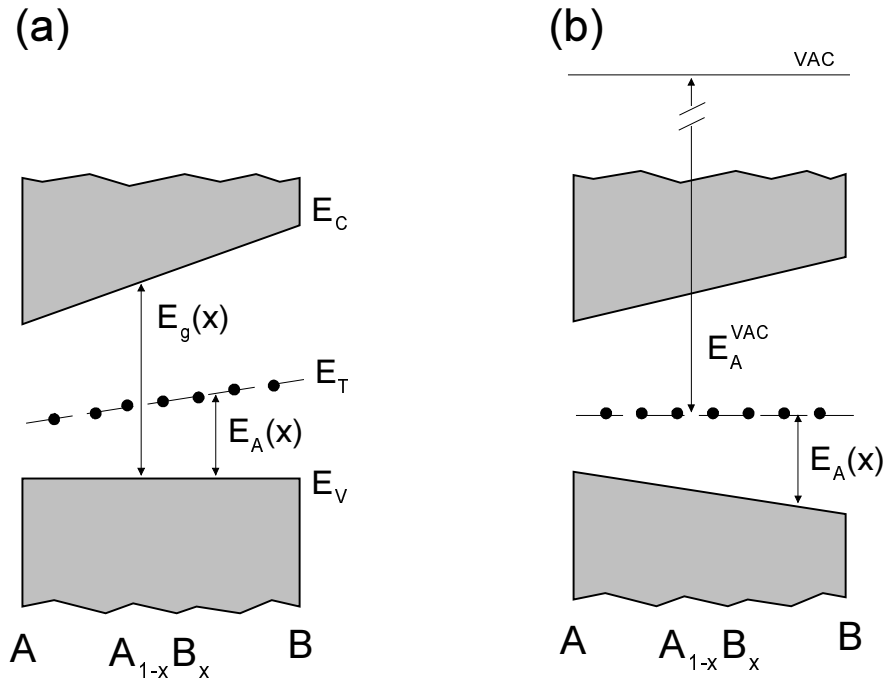

Figure 4. The deep level approach. The conventional practice (a) of referring impurity-related levels (E_T) to the band edges of semiconductor (E_C or E_V) is replaced by a vacuum-related energy system (b) in which deep levels induced by the same impurity are independent of the host material within the same family ($A_{1-x}B_x$) of compounds. The quantity $E_g(x)$ denotes the composition-dependent band gap energy, and $E_A(x)$, E_A^{VAC} are the impurity level energies measured with respect to the valence band maximum and to the vacuum level, respectively.

The accuracy reached by this approach is remarkably good [41,58]. The energy position of the impurity levels and the interrelationship with energy band alignments have been investigated in various semiconductor systems, including IV-IV (SiGe [109-112]), III-V (GaAsP [104,113-115], InGaAsP [116], AlGaAs [58], AlGaN [117]), II-VI (HgCdSe [118], HgSeTe [58]), II-III$_2$-VI$_4$ (ZnCdGa$_2$Se$_4$, ZnHgGa$_2$Se$_4$, CdHgGa$_2$Se$_4$ [119]), or I-III-VI$_2$ (CuGaAlSe$_2$ [120]) alloys. The deep level approach is applied in the present work to align the band edges within the chalcopyrite Cu(In,Ga)(Se,S)$_2$ system. The main difference here is that an intrinsic defect currently observed in chalcopyrites is used to align the energy bands within the alloy system, rather than making use of an extrinsic defect as above.

2.11. Linearity of band offsets

In general, the band offsets of semiconductor heterojunctions will be determined by the relative band energy positions in the bulk of the semiconductor partners and by the specific microscopic interface contributions. The relative weights of these two factors is of fundamental importance for the band lineup theories [41]. Approaches which neglect interface phenomena (like Anderson, Harrison, or deep-defect approach and unlike surface-states-models) are inherently based on the hypothesis of *linearity* of band offsets [41], and estimate ΔE_V^{if} or ΔE_C^{if} from the difference of parameters characteristic to the two semiconductor partners. The linearity implies the *commutativity* [65] of the band discontinuities, i.e., the band offsets are independent of the order in which one semiconductor is grown upon the other (like, e.g., for Si/Ge [65], GaAs/AlAs [121], ZnTe/HgTe and CdTe/HgTe structures [122], and unlike Ge/ZnSe [65]). Another consequence of the linearity is the property of *transitivity* (as referred to by Frensley and Kroemer [42,79]), which requires that for three semiconductors *A*, *B*, and *C*, the sum of the valence band discontinuities for the heterojunctions *A/B* and *B/C* gives the valence band offset for the heterojunction *A/C*, or, equivalently, the transitivity sum $\sum \Delta E_V^{if} = \Delta E_V^{if}(A/B) + \Delta E_V^{if}(B/C) - \Delta E_V^{if}(A/C)$ equals zero [122]. The implications of hypothesis of linearity are tested in Table I which lists the experimental valence band offsets for various triplets of heterostructures and the corresponding transitivity sums.

Table I. Test of transitivity rule for various triplets A/B, B/C, and A/C (substrate/overlayer) of semiconductor heterostructures. The last column gives the transitivity sum $\sum\Delta E_V^{if} = \Delta E_V^{if}(A/B) + \Delta E_V^{if}(B/C) - \Delta E_V^{if}(A/C)$. All valence band discontinuities ΔE_V^{if} are given in eV with the sign convention of Ref. [65] which considers the valence band offset as positive if the overlayer valence band edge is above the substrate valence band edge.

A	B	C	$\Delta E_V^{if}(A/B)$	$\Delta E_V^{if}(B/C)$	$\Delta E_V^{if}(A/C)$	$\sum\Delta E_V^{if}$
AlAs	GaAs	Ge	0.38 eV $\leq$	ΔE_V	$\leq$ 0.78	0.05[a]
GaAs	Ge	CuBr	0.4 eV $\leq$	ΔE_V	$\leq$ 0.9	-0.64[b]
CdTe	ZnTe	HgTe	0.10[c]	0.25[c]	0.36[c]	-0.01
GaAs	Ge	Si	0.35[d]	-0.17[d]	0.05[d]	0.13
GaP	Ge	Si	0.8[d]	-0.17[d]	0.95[d]	-0.32
GaSb	Ge	Si	0.2[d]	-0.17[d]	0.05[d]	-0.02
InAs	Ge	Si	0.33[d]	-0.17[d]	0.15[d]	0.01
InP	Ge	Si	0.64[d]	-0.17[d]	0.57[d]	-0.1
InSb	Ge	Si	0.00[d]	-0.17[d]	0.00[d]	-0.17
CdS	Ge	Si	1.75[d]	-0.17[d]	1.55[d]	0.03
CdSe	Ge	Si	1.3[d]	-0.17[d]	1.20[d]	-0.07
CdTe	Ge	Si	0.85[d]	-0.17[d]	0.75[d]	-0.07
ZnSe	Ge	Si	1.40[d]	-0.17[d]	1.25[d]	-0.02
ZnTe	Ge	Si	0.95[d]	-0.17[d]	0.85[d]	-0.07
ZnO	CdS	Ge	1.2[e]	1.4[e]	2.7[e]	-0.1
GaAs	CuAlSe$_2$	CuGaSe$_2$	-1.0[f]	0.8[g]	-0.3[f]	0.1
CuInSe$_2$	CdS	Si	-0.8[h]	1.55[d]	0.0[j]	0.75
CuInSe$_2$	CdS	Ge	-0.8[h]	1.75[d]	0.48[j]	0.47
CuGaSe$_2$	CdS	Ge	-0.93[k]	1.75[d]	0.62[j]	0.20
CuInSe$_2$	ZnSe	Si	-0.7[l]	1.25[d]	0.0[j]	0.55
CuInSe$_2$	ZnSe	Ge	-0.7[l]	1.4[d]	0.48[j]	0.22
CuGaSe$_2$	ZnSe	Ge	-0.6[m]	1.4[d]	0.62[j]	0.18
GaAs	CuGaSe$_2$	Ge	-0.3[f]	0.62[j]	0.35[d]	-0.03

[a]Ref. [121]; [b]Ref. [123]; [c]Ref. [122]; [d]Ref. [65]; [e]Ref. [124]; [f]Ref. [74]; [g]Ref. [125]; [h]Ref. [70]; [j]Ref. [66]; [k]Ref. [69]; [l]Ref. [68]; [m]Ref. [67].

Following Refs. [41,65], when considering non-chalcopyrite semiconductors, the average magnitude of the deviation from zero of the transitivity sum is in the order of 0.15 eV. This average deviation from zero is considerably higher for the structures involving chalcopyrites in Table I. In some cases, this sum deviates from zero by more than half of electronvolt, showing that the interface effects ignored (or treated with strong approximation) by all linear models can not be neglected [41]. The complex structure of the interface in multinary chalcopyrite-based structures possibly determines stronger contributions of interface phenomena. Generally, the average deviation from zero of the transitivity sum indicates an average accuracy limit underlying the linear models, and this accuracy limit might be a reasonable estimate for the average magnitude of the interface effects [41,65].

2.12. Closing remarks

The models of heterojunction band discontinuities can be divided according to the chosen reference level for the band alignments. Anderson [1], Frensley and Kroemer [78,79], Harrison [81], Zunger [104] and Langer [58] estimated the band discontinuities in terms of bulk parameters of the semiconductor partners, deriving a *natural* [41] band offset. Other approaches provided a reference related to the branch point energy [60], to the charge neutrality level [61], to the dielectric midgap energy [63], or to the dangling bond energy [64], all based on a common concept of *interface-induced gap states*.

An important ingredient in a generalized model is the relation between Schottky barriers and heterojunction discontinuities. In a first approximation, given two *p*-type semiconductors with band gap energies E_{gi}, electron affinities χ_i, and branch point energies E_{BP}^i ($i = 1,2$), and a metal with work function ϕ_m, the differences of the two Schottky barrier heights ϕ_{pi} ($i = 1,2$) should equal the valence band discontinuity ΔE_V^{if} at the interface between the two semiconductors, $\Delta E_V^{if} = \phi_{p1} - \phi_{p2}$ [41]. This correlation is predicted by the electron affinity rule [41] ($\Delta E_V^{if} = E_{g1} - E_{g2} + \chi_1 - \chi_2$ and $\phi_{pi} = E_{gi} + \chi_i - \phi_m$), by standard induced-gap-states-models [126] ($|\Delta E_V^{if}| = |\Delta E_{BP}|$ and $\phi_{pi} = E_{BP}^i$), or by empirical approaches based on impurity levels [108]. As discussed in Ref. [41], although such correlations are found [127], there are, however, significant and systematic deviations from the perfect agreement indicating that a unified model should include supplementary corrections.

Additional phenomena that should be considered are related to changes of band offsets at insulator-semiconductor structures [128] or semiconductor-semiconductor heterojunctions [41,127,129-133], when a thin intralayer of a third material is placed between the heterojunction partners. For instance, an Al metal intralayer increases the valence band discontinuity of CdS/Ge [131] and ZnSe/Ge [41,130] heterojunctions by about 0.15 eV and 0.3 eV, respectively. In addition, the metal intralayer-induced changes of band discontinuities generally saturate for submonolayer thicknesses of the intralayer [41,129,130]. These changes are related to the modification of the interface chemical bonds, of the microdiffusion proceses at the interface, or of the midgap energy points [41,129-131].

A first step towards a generalized theory of band lineups is made by including Schottky-like corrections terms within the frame of gap-states models [41,130]. With such corrections, the valence band offset ΔE_V^{if} between two semiconductors and the *p*-type Schottky barrier

heights ϕ_{pi} $(i = 1,2)$ between each semiconductor and a metal are written as [130]

$$\Delta E_V^{if} = E_{BP}^1 - E_{BP}^2 + S \left[(\chi_1 + E_{g1} - E_{BP}^1) - (\chi_2 + E_{g2} - E_{BP}^2) \right] \, ,$$

$$\phi_{pi} = E_{BP}^i + S^i (\chi_i + E_{gi} - E_{BP}^i - \phi_m) \, . \tag{7}$$

The notations are the same as above (an equivalent reference level like CNL or DME can be used instead of E_{BP}) and S, S^i are parameters related to the reciprocal of the optical dielectric constant. The Anderson-Schottky rule and the prediction of pure induced-gap-states models are recovered when $S, S^i \rightarrow 1$ and $S, S^i \rightarrow 0,$ respectively [130].

Another step is provided by the so-called '*induced-gap-states-and-electronegativity model*' of Mönch [84,134] which describes the charge transfer across the heterointerface and thus the dipole contribution in terms of difference of the electronegativities of the two junction partners. Further progress towards a unified model is made when the electronic defects (such as vacancies, antisite defects) created during interface formation are considered to interplay to the induced gap states in determining heterojunction band offsets and Schottky barrier heights [41,135,136]. Thus, in a unified approach, defects, induced-gap-states, and Schottky terms, all can play a role in determining the heterojunction band alignments and Schottky barrier heights [41].

3. Fundamentals of Cu(In,Ga)(Se,S)$_2$ materials and devices

3.1. The Cu(In,Ga)(Se,S)$_2$ chalcopyrite system

3.1.1. Crystallography

The I-III-VI$_2$ (I=Cu; III=In,Ga; VI=Se,S) chalcopyrite family of compounds is the ternary analogue to the II-VI binary semiconductors [3,137]. The I-III-VI$_2$ chalcopyrite tetragonal structure is obtained from the cubic II-VI structure by occupying the group-II atom sites alternatively with group-I (Cu) and group-III (In,Ga) atoms [3]. The chalcopyrite crystalline structure has the D_{2d}^{12} space symmetry group with eight atoms per primitive unit cell [137]. Each group-I and group-III metal atom (cation) is tetrahedrally coordinated by four group-VI chalcogen atoms (Se,S anions), while each anion is coordinated by two group-I and two group-III cations [137]. Because the strengths of the I-VI and III-VI bonds are generally different, the anion usually adopts an equilibrium position closer to one pair of cations than to the other, leading to tetragonal distortion in chalcopyrite materials (the ratio of lattice constants *c/2a* differs from 1) [3,138]).

3.1.2. Band gap energies

Despite the structural similarities, the band gap energies of the I-III-VI$_2$ chalcopyrites are substantially smaller than those of their binary analogs (the *band gap anomaly* of chalcopyrite semiconductors) [138]. The valence band maximum in chalcopyrites is dominated by the hybridization of Cu 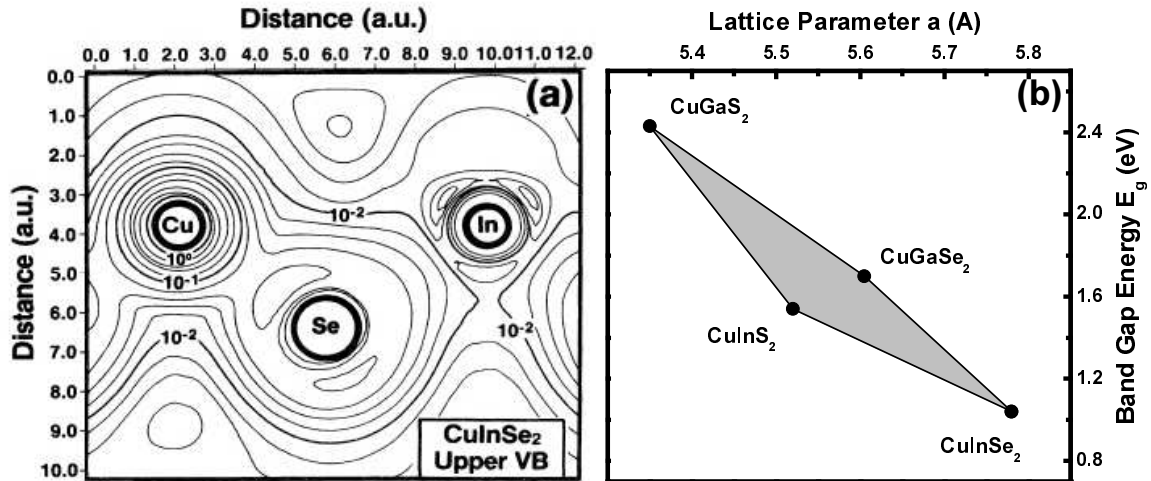3*d* and anion 4*p* orbitals [137,138]. This is illustrated in Figure 5(a) which shows the calculated electronic charge density for states in the upper valence band of CuInSe$_2$ (reproduced from Ref. [137]). As it follows from the peanut-shaped contours around Cu and Se, the Cu-anion contact appears as covalently bonded, whereas the In-anion contact appears as nonbonding. Thus, as shown in Ref. [137], the III-valent cation does not form a strong bond with the chalcogen atom in the upper valence band, in contrast to Cu which contributes significantly to the electronic charge (mainly with the *d* orbitals). In the binary semiconductors the cation has only deep, corelike *d* states, and as a result the *p-d*

repulsion determining the valence band maximum is generally small [137,138]. Since this *p-d* interaction is much stronger in chalcopyrites (due to the valence *d* states of Cu), the valence band maximum is pushed upward on an absolute energy scale leading to a reduction in the energy gap [137,138]. Figure 5(b) summarizes the band gap energies E_g and the lattice constants *a* for the Cu(In,Ga)(Se,S)$_2$ semiconductors. This system of copper chalcopyrites covers a broad range of the band gap energies E_g from 1.04 eV in CuInSe$_2$ over ~1.54 eV in CuInS$_2$ and ~1.7 eV in CuGaSe$_2$ up to 2.43 eV in CuGaS$_2$, overlaying most of the visible spectrum [3,138]. The band gap energy increases by alloying CuInSe$_2$ with Ga and/or S. At the same time, there is a complete range of miscibility in the respective alloy system [3] and thus all the alloy states and all the band gap energies are thermodynamically and technologically accessible.

Figure 5. (a) Calculated electronic charge density for states in the upper valence band of CuInSe$_2$ (reproduced from Ref. [137]). (b) Band gap energy E_g vs. the lattice constant a for Cu(In,Ga)(Se,S)$_2$ chalcopyrite compounds.

The band gap energy E_g shows a slight anomalous increase in some cases (e.g., CuInS$_2$) with increasing temperature in the low temperature range, while at higher temperatures E_g decreases under increasing T [139-142]. The anomalous behavior of the band gap energy at low temperatures is considered to stem from the diminishing *p-d* hybridization upon increasing T [140]. The pressure dependence of the band gap displays positive dE_g/dP coefficients which are smaller than those of the binary II-VI analogs [94,95]. A possible explanation considers that the *d* orbitals typically have very small pressure coefficients, and therefore the strong *p-d* hybridization in chalcopyrites contributes to the reduction of the band gap pressure coefficient [94,95].

3.1.3. Phase diagram

The complexity of the multinary material system is reflected into the phase diagram of the chalcopyrite compounds. The phase relations for various compounds within the chalcopyrite system are collected in Ref. [143]. The complex ternary phase diagrams of I-III-VI$_2$ chalcopyrites can be reduced to simpler pseudo-binary phase diagrams along the quasibinary I$_2$VI-III$_2$VI$_3$ tie-line. At certain temperatures most of the I-III-VI$_2$ compounds undergo solid phase transitions from the chalcopyrite structure to the high-temperature phase by disordering of the cation sublattice [143]. The phase diagram of CuInSe$_2$ with a special focus on the temperature and composition range relevant for the preparation of thin films has been recently corrected [2,144]. The existence range of the α-phase (CuInSe$_2$) along the quasi-binary I$_2$VI-III$_2$VI$_3$ tie-line is limited by the occurrence of the Cu$_2$-Se phase on the Cu-rich side, by the occurrence of the β-phase (CuIn$_3$Se$_5$) on the In-rich side, and by the formation of the δ-phase (the sphalerite phase) at high temperatures [3,144]. This existence range is very narrow and extends from a Cu-content of 24 at. % to 24.5 at. %, not including the stoichiometric composition of 25 at. % Cu [2,3,144]. Chalcopyrite CuInSe$_2$ thin films for photovoltaic applications have a slightly Cu-poor composition, and a tendency for phase separation in such photovoltaic-grade absorbers may be expected after deposition [3]. Fortunately, partial replacement of In by Ga, as well as the use of Na-containing substrates (e.g., soda lime glass) widens the useful range of absorber compositions [3,145,146]. In contrast to CuInSe$_2$ which melts congruently, the compound CuGaSe$_2$ is formed by peritectic reaction [143]. No intermediate ternary phases excepting CuGa$_5$Se$_8$ along the quasi-binary Cu$_2$Se-Ga$_2$Se$_3$ tie-line are reported in Ref. [143]. The phase relations in the Cu-Ga-Se system are investigated in detail in Ref. [147]. The phase diagram of CuInS$_2$ shows a congruent melting point [143,148]. The homogeneity region of CuInS$_2$ extends to both Cu$_2$S and In$_2$S$_3$ sides along the Cu$_2$S-In$_2$S$_3$ quasibinary tie-line at high temperatures ($T > 800$ ^{0}C), and is very narrow at room temperature [148]. The compound CuInS$_2$ undergoes two solid state phase transitions making the single crystal growth from its own melt difficult [143,148]. The CuGaS$_2$ chalcopyrite has the highest (congruent) melting point within the ternary field of chalcopyrites and a wide homogeneity range both to Cu$_2$S and Ga$_2$S$_3$ rich compositions at elevated temperatures [147].

3.1.4. Preparation methods

Besides vapor- [149] or liquid- [150] phase epitaxial growth and single crystal growth from gas phase (e.g., by chemical vapor transport [151]), from solution (e.g., by traveling heater method [152]), or from melt (e.g., by Bridgman method [153]), Cu-chalcopyrites are prepared as polycrystalline thin films by a wide variety of methods [154]. These techniques include coevaporation [155], sequential deposition [156], sputtering [157], laser ablation [158], electrochemical deposition [159], spray pyrolysis [160], or particle deposition [161]. Polycrystalline thin films produced by coevaporation and selenization of metal precursors yield the highest efficiency devices [3,154].

When using coevaporation technique, material deposition from elemental sources and film formation are performed in the same processing step [3]. The composition of the deposited material with regard to the metals corresponds to their evaporation rates, whereas the chalcogen is always evaporated in excess [3]. A low chalcogen evaporation rate during the deposition may lead to the formation of Na-induced secondary phase segregations (e.g., in CuGaSe$_2$ [162,163] or CuInS$_2$ [164]). Different compositions of the growing film determine different growth regimes. Excess Cu leads to the segregation preferentially at the film surface of a quasi-liquid Cu-chalcogen phase (Cu$_{2-x}$Se in the selenides and CuS in sulphides) which dominates the opto-electronic and surface properties of as-grown films [165]. After the preparation, the Cu-rich films have to be etched in aqueous solution of KCN which selectively removes the Cu-excess phase [155,166]. However, according to the present growth model [165,167], the Cu-excess phase acts a flux during the growth process and induces the vapor-liquid-solid growth mechanism with a beneficial effect upon the final film quality. As a result, Cu-rich films have large, nearly stoichiometric grains in excess of 1μm, whereas In-rich films have much smaller grains [3]. Therefore, besides the *single-stage* process with constant evaporation rates of all elements during the growth, an advanced preparation recipe deliberately includes a Cu-rich stage during the deposition in order to obtain films of high quality [3]. This idea was first applied in designing the so-called Boeing or *bi-layer* process which starts with the deposition of a Cu-rich layer and ends with an excess In rate in order to consume the copper-selenide phase and to bring the overall composition in the Cu-poor region [3,168]. Another possibility is the *inverted process* by which Cu and Se are deposited on the top of a (In,Ga)$_2$Se$_3$ precursor in order to obtain Cu(In,Ga)Se$_2$ films with an overall composition close to stoichiometry [3,169]. Finally, the absorber preparation recipe leading to the currently record devices is the *three-stage process* which is based on the 'Cu-poor/Cu-rich/Cu-poor' deposition sequence [3,170].

3.1.5. Defects

While in elemental and in most of the binary semiconductors polycrystallinity leads to a high concentration of electrically active defects that have a detrimental effect on the performance of optoelectronic devices, the polycrystalline chalcopyrite thin films (e.g., CuInSe$_2$) are as good electronic materials as their single crystal counterparts [171]. The dislocations, stacking faults, twins and grain boundaries are found to be only slightly electrically active [172]. Some of the chalcopyrites (e.g., CuInSe$_2$) can be prepared as *n*- or *p*-type by the introduction of native (intrinsic) defects [3]. CuInSe$_2$ samples with *p*-type conductivity are grown if the material is Cu-poor and is annealed under high chalcogen vapor pressure, whereas Cu-rich material with chalcogen deficiency tends to be *n*-type [3,173,174]. Thus, the chalcogen vacancy V_{Se} acts as donor in the *n*-type material and the Cu vacancy V_{Cu} as acceptor in the *p*-type material [3]. Theoretical calculations [171] indicate negative formation energies for Cu vacancies V_{Cu} implying the spontaneous formation of these defects under equilibrium conditions [3]. A defect complex with very low formation energy in CuInSe$_2$ is the ($2V_{Cu}^{-}$, In-on-Cu antisite In_{Cu}^{2+}) cluster which is electronically neutral and does not exhibit an electronic transition in the band gap [171]. Thus, this complex can accommodate a large amount of excess In and, at the same time maintain the electrical performance of the material [3]. Furthermore, first principle calculations [175] predict an attractive interaction among the defect pairs, describing the observed Cu-poor intermediate phases as ordered arrays of defect pairs. The addition of Ga [176] and/or Na [177] to CuInSe$_2$ lowers the relative stability of the defect pairs, thus decreases the stability of the defect phases limiting the existence domain of CuInSe$_2$ towards the Cu-poor compositions, with the result of increasing the stability range of the chalcopyrite phase. Intrinsic defects like cation vacancies and antisite defects play also an important role in the defect structure of the sulphide CuInS$_2$ material, as shown by theoretical calculations [178,179].

3.2.   Thin film Cu(In,Ga)(Se,S)$_2$ - based solar cells

3.2.1. Device structure

Figure 6 illustrates the structure of a standard ZnO/CdS/Cu(In,Ga)(Se,S)$_2$ thin film heterojunction solar cell [3,180]. The chalcopyrite absorber with a thickness of about 2 μm is deposited onto Mo coated glass substrate. Soda lime glass is widely used as substrate, due to
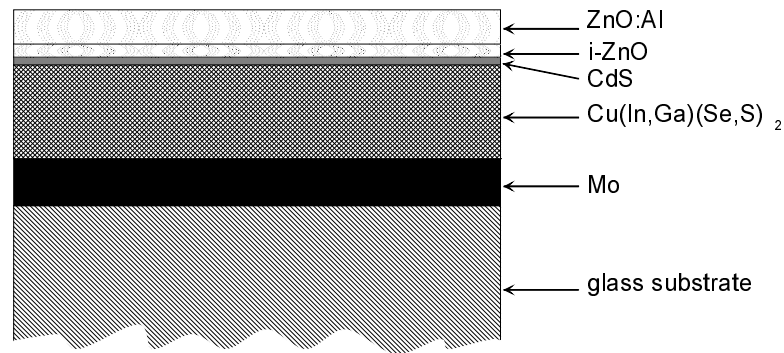
Figure 6. Typical structure of a thin film ZnO/CdS/Cu(In,Ga)(Se,S)₂ solar cell.

the beneficial impact of Na - diffusing out from the glass through the Mo layer into the absorber during the growth - upon the final film quality and device performance [3]. The incorporation of Na into the chalcopyrite absorber either from the glass substrate [180] or from Na containing precursor layers [181] is a necessary ingredient in order to obtain high efficient devices. The benefic effects of sodium are manifold [3]: Na improves the morphology (increases the grain size and induces a strong (112) texture) [181], increases the hole concentration reducing the compensation [21,181,182], induces beneficial changes in the defect distribution of the absorber [183], widens the existence range of the chalcopyrite phase of the phase diagram [177], facilitates the incorporation of Se into the film [184], promotes the oxigenation and passivation of grain boundaries [185]. However, the benefit of Na incorporation is limited by the formation of recently reported Na-related phase segregations (e.g., in polycrystalline $CuGaSe_2$ thin films [162] with a detrimental effect upon the device performance, or at the surface of $CuInSe_2$ single crystals [186]).

The Mo back contact has typically a thickness of about 1 μm [3]. Several criteria determine the choice of this material as base electrode, including the ability to form an ohmic contact to the absorber and a contact resistance which does not deteriorate under annealing, a good adhesion to the glass, and a considerable resistance to Se corrosion [154,172,187]. Furthermore, a $MoSe_2$ film forms at the Mo/absorber interface during absorber deposition [3,188],189]. $MoSe_2$ is a layered p-type semiconductor and the van der Waals planes are found to be perpendicular to the interface thus determining a good adhesion of the absorber [3]. At the same time, due to the larger band gap than that of the chalcopyrite absorber, the $MoSe_2$ layer provides an electronic mirror for the photogenerated electrons [3].

After the deposition of the *p*-type absorber, the heterojunction is completed by chemical bath deposition of a thin (typically 50 nm) CdS buffer layer, followed by sputter deposition of the ZnO window layer. The window structure consists of an undoped (intrinsic)

i-ZnO layer with a typical thickness of 50-70 nm adjacent to the CdS and a thicker Al-doped ZnO layer. The final deposition step is the evaporation of an Al metal grid as a front contact [2,3]. For high efficiencies, an antireflective coating (e.g., MgF_2 [170]) can be further deposited to minimize the reflection losses.

The chemical bath deposition of the CdS buffer layer is required in order to remove the natural oxide from the film surface and to provide protection against damage and chemical reactions resulting from subsequent processing steps [3,190]. Furthermore, positive charges are supplied to the absorber surface by a Cu/Cd exchange at the interface [191] and thus the beneficial type inversion at the buffer/absorber interface is supported [3,190]. An intermixing behavior involving the elements S, Se and In at the $CdS/Cu(In,Ga)Se_2$ interface has also been identified [192]. The replacement of the chemical bath deposited CdS buffer layer is advantageous from the viewpoint of environmental safety and in-line production [3]. With some precautions, Cd-free buffer layers like $ZnIn_xSe_y$, $Zn(OH,S)$ or $In(OH,S)$ can be alternatively used (a record 18.1 % efficiency for Cd-free solar cells was recently obtained [193] from a device with a ZnS buffer layer) [3,194-196].

The ZnO window with a large band gap provides in excess of 90 % transmission to the majority of the intense solar spectrum and has a conductivity in the order of 2×10^3 $\Omega^{-1}cm^{-1}$ [2,154]. Although inferior to Indium-Tin-Oxide (InO:Sn) regarding the stability in humid environments, ZnO has several advantages including non toxicity and abundance of the constituting elements [3,197]. Additionally, no significant chemical interaction is found between ZnO and CdS at room temperature [124].

3.2.2. *Band diagram*

Figure 7 displays the equilibrium band diagram of the ZnO/CdS/wide-gap $Cu(In,Ga)(Se,S)_2$ heterostructure solar cell with a special focus on the active junction interface. The band gap energy E_g of the absorber can be conveniently accommodated between 1 eV and 2.4 eV depending on alloy composition as discussed in Section 3.1, whereas the band gap energies of the CdS and ZnO are 2.4 eV and 3.3 eV, respectively [124]. This degree of liberty of the absorber band gap values has a profound impact on the valence and conduction band discontinuities ΔE_V^{if}, ΔE_C^{if}, and on the hole barrier ϕ_b^p at the CdS/absorber interface. A major purpose of this work is to determine the composition dependence of these energy barriers relevant for electrical transport.
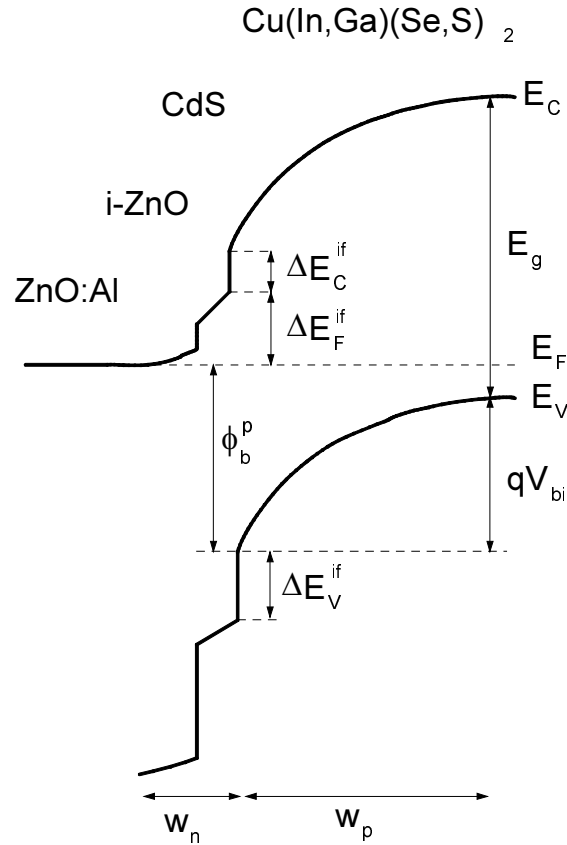
Figure 7. The equilibrium band diagram of the ZnO/CdS/wide-gap Cu(In,Ga)(Se,S)$_2$ heterojunction solar cell [3]. The quantities E_C, E_V, E_g, and E_F denote the conduction band, the valence band, the band gap and the Fermi energy of the absorber, respectively. The band offsets at the CdS/absorber interface are ΔE_V^{if}, ΔE_C^{if}, while ΔE_F^{if} is the energy distance between the Fermi level and the conduction band energy at this heterointerface. The widths of the space charge region in the n- and p-side of the heterojunction are w_n and w_p, respectively, and ϕ_b^p indicates the interface barrier for holes as described in the text. The built-in voltage of the p-type absorber is V_{bi}.

The discontinuity ΔE_C^{if} between the conduction band energy of the chalcopyrite and that of the CdS at the CdS/absorber interface is close to zero in case of the standard low-gap Cu(In$_{1-x}$Ga$_x$)Se$_2$ [70,198] but becomes negative in case of wide-gap chalcopyrites [34], as indicated in Figure 7. The barrier ϕ_b^p determines the transport of holes at the buffer/absorber interface [2] and has a significant effect upon the recombination at this interface, as it will be discussed in Chapter 7. Another important quantity involved in the interface recombination is the energy distance ΔE_F^{if} between the Fermi level and the conduction band energy at the CdS/asorber heterointerface. The sum $\Delta E_F^{if} + \Delta E_C^{if} = \phi_b^n$ is the barrier that electrons have to surmount when leaving the absorber if the device is under working conditions [3]. The CdS buffer layer is possibly completely depleted [199] and the valence and conduction band offsets at the CdS/ZnO interface are 1.2 eV and 0.3 eV, respectively [124].

3.2.3. Surface defect layer

An important particularity of the band diagram neglected in Figure 7 is a thin (10 - 30 nm) layer with a Cu-poorer composition and a larger band gap than the bulk chalcopyrite [3]. This layer naturally segregates on the top of Cu-poor Cu(In,Ga)Se$_2$ thin films in the uppermost surface region which has a stoichiometry and physical properties significantly different from the bulk material [3,200-202]. The existence of this layer has not been confirmed by structural methods up to now and is still under debate [3,190]. Although the precise properties of this separate surface phase and thus the details of the band diagram close to the CdS/absorber interface are not yet known, the experimental findings have lead to three different approaches which describe the situation [190].

The *ordered defect compound model* takes into consideration the two prominent features of the free surface of as-grown Cu(In,Ga)Se$_2$ films [190,201]. First, the band gap of Cu-poor Cu(In,Ga)Se$_2$ layers widens towards the surface of the film, this band gap widening being accommodated in a shift of the valence band edge of the chalcopyrite towards lower energies in the vicinity of the CdS/absorber interface [70,190,201]. Second, the surface composition of Cu-poor Cu(In,Ga)Se$_2$ films corresponds to a (Ga+In)/(Cu+Ga+In) ratio of approximately 0.75 for a range of bulk compositions of 0.5 < (Ga+In)/(Cu+Ga+In) < 0.75 [190,201]. Therefore, the segregation of the Cu(In,Ga)$_3$Se$_5$ phase at the film surface is inferred, an assumption compatible with the phase diagram [190]. However, charge neutrality estimations show that the weak *n*-type conductivity of the ordered defect compound Cu(In,Ga)$_3$Se$_5$ is not sufficient to achieve the surface type inversion of the chalcopyrite absorber [3,146].

The *surface defect model* views the type inversion at the surface as determined by shallow surface donors rather than by a distinct *n*-type surface phase [190]. These positively charged surface donors pin the Fermi level position and, according to the Cahen-Noufi model [203], are expected in the metal terminated (112) surface of CuInSe$_2$ films due to dangling bonds to the missing Se [3]. Air-annealing of bare absorbers passivates the surface states and reduces the type inversion such as the surface of Cu(In,Ga)Se$_2$ films is found in some cases to be nearly in flat band conditions after a long exposure to air [190] (reversibly, hydrogen annealing activates the respective surface states [204]). As mentioned in Section 3.2.1, a beneficial effect of the CdS deposition is to restore the type inversion at the absorber surface. Upon air-annealing of the complete heterostructure, the interface Fermi level is shifted away from the conduction band and, by extending the surface defect model to the active

CdS/absorber interface of the full device, this behavior is again interpreted in terms of passivation of surface/interface states [190,205].

The *defect layer model* combines the ordered defect compound model and the surface defect model by considering both the modification of the band structure due to Cu deficiency of the surface and the presence of positively charged surface states due to missing surface anions [146,190,199]. The surface states are responsible for the band bending which drives Cu away from the surface sites towards the neutral part of the film, such as the remaining Cu vacancies result in a high density of acceptor states close to the surface [190]. Thus, the defect layer model views the surface layer as a p^+-material rather than an *n*-type constituent. Furthermore, the surface defect layer is taught about as a consequence rather than an origin of the natural surface type inversion [190]. Experimental results indicate a close interrelation between surface Cu-vacancy formation and the Fermi level movement towards the conduction band, providing thus notable evidence which supports this model [190,206].

Due to the band gap enlargement towards the active heterointerface, the surface defect layer is an important ingredient when investigating electrical transport in relation to changes in the Cu-stoichiometry. Chapter 7 discusses this problem in more detail.

4. Experimental methods

4.1. Absorber preparation

The Cu(In,Ga)(Se,S)$_2$ chalcopyrite thin films are prepared by thermal evaporation from elemental sources on sodium containing glass. A two-step vacuum system (a rotatory and a turbo-molecular pump) and a liquid nitrogen cooled buffer trapping the impurities in the evaporation chamber provides the necessary vacuum conditions for deposition.
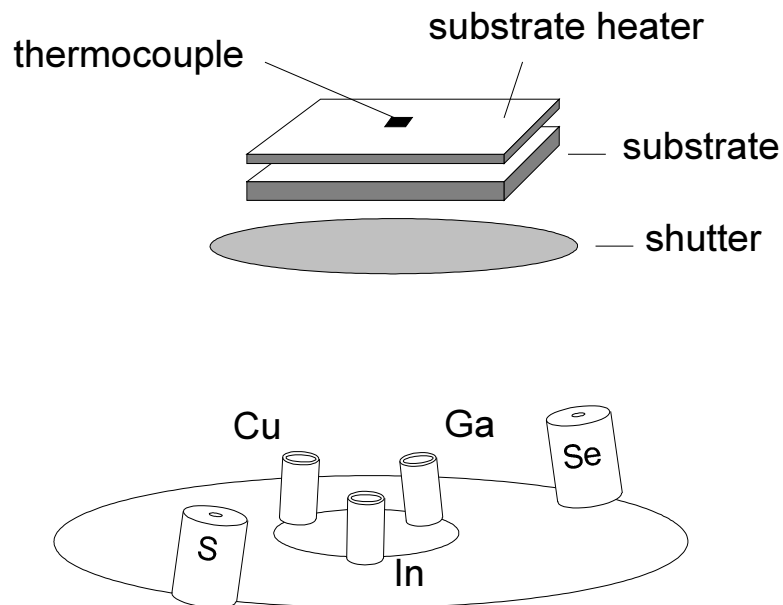

Figure 8. Experimental arrangement within the vacuum plant for the preparation of Cu(In,Ga)(Se,S)$_2$ thin film absorbers by coevaporation from elemental sources [3].

Figure 8 displays the schematic arrangement within the vacuum plant [3]. The metal Cu, In, and Ga species are evaporated from graphite crucibles and the chalcogen S and Se species from stainless steel effusion cells. The evaporation rates are controlled by the source temperatures. The deposition process requires a substrate temperature of about 550 ^{0}C. A single stage deposition process with constant evaporation rates of all elements and a constant substrate temperature is used for the preparation of the layers (an additional set of samples [207] including absorbers with compositional gradient in the depth is also used in this work).

The geometrical arrangement of the evaporation sources allows the preparation of samples with Cu-poor and Cu-rich composition in the same preparation run.

4.2. Absorber composition and morphology

The investigation of surface morphology and the determination of film composition are performed with a Zeiss (DSM 940) scanning electron microscope equipped with an attached energy dispersive X-Ray system (Noran). The electrons are focussed on the sample by an acceleration voltage of 25 kV.
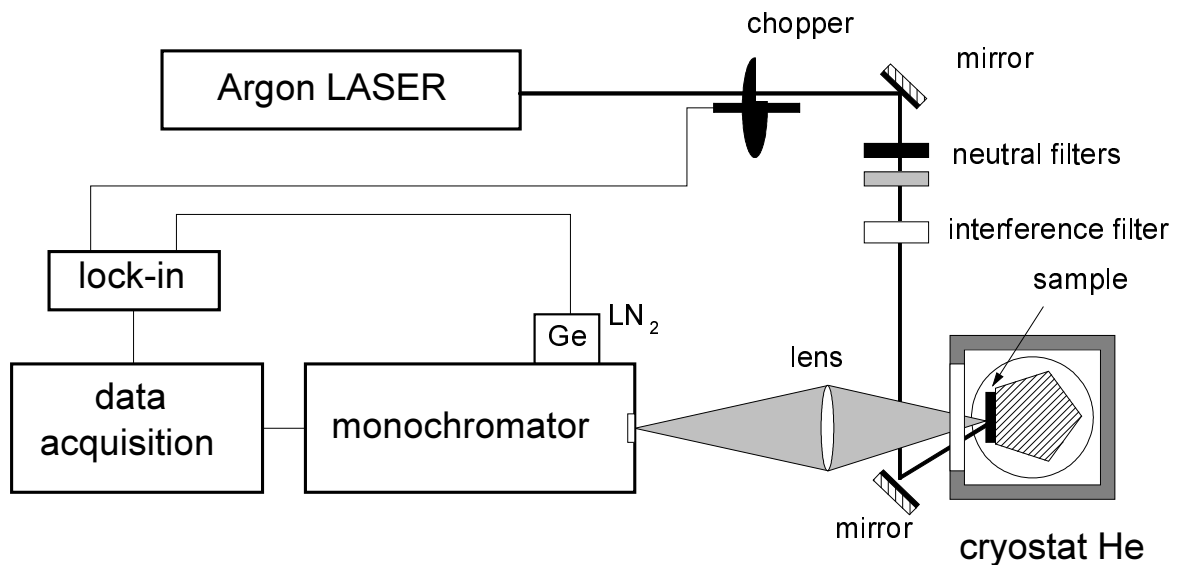
4.3. Photoluminescence

Figure 9. Schematic description of the experimental apparatus for photoluminescence measurements (after Ref. [208]).

Figure 9 shows the schematic diagram of the experimental setup for photoluminescence measurements. The excitation source is a continuous-wave Ar-ion laser (Stabilite 2017) operating at 488 nm. A set of neutral density filters is used for performing measurements at different excitation intensities. The samples are mounted on the cold finger of a closed-cycle helium cryostat allowing measurements at temperatures down to 11 K. The

emission spectra are analyzed by a monochromator (Jobin Hr 460) and the chopped signal is detected with a liquid nitrogen cooled germanium detector using the lock-in technique.

4.4.   External quantum efficiency
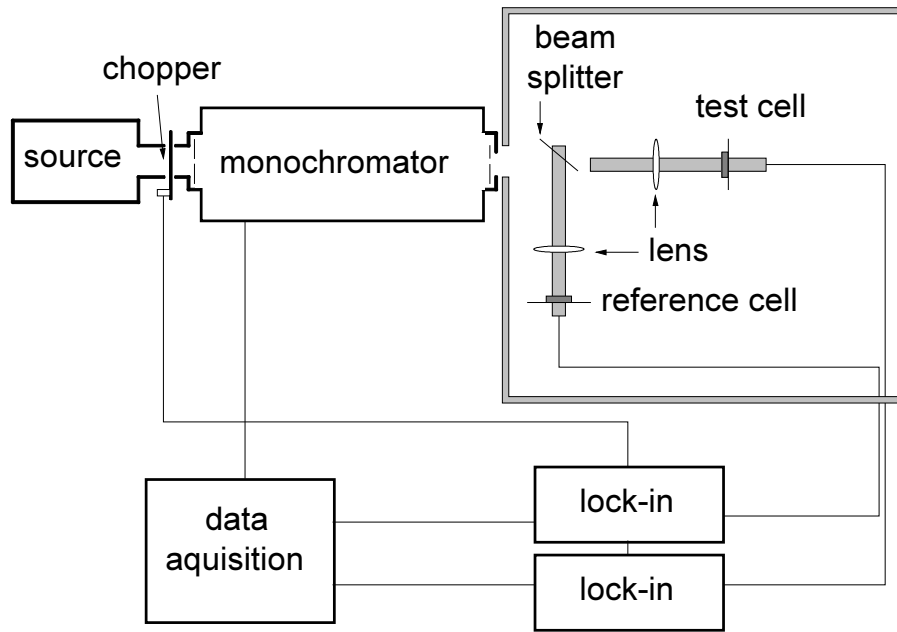
Figure 10. Schematic diagram of the experimental arrangement for the quantum efficiency measurements (after Ref. [209]).

The spectral quantum efficiency measurements are performed at room temperature with the experimental apparatus schematically shown in Figure 10. The illumination system provides radiation in the ultraviolet-visible-infrared wavelength range. After chopping and spectral decomposition by a monochromator (Bentham TM 300), the radiation is divided and a reference beam is focused on a separate monitor cell. The electrical signals from the test cell and monitor cell are phase sensitively amplified with a lock-in system. Calibrated detectors are used for reference measurements.

4.5.   Electrical characterization

Figure 11 schematically describes the set-up for electrical measurements. The solar cell heterojunctions with an area of 0.5 cm^2 are mounted onto a liquid nitrogen cooled stage in an evacuated chamber, allowing measurements at temperatures from 80 K to 360 K. The

electrical connection to the solar cell is realized using the four wire technique. A Hewlett Packard HP 4192A impedance analyzer measures the capacitance-frequency spectra under an applied *ac* signal of 50 mV, in a range of frequencies between 100 Hz and 10 MHz.
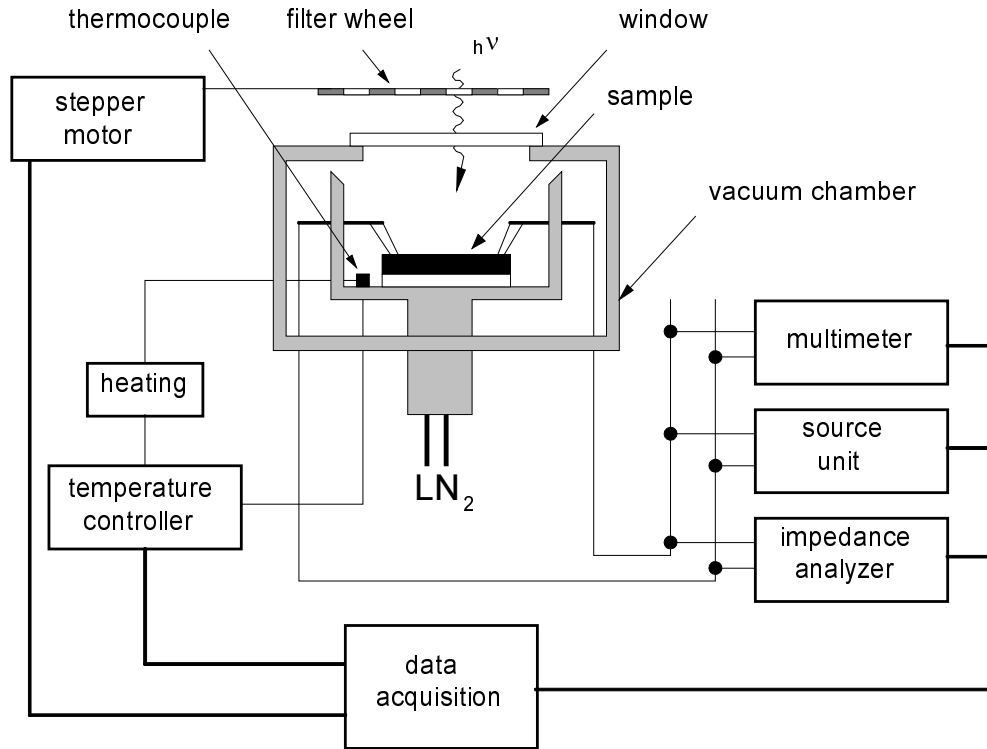

Figure 11. Schematic diagram of the experimental arrangement for the electrical analysis (after Ref. [210]).

The capacitance-voltage dark measurements are performed with a Keithley 2400 source meter and a HP 3478A multimeter in a range of voltages between - 1.5 V and 0.3 V. A Keithley 2400 source unit is used for performing the current-voltage measurements in a temperature range from 200 K to 360 K. A halogen lamp serves for illuminating the sample and a filter wheel controlled by a stepper motor allows for adjusting the light intensity by neutral density filters.

5. Photoluminescence spectroscopy

This Chapter investigates the radiative recombination processes in Cu(In,Ga)(Se,S)$_2$ alloys by temperature dependent and excitation intensity dependent photoluminescence measurements. After a brief description of the radiative recombination mechanisms in chalcopyrites, the dominant emissions related to shallow defects are analyzed with a special focus on the effect of anion alloying upon the photoluminescence spectra.

5.1. Basics

5.1.1. Radiative recombination mechanisms

In a photoluminescence (PL) experiment the electrons and holes are brought in nonequilibrium states by absorption of photons, and as a result of the transition from higher to lower energy states, the emission of radiation occurs [211]. Photoluminescence offers a nondestructive, sensitive tool for the spectroscopy of defects in semiconductors [212]. Possible radiative recombination processes include band-to-band, free-to-bound, exciton-related, or donor-acceptor transitions.

Band-to-band transitions [211] involve the recombination of free electrons and free holes. The emission spectrum $I(\hbar\omega)$ for semiconductors with a direct band gap E_g (like, for instance, Cu-chalcopyrites) is given in a first approximation by $I(\hbar\omega) = R\,(\hbar\omega - E_g)^{1/2}$, where the coefficient R depends on the effective masses of electron and holes [211]. The emission displays a low energy threshold at $\hbar\omega = E_g$. The high energy tail moves at higher energies under increasing excitation rate and increasing temperature, since emissions at higher energies are possible as the states deeper in the band become filled [211].

The *free-to-bound* recombination involves transitions of carriers from energy bands to the defect levels in the band gap [211]. If defects with binding energy E_A are involved, the emission line shape and its change with temperature is given in the hydrogenic approximation by

$$I(\hbar\omega) = u^{1/2} \exp\left(-u\right) , \qquad\qquad (8)$$

where $u = (\hbar\omega - E_g + E_A)/k_BT$ and with the peak maximum at $\hbar\omega_{peak} = E_g - E_A + k_BT/2$ (k_BT is the thermal energy) [89,212]. According to the above equation, if the temperature dependence of the band gap and of the ionization energy is neglected, the peak energy shows a blue shift of $\partial(\hbar\omega_{peak})/\partial T = k_B/2$ with increasing temperature [140a,213].

In sufficiently pure semiconductors, the excited electrons and holes pair off by Coulomb interaction forming *free excitons* which then recombine emitting a narrow spectral line at energy (in a direct gap semiconductor) $\hbar\omega = E_g - E_X$ [211], where E_X is the ground state binding energy of the free exciton (which is, e.g., 18 meV for CuInSe$_2$ [89] and 16 meV for CuInS$_2$ [214]). The thermal quenching of the emission line can be described by the general expression

$$I(T) = \frac{I(T=0)}{1 + B\exp(-E_X/k_BT)} \ , \tag{9}$$

where $I(T)$ is the intensity at the temperature T and B is a temperature independent constant [89]. At the cost of a lower transition probability, a direct transition can also occur with the emission of optical phonons (the energy of optical phonon modes is ~28 meV in CuInSe$_2$ [89], 36 meV in CuGaSe$_2$ [215], 35-40 meV in CuInS$_2$ [140a], and ~45 meV in CuGaS$_2$ [216]), and thus the narrow emission spectrum of a free exciton can be replicated at several lower photon energies [211]. The impurities can trap the excitons which become *bound excitons* emitting in a narrow spectral width at a lower photon energy than that of the free excitons [211].

When both donors and acceptors are present in a compensated semiconductor, the electrons from donor states can recombine with holes from acceptor states by *donor-acceptor pair* (DAP) *transitions* [211]. The coulomb interaction $E_{Coul} = q^2/(\varepsilon R)$ between a donor and an acceptor modifies the binding energy compared to the isolated-impurity case, such that the energy separating the paired donor and acceptor states, i.e., the emitted photon energy $\hbar\omega$, is given by [89,211]

$$\hbar\omega = E_g - E_A - E_D + \frac{q^2}{\varepsilon R} \ . \tag{10}$$

Here E_A, E_D are the ionization energies of the acceptor and the donor, ε is the dielectric constant, and R is the donor-acceptor separation. Since the distance R varies in a discrete fashion, the emission spectrum of the DAP transitions exhibits a fine structure [211]. With increasing excitation density, the number of photogenerated electrons and holes increases, the average donor-acceptor separation will decrease, and the DAP emission line will thus shift to higher energy [89]. The time dependence of the DAP recombination displays

a shift of the emission line towards lower energies with the time lapse after excitation [211,217]. This behavior results from a decreasing transition probability with increasing donor-acceptor distance, which determines a slower DAP recombination at low photon energies when compared to the high energy transition [211].

Important information about the underlying recombination process is provided by the behavior of the PL intensity I as the excitation power P is varied [218]. The excitation power dependence of the PL intensity can be described by a power law $I \sim P^{\gamma}$, where γ is a coefficient [89,212,218]. It has been found that $1 < \gamma < 2$ holds for the free- and bound-exciton emission, while γ is less than 1 for free-to-bound and donor-acceptor pair recombination [218].

5.1.2. Photoluminescence transitions in Cu-chalcopyrites

The photoluminescence emissions of $CuInSe_2$ [89,219], $CuIn(Ga)Se_2$ [213,220], $CuGaSe_2$ [212], or $CuInS_2$ [140] depend on the molecularity of the material. The deviation from the valence stoichiometry has also a considerable impact on the photoluminescence spectra (see Refs. [221,222] for the case of $CuInSe_2$ where the deviation from valence stoichiometry is defined as $\Delta z = \{2 [Se] / ([Cu] + 3 [In])\} - 1$, while the corresponding deviation from molecularity is $\Delta m = \{[Cu] / [In]\} - 1$). In addition to compositional trends, the effect of annealing upon the photoluminescence emission is reported (e.g., for $CuInSe_2$ [173], $Cu(Al,In)Se_2$ [223]), as well as that of illumination treatments (e.g., in the case of $CuInSe_2$ [224]). Investigations on $CuGaSe_2$ [225] show that the photoluminescence characteristics are not essentially deteriorated by solar cell processing steps.

In the $CuInSe_2$ prototype, the Cu-rich (Cu/In ratio larger than 1) polycrystalline thin films prepared by coevaporation are dominated by an emission band at about 0.97 eV (at 8.5 K) [89]. This emission shows a blue shift with increasing temperature and is attributed to a free-to-bound transition [89]. In these polycrystalline films [89], exciton-related emissions are observed at higher, near-band-gap energies (see e.g., Ref. [226] for near band edge emissions in $CuInSe_2$ films grown by molecular beam epitaxy), and additional transitions at lower energies. When turning to coevaporated $CuInSe_2$ polycrystalline thin films of slightly In-rich compositions, an abrupt change is obvious in the photoluminescence spectra showing now broad emission lines which shift towards higher energies under increasing excitation density or under increasing excitation wavelength and towards lower energies under increasing temperature [89,227]. The dominant emission in these In-rich films is assigned to donor-

acceptor pair recombination [89,219], although models involving energy band distorsions in highly compensated semiconductors are invoked in other cases (e.g., for In-rich CuIn(Ga)Se$_2$ films prepared by rapid thermal processing [220]).

In the case of Cu-rich and near-stoichiometric CuGaSe$_2$ thin films prepared by metalorganic vapor phase epitaxy, the low temperature (10 K) PL spectra show dominant emissions located at 1.62 eV and 1.66 eV, and in addition phonon replica and excitonic luminescence is observed [212]. The dominant emissions in such CuGaSe$_2$ material with near-stoichiometric composition are associated with a change in the recombination from DAP transition at low temperatures to a free-to-bound transition at higher temperatures [212] (a similar behavior was observed in CuInSe$_2$ crystals [228]; the superposition of free-to-bound and DAP recombination in other PL study on CuGaSe$_2$ was also considered [229]). When turning to Ga-rich compositions, such CuGaSe$_2$ epitaxial layers show single, broad PL bands which shift toward higher energy with increasing excitation power [212].

Upon alloying CuInSe$_2$ with S the photoluminescence emissions shift towards higher energies together with the band gap increase, generally maintaining their spectral features [214,230]. The near-band edge photoluminescence in CuInS$_2$ crystals is investigated in Refs. [90,140b]. When going from Cu-rich to In-rich composition, similar dominant features are found in the PL spectra of CuInS$_2$ crystals: two broad emission bands are seen in both cases, located (at 4.2 K) at about 1.36 eV and 1.39 eV in Cu-rich samples, and at about 1.41 eV and 1.44 eV in In-rich samples [140a]. The broad emission peaks (of In-rich CuInSe$_2$) shift to higher energies with increasing temperature or increasing excitation intensity [140a].

The low-temperature photoluminescence spectra of CuGaS$_2$ epitaxial layers deposited by metalorganic chemical vapor depostion contain near band gap exciton peaks and dominant emissions at about 2.43 eV and 2.39 eV (at 8 K) assigned to free-to-bound and DAP transitions, respectively [231]. In the case of CuGaSe$_2$ thin films deposited by coevaporation, dominant PL emissions located (at 4.2 K) around 2.3 eV for slightly Cu-rich material, and at about 2.4 eV for slightly Ga-rich material are observed [216].

5.2.   Results

The compositional trends of radiative recombination mechanisms with respect to S/Se alloying are investigated on Cu(In$_{1-x}$Ga$_x$)(Se$_{1-y}$S$_y$)$_2$ polycrystalline thin films [207] with a Ga/(Ga+In) ratio x of about 0.3 and with different S/(S+Se) ratios y. The chalcopyrite layers

are deposited by coevaporation onto Mo coated soda lime glass and have an overall Cu-poor composition. The PL analysis is carried out using the experimental setup described in Section 4.3. After the measurement, the photoluminescence raw data is multiplied with the function which takes into account the detector sensivity.
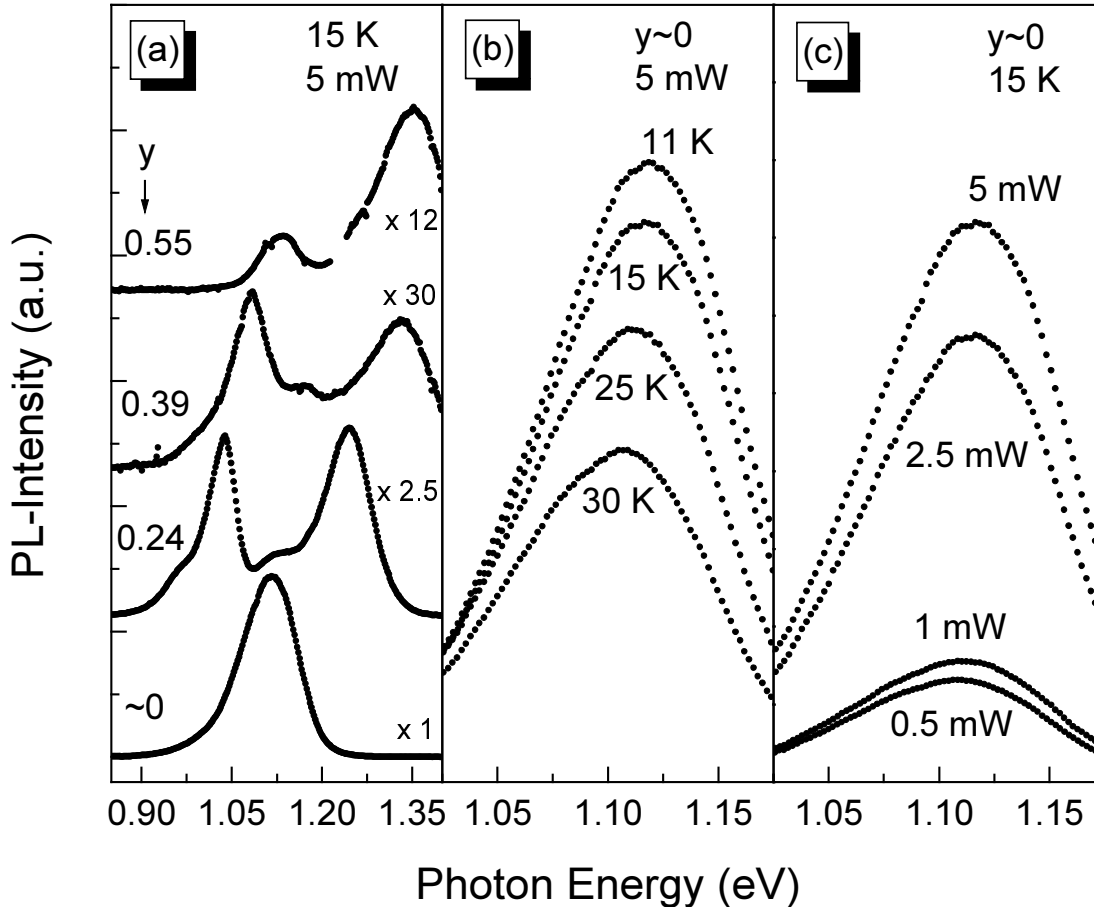

Figure 12. (a) Photoluminescence spectra of Cu-poor $Cu(In_{1-x}Ga_x)(Se_{1-y}S_y)_2$ chalcopyrite thin films with a Ga/(Ga+In) ratio x of about 0.3 and with different S/(S+Se) ratios y. The spectra are measured at the same nominal temperature (15 K), excitation wavelength (488 nm), and excitation power (5mW). (b) Temperature dependence and (c) excitation intensity dependence of the emission spectra for the sample with y ~ 0 in (a). All spectra are corrected for the detector sensitivity. The scale is different in (a) where the spectra are arbitrarily translated along the vertical axis.

Figure 12(a) displays the photoluminescence spectra of Cu-poor $Cu(In_{1-x}Ga_x)(Se_{1-y}S_y)_2$ polycrystalline thin films with a Ga/(Ga+In) ratio x of about 0.3 and and with different S/(S+Se) ratios y. Broad emissions are generally observed while the narrow excitonic lines are not detected on these samples. The PL lines move towards higher energies due to the band gap rising under increasing sulphur content [214]. Additional transitions are observed on sulphur-containing samples when comparing to the absorber with $y \sim 0$ (this absorber contains trace amounts of S). In addition to the different recombination paths, the supplimentary

transitions may originate from grading effects in the depth of the layers. The temperature and excitation intensity dependence of the photoluminescence response for the absorber with y ~ 0 in Figure 12 (a) is shown in Figure 12(b) and (c). The PL peak moves towards lower energies under increasing temperature or under decreasing excitation intensity. This behavior is observed when investigating other photoluminescence emissions in Figure 12(a), as discussed below. For a quantitative analysis, the peak energy and the peak intensity are determined directly from the photoluminescence spectra after correction for the detector sensitivity at different temperatures and excitation intensities. The overlapping of adjacent peaks is neglected and no deconvolution or fitting procedures are used when determining the characteristics of a certain emission peak.
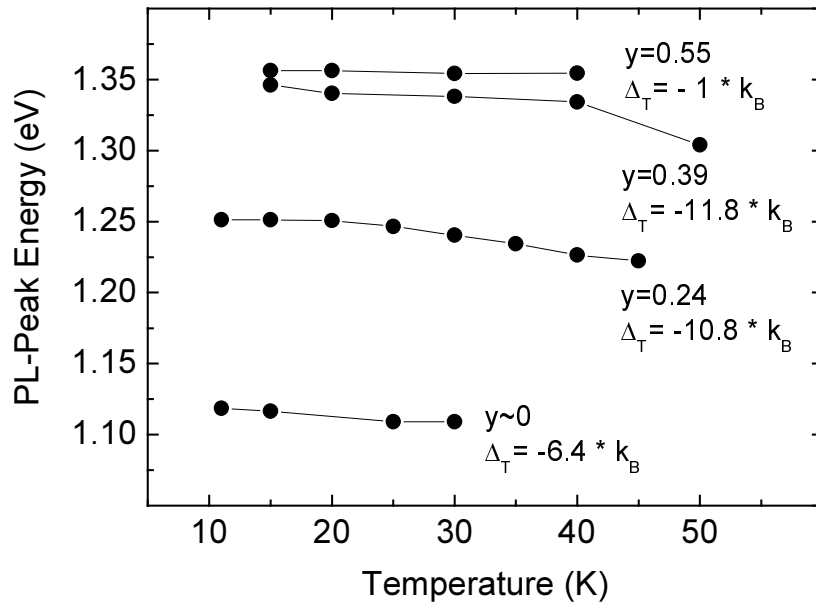
Figure 13. Peak energies as a function of temperature for the high-energy photoluminescence emissions of $Cu(In_{1-x}Ga_x)(Se_{1-y}S_y)_2$ thin films with $x \approx 0.3$ and with y = 0, 0.24, 0.39, 0.55 in Figure 12(a). The corresponding red shifts Δ_T are also indicated, where k_B is the Boltzman constant. The temperature dependence is measured at excitation intensity of 5 mW, 10 mW, 50 mW, and 10 mW for the absorbers with y = 0, 0.24, 0.39, and 0.55, respectively.

Figure 13 displays the red shift under increasing temperature for the high-energy photoluminescence emissions of the spectra in Figure 12(a). Red shifts Δ_T between $-1 \cdot k_B$ and $-12 \cdot k_B$ are observed, apparently not correlated with the sulphur content (the red shift of the sample with y ~ 0 increases considerably at higher temperatures possibly due to a delicate interchange which involves arising emission peaks as inferred from additional PL spectra). Figure 14 summarizes the dependence of the high-energy photoluminescence emissions of the spectra in Figure 12(a) on the excitation intensity. Characteristic energetic blue shifts Δ_P in the order of 10 meV/decade are seen under increasing excitation intensity in Figure 14(a) for
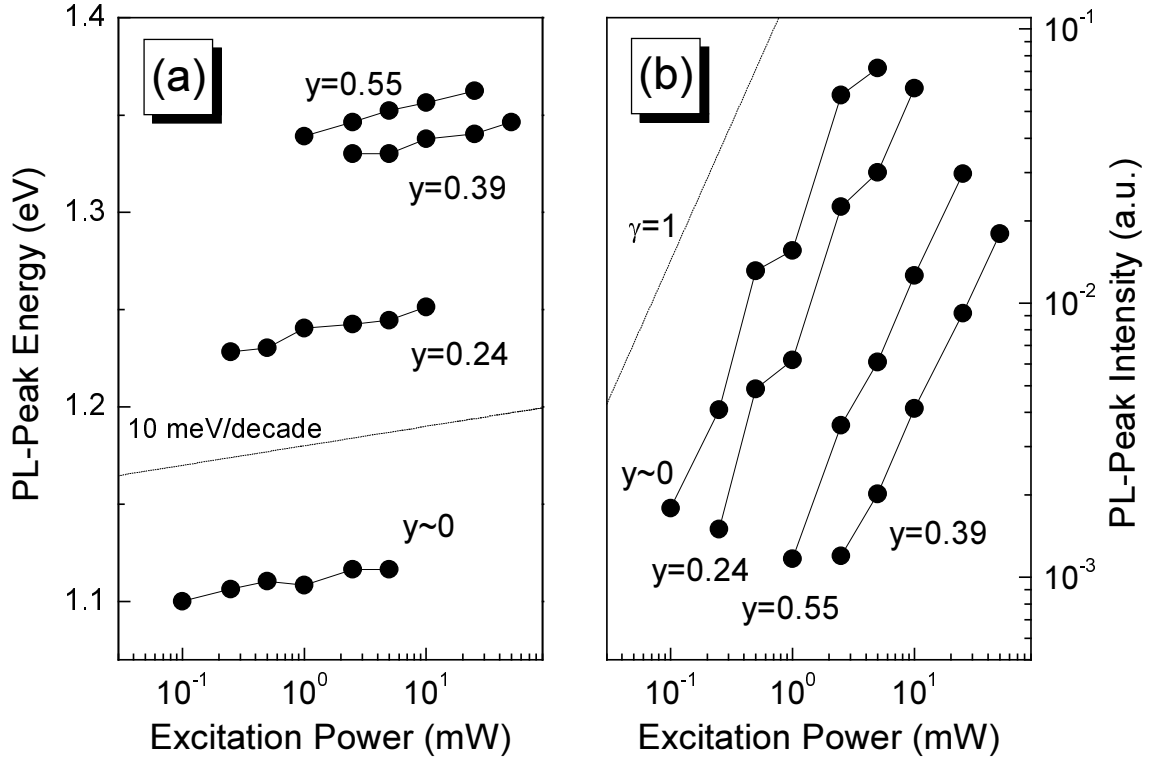
Figure 14. PL peak energy (a) and peak intensity I (b) at 15 K as a function of excitation power P for Cu(In$_{1-x}$Ga$_x$)(Se$_{1-y}$S$_y$)$_2$ thin films with x ≈ 0.3 and with y = 0, 0.24, 0.39, and 0.55. A blue shift Δ_P of 10 meV/decade under increasing excitation power is shown in (a), and the correspondence I = P$^\gamma$, with γ = 1 is indicated in (b). The characteristic values are Δ_P = 9.4 meV/decade, γ = 0.981 for y ~ 0; Δ_P = 13.8 meV/decade, γ = 0.964 for y = 0.24; Δ_P = 12.8 meV/decade, γ = 0.911 for y = 0.39, and Δ_P = 16.6 meV/decade, γ = 0.989 for y = 0.55.

all emissions and no significant saturation is reached. The emission intensity I as a function of the excitation power P in (b) follows the $I = P^\gamma$ law mentioned in Section 5.1. Table II summarizes the dependence of the investigated PL emissions on the temperature and on the excitation intensity.

5.3. Discussion

As mentioned in Section 5.1, the temperature coefficient $\Delta_T = k_B/2$ for a free-to-bound transition should be positive and generally independent on the specific sample [140a,213]. In contrast, negative temperature coefficients Δ_T are observed in Table II for the investigated chalcopyrite absorbers. The red shifts Δ_T are generally in the same range of magnitude as those reported by Zott et al. for In-rich CuInSe$_2$ thin films ($\Delta_T \approx 0.4$ meV·K^{-1} ≈ 4.6·k_B) [227]

Table II. Characteristics of investigated PL emissions in Cu-poor Cu(In$_{1-x}$Ga$_x$)(Se$_{1-y}$S$_y$)$_2$ thin film alloys with x ≈ 0.3 and with different ratios y: the peak energy positions at 15 K and 5 mW, the red shifts of the peak energy Δ_T under increasing temperature, the blue shifts of the peak energy Δ_P under increasing excitation intensity, and the respective γ coefficients.

y	Peak Energy (eV)	Δ_T (k_B)	Δ_P (meV/decade)	γ
0	1.12	-6.4	9.4	0.981
0.24	1.24	-10.8	13.8	0.964
0.39	1.33	-11.8	12.8	0.911
0.55	1.35	-1	16.6	0.989

which attributed the respective transitions to donor-acceptor pair recombination. The assignment involves the thermal ionization of the shallower member of a donor-acceptor pair which reduces the ionization energy of the deeper partner by $E_{Coul} = q^2/(\varepsilon R)$ (see eq. (10)) [89]. The reduction is larger for smaller R, determining the closer pairs to be thermally ionized before the distant pairs and thus the contribution of the distant pairs with lower transition energies is favored under increasing temperature [89]. However, true DAP transitions show usually a blue shift of peak energy with increasing temperature, explained by a predominant ionization of long-living distant pairs at higher temperatures and a remaining recombination due to closer pairs radiating at higher energies [213,232]. Such blue shifts are observed and correlated to donor-acceptor recombination in CuInS$_2$ crystals [140a] or in Cu-rich CuIn(Ga)Se$_2$ thin films [213]. In some cases (e.g., In-rich CuIn(Ga)Se$_2$ thin films prepared by rapid thermal processing) the dependence of the peak energy with increasing temperature changes from a red shift at low temperatures or low excitation intensities to a blue shift at high temperatures or high excitation intensities [220]. This latter behavior is explained by a model which considers highly defective and compensated semiconductors with fluctuating potentials (which superimpose the valence and conduction bands) due to charged defect clusters [220]. In such a frame (and e.g., when donors are much shallower than the acceptors), the recombination between electrons localized in donor point clusters and holes at acceptor levels dominates at low temperatures and moderate excitation intensities, while at high temperatures and/or high excitation intensities the dominant recombination involves electrons in the conduction band [220].

Blue shifts of peak energies with increasing excitation intensity are found in different chalcopyrite materials (e.g., CuInSe$_2$ [89,228], CuIn(Ga)Se$_2$ [213,220], CuGaSe$_2$ [212],

CuInS$_2$ [140a]). The blue shifts $\varDelta_P$ in Table II are an indication of DAP transitions, although common DAP recombination shows substantially smaller energetic blueshifts $\varDelta_P$ in the range 1-2 meV/decade excitation intensity [212,213]. Blue shifts $\varDelta_P$ in the range of 10 meV are found in heavily compensated semiconductors [220] indicating a high degree of compensation in the investigated samples.

The dependence of the peak intensity I on the excitation power P in Figure 14(b) shows no systematic deviations from the $I = P^{\gamma}$ law, where the coefficient γ is smaller than 1 in all cases, a typical range for defect-correlated recombination mechanisms [212,218].

5.4.   Conclusion

This Chapter has investigated the effect of anion intermixing upon the photoluminescence emissions using a set of Cu-poor Cu(In,Ga)(Se,S)$_2$ alloys with almost constant Ga/In content and with various S/(S+Se) ratios y. The PL maxima move towards lower energies under increasing temperature and towards higher energies under increasing excitation intensity. The features of the PL spectra may be essentially attributed to DAP recombination which seems to dominate the radiative recombination in the investigated compositional range. However, some particularities as large blue shifts of peak energy with increasing excitation power cannot be explained with the standard DAP model, and thus spatial potential fluctuations due to random distribution of charged defects in highly compensated semiconductors should be taken into account for a more quantitative evaluation.

6.   Admittance spectroscopy

After discussing the principle of admittance spectroscopy and the specific features for the chalcopyrite system, this Chapter investigates the composition dependence of the dominant defect energies in polycrystalline $Cu(In_{1-x}Ga_x)(Se_{1-y}S_y)_2$ chalcopyrite thin films. The energy bands within the alloy system are then aligned using the energy level of the intrinsic bulk acceptor as reference. The extrapolated band offsets between the end points of common-anion and common-cation chalcopyrite alloys are in fairly good agreement with first principle calculations.

6.1.   Basics

6.1.1.   General principle

Admittance spectroscopy is a suitable tool to characterize electrically active trap states in semiconductor junctions [233]. The technique involves the measurements of the junction capacitance as a function of frequency and temperature [234]. Under a small-amplitude *ac* signal applied to the junction, the traps at the Fermi level are charged and discharged and a contribution to the total device capacitance arises [234]. For a discrete level, the dependence of the additional capacitance C_i on the applied angular frequency $\omega = 2\pi f$ is given by [234]

$$C_i \propto \frac{\omega_i^2}{\omega_i^2 + \omega^2} \; . \tag{11}$$

At frequencies $\omega < \omega_i$ the trap emits and captures carriers following the applied signal while for higher applied frequencies the trap contribution cancels [233]. The inflexion point at ω_i is related to the emission rate e_T of the defect [234]

$$\omega_i = 2\,e_T = 2\,\sigma_{p,n}\,v_{th}\,N_{v,c}\exp\left(-\frac{E_A}{k_B T}\right) . \tag{12}$$

Here v_{th} is the thermal velocity, $k_B T$ the thermal energy, $N_{v,c}$ the effective density of states in the valence band or conduction band, $\sigma_{p,n}$ is the thermal capture cross section for holes and

electrons, respectively, and E_A is the energetic depth of the defect with respect to the corresponding band edge. Since v_{th} and $N_{v,c}$ depend on temperature like $T^{1/2}$ and $T^{3/2}$, respectively, and assuming a constant capture cross section $\sigma_{p,n}$, the inflexion frequency $f_i = \omega_i/2\pi$ of the capacitance spectrum takes the form [234,235]

$$2\pi f_i = \xi_0 \, T^2 \exp\left(-\frac{E_A}{k_B T}\right) , \qquad (13)$$

where the pre-exponential factor ξ_0 comprises all the temperature independent parameters that determine v_{th} and $N_{v,c}$. Therefore, an Arrhenius plot of $2\pi f_i / T^2$ vs. the inverse temperature $1/T$ should yield a straight line and the slope provides the activation energy E_A.

For the case of an energetically continuous and spatially homogeneous distribution of defects, the determination of trap contribution the junction capacitance is performed following the model of Walter et al. [233,234]. This procedure allows one to calculate the distribution of defect states $D(E)$ in the band gap of the absorber from capacitance spectra $C(T,f)$. The distribution of defects is obtained by an integration in energy and space of capacitance contributions originating from all trap states that exchange carriers with the bands [234]. Accordingly, the energetic distribution of defects $D(E)$ in the band gap is proportional to the derivative of the capacitance C with respect to the logarithm of the angular frequency [234]

$$D(E) = \beta(E) \, \frac{1}{k_B T} \, \frac{dC(\omega)}{d\ln(\omega)} , \qquad (14)$$

Where the function $\beta(E)$ preponderates the contribution of defects depending on their depth. The frequency axis is re-scaled into energy axis using eq. (13), where the value for ξ_0 is determined from the y-axis intercept of the Arrhenius plots [235].

6.1.2. Particularities for chalcopyrites

Admittance spectroscopy of ZnO/CdS/Cu(In,Ga)(Se,S)$_2$ heterojunctions mostly shows two electronic transitions [234] as illustrated in Figure 15(a), which depicts the qualitative energy band diagram at the CdS/chalcopyrite absorber interface. As mentioned in Section 3.2.2, in case of low-gap chalcopyrites, a small spike or an essentially flat band alignment in the conduction band is found across the junction, whereas under alloying with Ga and/or S a cliff is induced [34,38,70]. The two transitions, denoted in the following as N$_1$ and N$_2$, involve a spatially discrete distribution of interface donors and a homogenous distribution of bulk acceptors [234], respectively. The contributions of the traps N$_1$ and N$_2$ to the total

junction capacitance are shown in Figure 15(b). In the low temperature range the main contribution arises from the shallow interface donors, whereas the capacitance transient at higher temperatures is due to the bulk acceptors [234].
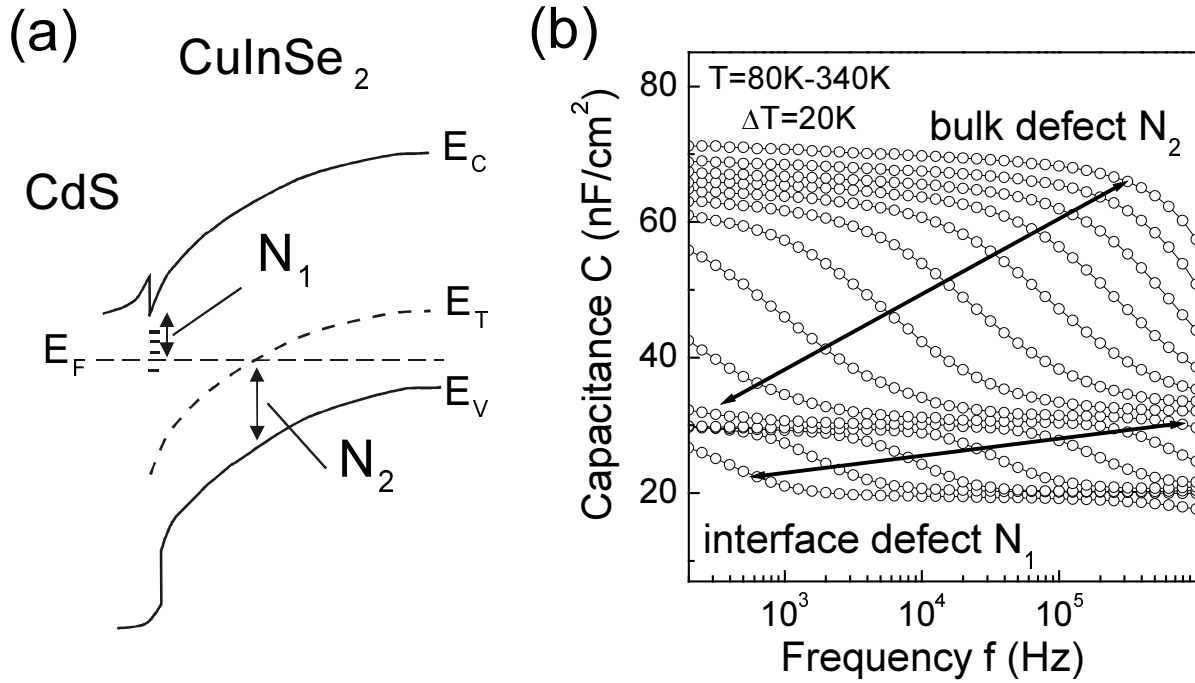

Figure 15. (a) Qualitative equilibrium band diagram of the chalcopyrite absorber and the alignment with the CdS buffer layer. The quantities E_C, E_V, and E_F denote the conduction band, the valence band, and the Fermi energy, respectively. A spatially discrete distribution of defect states at the interface is involved in the transition N_1. The transition N_2 is due to charging and discharging of the bulk acceptors E_T. (b) Generic capacitance vs. frequency spectra at different temperatures measured under a small-amplitude ac signal applied to the CuInSe$_2$-based heterojunction (data from Ref. [236]). The capacitance increases with increasing temperature. The contributions of transitions N_1 and N_2 to the total capacitance are also indicated.

As mentioned above, the evaluation routine for the analysis involves the log-derivative $f \times dC/df$ of the capacitance C, the determination of the activation energy E_A of the different transitions from the corresponding Arrhenius plots, and a re-scaling of the frequency axis into activation energies for visualisation and determination of defect densities [233,234]. The procedure used to derive the defect density assumes defect states which are continuously distributed in the volume of the semiconductor [234]. For the trap N_2 this requirement is satisfied. However, in the case of the trap N_1 we deal with a spatially discrete (but energetically continuous) distribution of donor states at the CdS/chalcopyrite absorber interface [234]. Thus, the activation energy of this transition (typical values are between 50 and 200 meV) corresponds to the energy distance $\Delta E_F^{if} = E_C - E_F$ of the Fermi energy E_F to the conduction band energy E_C at the heterointerface [234]. This distance is a measure of the

type inversion at the absorber surface. Air annealing partly neutralizes the interface states and increases the measured activation energy [205,234]. The bulk acceptor responsible for the transition N_2 has an activation energy $E_A = E_T - E_V$ around 280-300 meV in $CuInSe_2$ measured from the valence band maximum E_V, as routinely found by AS [234] and deep level transient spectroscopy (DLTS) [237]. The energy position of this defect remains constant within the alloy system $Cu(In_{1-x}Ga_x)Se_2$ [30] and also pure $CuGaSe_2$ exhibits an acceptor state at the same activation energy [238]. The importance of this defect is given by the fact that its concentration closely limits the open circuit voltage of $Cu(In_{1-x}Ga_x)Se_2$ solar cells [29,30], and hence the trap can be considered as the dominant recombination center in this material.

6.2.   Composition dependence of defect activation energies

The investigations are carried out using two series of absorbers in terms of S/(S+Se) ratio y and Ga/(Ga+In) ratio x: (a) a series of $CuIn(Se_{1-y}S_y)_2$ absorbers with $0 < y < 0.6$ and (b) a series (mainly according to Ref. [207]) of $Cu(In_{1-x}Ga_x)(Se_{1-y}S_y)_2$ absorbers with $x = 0.3 \pm 0.08$ and $0 < y < 0.7$. The present investigations concentrate on slightly Cu-poor material (Cu/(Cu+In+Ga) ratio ≈ 0.45). This is the material composition that is currently used to produce photovoltaic grade $Cu(In,Ga)(Se,S)_2$ [2].

Figure 16 shows selected capacitance spectra of $Cu(In_{1-x}Ga_x)(Se_{1-y}S_y)_2$ heterostructures at various S contents in the absorber material, corresponding to series (a) with $x = 0$ and (b) with $x \approx 0.3$. The capacitance C decreases with increasing frequency f and with decreasing temperature T. At high temperatures, the bulk defects bring the main contribution to the total capacitance via transition N_2 in Figure 15 and the step at lower temperatures in the capacitance spectra corresponds to the transition N_1 due to interface states [234]. The region of almost constant C at low temperatures in the spectra corresponds to the space charge capacitance of the junction [234,238]. This capacitance generally decreases with increasing sulphur content in the absorber, indicating a widening of the space charge region [72]. In some cases (e.g., the device with $y = 0.7$ in Figure 16b), because of the freeze-out of majority carriers at high frequencies and low temperatures, the capacitance C approaches the lowest limit which represents the geometric capacitance of the device [238]. Under these circumstances, the heterojunction behaves like a plate capacitor between the ZnO window layer and the Mo back contact [238]. Due to the lack of conductivity in the bulk of the

absorber, a single large capacitance step is detected for high sulphur contents (not shown). This behavior is dominant for $y > 0.7$ and therefore, in this compositional range the investigation of trap contributions to the junction capacitance and the evaluation of the defect densities are obstructed.
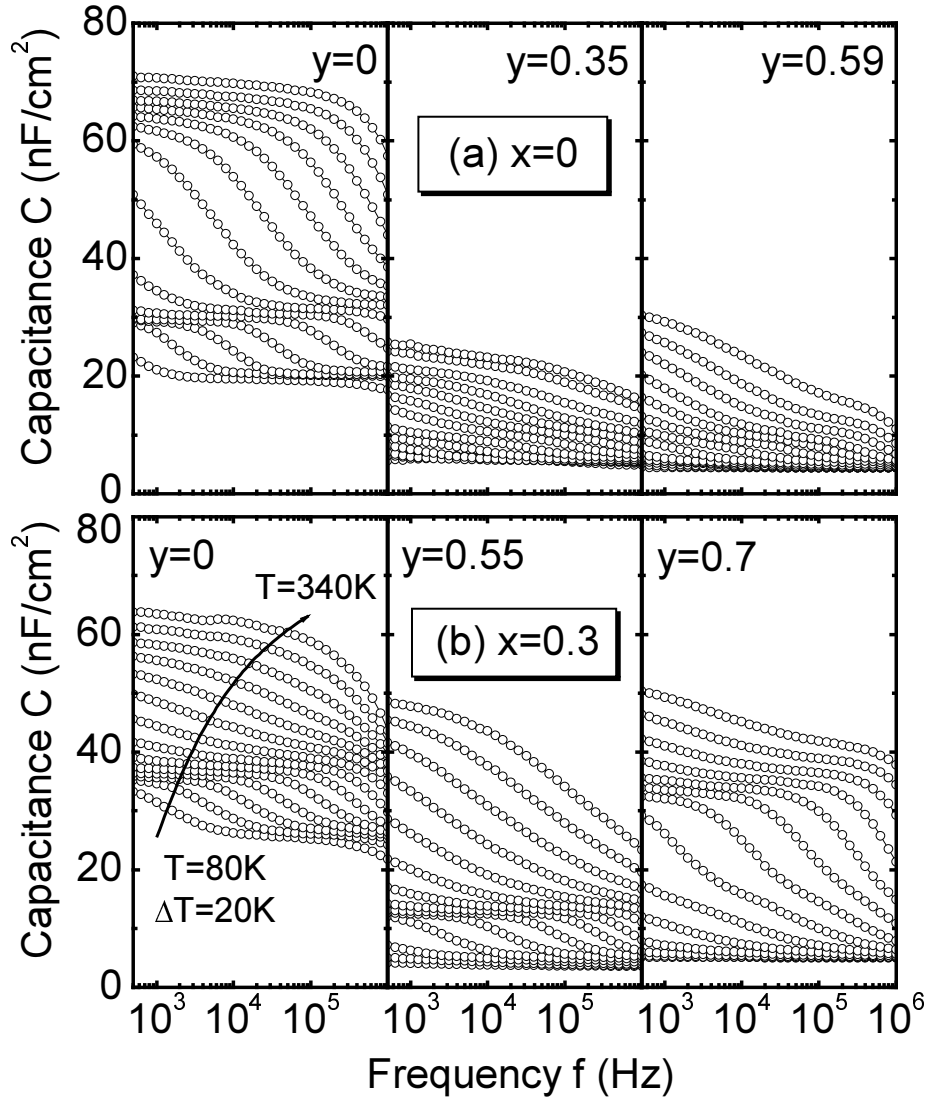

Figure 16. Capacitance spectra of ZnO/CdS/Cu(In$_{1-x}$Ga$_x$)(Se$_{1-y}$S$_y$)$_2$ heterostructures based on absorbers with (a) x = 0 and (b) x ≈ 0.3, and with various sulphur contents. The values of the y parameter are indicated for the individual spectra. The spectra are recorded between 80 K and 340 K with a temperature step of 20 K. The capacitance spectra for y = 0 in (a) are the same as in Figure 15(b) [236].

In order to analyze the defect contribution to the total junction admittance, the inflexion frequencies f_i are extracted from the derivative of the capacitance spectra and the activation energy for each transition is determined according to eq. (13) from the slope of the Arrhenius plots of $2\pi f_i / T^2$ vs. $1/T$ [234]. The Arrhenius data corresponding to the

transitions N_1 and N_2 as extracted from the capacitance spectra of Figure 16 are shown in Figure 17 for $Cu(In_{1-x}Ga_x)(Se_{1-y}S_y)_2$ absorbers with (a) $x = 0$ and (b) $x \approx 0.3$. The values of the corresponding activation energies are listed in Table III.
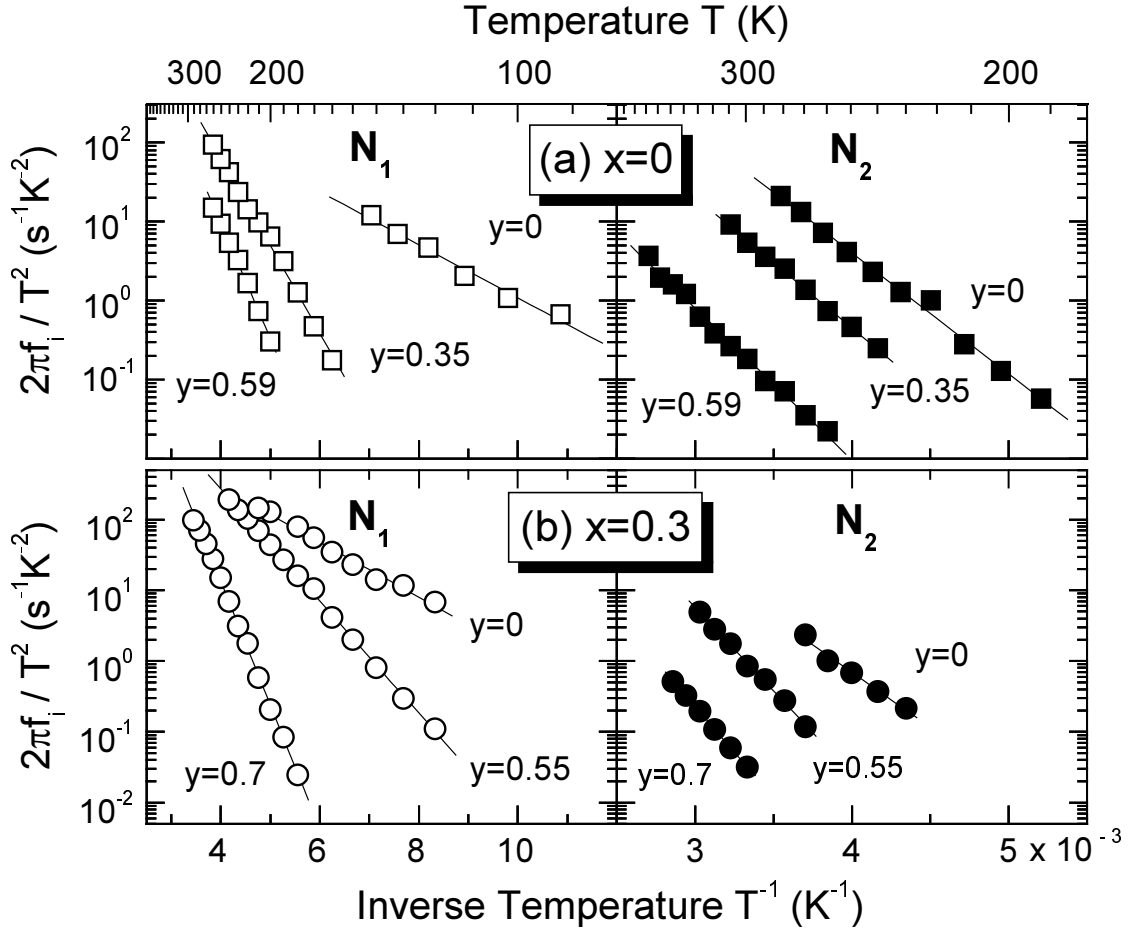

Figure 17. Arrhenius plots of the inflexion frequencies constructed from the capacitance spectra of Figure 16, corresponding to $Cu(In_{1-x}Ga_x)(Se_{1-y}S_y)_2$ heterostructures with (a) $x = 0$ (squares) and (b) $x \approx 0.3$ (circles). The two transitions N_1 and N_2 are represented by open and full symbols, respectively.

Table III. Activation energies $\Delta E_F{}^{if}$ of transition N_1 and E_A of transition N_2, as determined from the Arrhenius plots of the $Cu(In_{1-x}Ga_x)(Se_{1-y}S_y)_2$ heterostructures in Figure 17.

Composition		Activation Energy (meV)	
x	y	$\Delta E_F{}^{if}$ (N_1)	E_A (N_2)
	0	67	304
0	0.35	221	328
	0.59	290	381
	0	77	308
0.3	0.55	157	470
	0.7	347	508

Both activation energies increase with increasing S/(S+Se) ratio y. This behavior is more pronounced in the case of transition N_1. However, for the second transition, a total shift of 200 meV (Figure 17(b) and Table III, $x \approx 0.3$) is observed for the activation energy between $y = 0$ and $y = 0.7$. The energetic distributions of defects for the $Cu(In_{1-x}Ga_x)(Se_{1-y}S_y)_2$ - based heterojunctions with (a) $x = 0$ and (b) $x \approx 0.3$, determined according to the procedure of Walter et al. [233,234] using the Arrhenius data of Figure 17, are displayed in Figure 18.
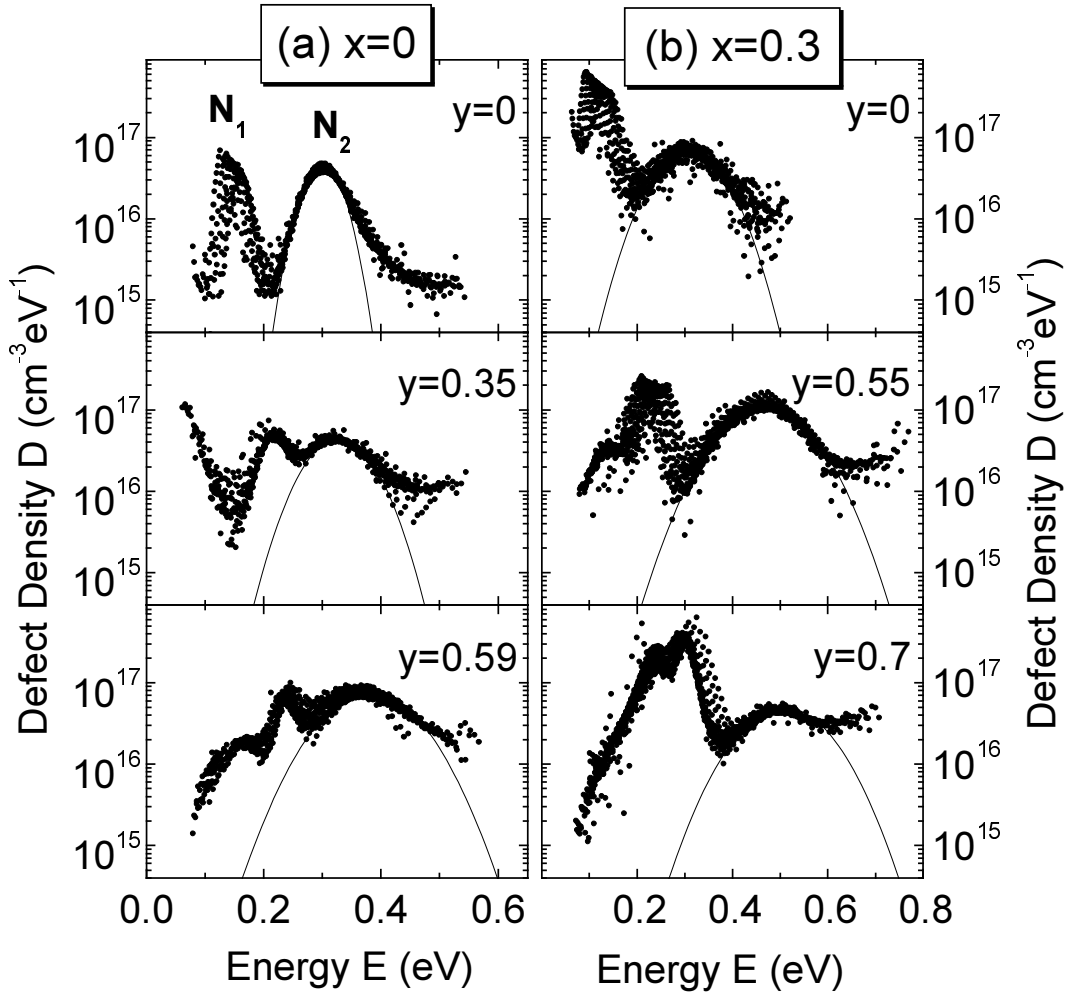
Figure 18. Defect spectra of $Cu(In_{1-x}Ga_x)(Se_{1-y}S_y)_2$ heterostructures with (a) x = 0 and (b) x ≈ 0.3, for different values of the y ratio (the spectrum for y = 0 in (a) from Refs. [30,236]). The spectra are scaled according to Refs. [233,234] using the Arrhenius data of transition N₂ in Figure 17. The spectra are displayed after manually removing the noise in different regions of the calculated spectra. The same was performed in Figure 4 in Ref. [283(b)].

The two maxima of the defect distributions corresponding to the interface donor N_1 and to the bulk acceptor N_2 are clearly visible in all the spectra. As the S content increases, a third peak at lower energies becomes dominant due to the freeze-out of the free carriers in the absorber, as mentioned above. The shift of both peaks N_1 and N_2 towards midgap energies with increasing y can be observed in the spectra, as reflected from the Arrhenius plots.

Since the admittance spectroscopy cannot distinguish between defect states close to the valence band edge or conduction band edge [233], the donor/acceptor character of the detected traps is established by additional deep level transient spectroscopy measurements (not shown). For CuGaSe$_2$ [238] or etched *Cu-rich* CuInS$_2$ [235,239], majority carrier traps have been reported in a range of activation energies not far from the values listed in Table III. However, the transition N$_1$ is identified in the present work as a minority carrier trapping process and the transition N$_2$ as a majority carrier trapping process since the two transitions exhibit different signs of the DLTS signal in the measurements (analogous to the case of standard CuInSe$_2$ material [234]).
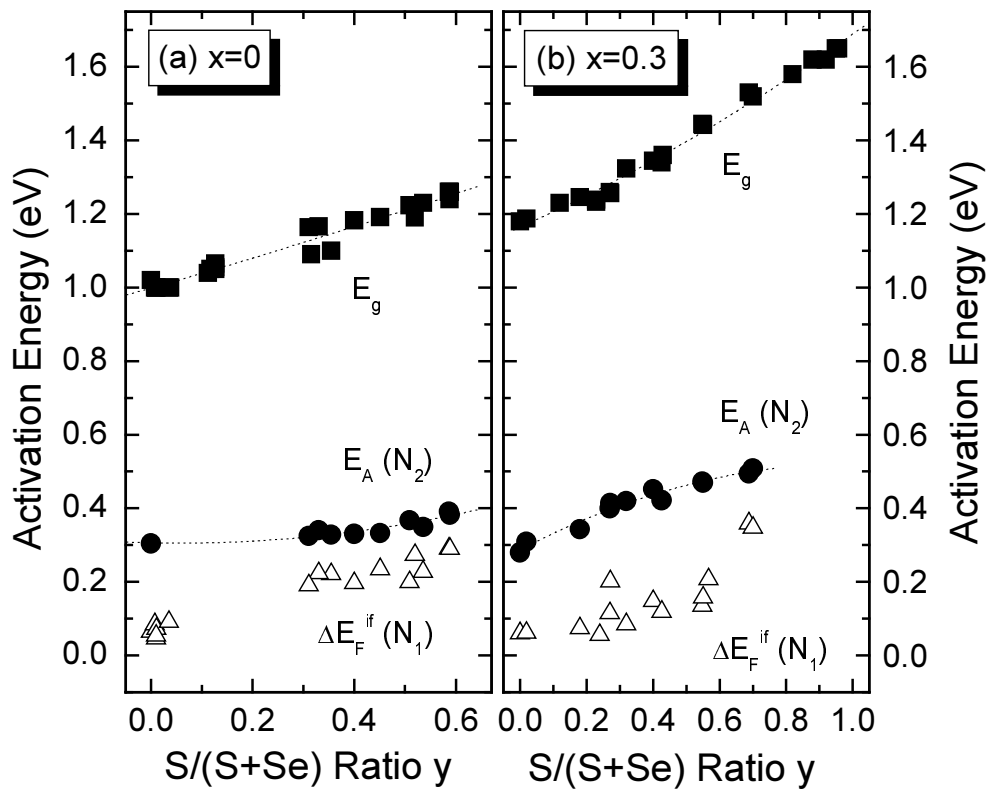
Figure 19. Dependence of the activation energies E_A of transition N_2 (full circles), ΔE_F^{if} of transition N_1 (open triangles) and that of the band gap energy E_g (full squares) on the S/(S+Se) ratio y for Cu(In$_{1-x}$Ga$_x$)(Se$_{1-y}$S$_y$)$_2$ alloys with (a) x = 0 and (b) x ≈ 0.3. Data for y = 0 in the series (a) and (b) are included from Ref. [236]. The data point $^{(i),(ii)}$ (open triangle) with $\Delta E_F^{if}(N_1)$ = 201.5 meV, y = 0.271 in Figure 19(b) is excluded from subsequent figures. For the uncertainties of defect activation energy see Appendix D. The data points with y > 0.8 in Figure 19(b) correspond to absorbers which possibly have Cu-rich composition, see also Figure 5(b) in Ref. [283(b)].

The dependence of the activation energies ΔE_F^{if} of transition N$_1$ and E_A of transition N$_2$ on the S/(S+Se) ratio *y* is summarized in Figure 19 for the two series of Cu(In$_{1-x}$Ga$_x$)(Se$_{1-y}$S$_y$)$_2$ heterostructures with (a) x = 0 and (b) x ≈ 0.3. The dependence of the band gap energy E_g on composition, as determined from the evaluation of quantum efficiency spectra of the

heterojunctions in Appendix B, is also shown. Note that the available data are somewhat restricted by the lack of an unambiguous transition N_2 (especially for $0 < y < 0.3$ in the case of $CuIn(Se,S)_2$ system) and by the lack of bulk conductivity (for $y > 0.7$). However, the general increase of both activation energies as well as of the band gap energy with increasing sulphur fraction in the absorber is clearly seen.

6.3. Band gap evolution diagrams

Following the procedure used to align the valence and conduction band energies for different semiconductor systems [58], the reference energy is set as equal to the energy level E_T of the bulk acceptor state N_2. The dependence of band edge energies as a function of S/(S+Se) composition is then determined according to $E_V = -E_A$ and $E_C = E_g - E_A$. The resulting band gap evolution diagrams for $Cu(In_{1-x}Ga_x)(Se_{1-y}S_y)_2$ alloys with (a) $x = 0$ and (b) $x \approx 0.3$ are shown in Figure 20(a),(b), respectively.
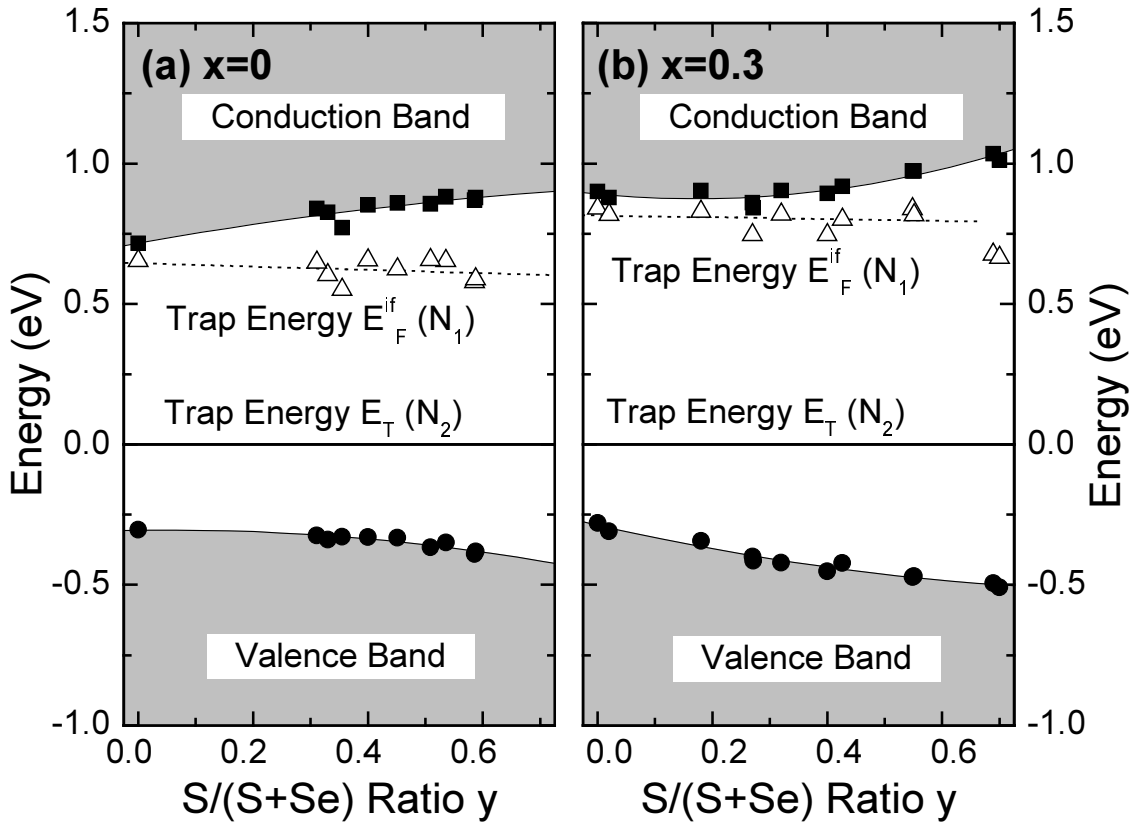

Figure 20. Composition dependence of the valence band and conduction band edge energies E_V (full circles) and E_C (full squares) of $Cu(In_{1-x}Ga_x)(Se_{1-y}S_y)_2$ alloys with (a) $x = 0$ and (b) $x \approx 0.3$, as reconstructed from the data in Figure 19 with $E_V = -E_A$ and $E_C = E_g - E_A$. Also shown is the Fermi energy $E_F{}^{if}$ (open triangles) at the CdS/absorber interface calculated from $E_F{}^{if} = E_g - E_A - \Delta E_F{}^{if}$.

One can conclude from the diagrams that the band gap enlargement with increasing y is accommodated, approximately to the same amount, in the lowering of E_V and the simultaneous rise of E_C. Also shown in Figure 20 is the energy level E_F^{if} of the interface transition N_1 which is computed from the measured values according to $E_F^{if} = E_g - E_A - \Delta E_F^{if}$. The present data indicate that the Fermi level at the CdS/Cu(In$_{1-x}$Ga$_x$)(Se$_{1-y}$S$_y$)$_2$ interface has approximately a fixed energy distance to that of the bulk acceptor for mixed-anion chalcopyrite alloys. Differences of approximately 625 meV and 800 meV are found between the two trap levels for the gallium-free and gallium-containing series of absorbers. Additionally, the data indicate that the Fermi level shifts upward on the energy scale under Ga addition into the absorber, a tendency which will be also seen in Chapter 7 in case of Cu-rich chalcopyrites.
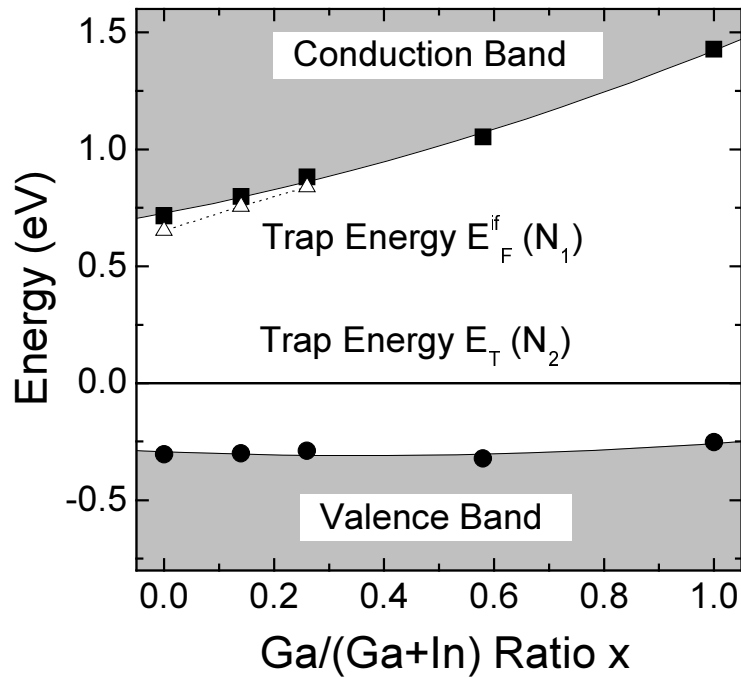

Figure 21. Dependence of the valence band and conduction band edge energies E_V (full circles) and E_C (full squares) of Cu(In$_{1-x}$Ga$_x$)Se$_2$ alloys on the Ga/(Ga+In) ratio x constructed from the defect data in Refs. [30,236,238] in the same way as Figure 20. Also included is the energy E^{if}_F (open triangles) at the Cu(In,Ga)Se$_2$/CdS interface.

In the light of the present results for S/Se alloying, the up to now unspectacular finding that the acceptor defect N_2 does hardly change its energy position upon alloying CuInSe$_2$ with Ga gets a renewed importance. Figure 21 plots the data from Refs. [30,236,238] using the same procedure as for S/Se alloys. As it follows from the diagram, the valence band energy of CuGaSe$_2$ is very close to that of CuInSe$_2$, the difference being smaller than 40 meV. This finding is compatible with the calculations of Wei and Zunger [240] in the frame of the

phenomenological common-anion rule [241] stating that the valence band offset between semiconductors which share an anion - Se, in this case - and have the same crystal structure is small (the breakdown of this rule has already been shown in some semiconductor systems involving zinc-blende type compounds [68,126,242,243] due to massive participation of cation d orbitals to the upper valence band; however, the rule still holds in the chalcopyrite alloys for both mixed I-valent cation and mixed III-valent cation systems [244]). Also shown in Figure 21 is the energy position of the transition N_1, computed with reference to the conduction band energy. In contrast to the situation for (S,Se) alloying, in the case of Cu(In,Ga)Se$_2$ alloys, the transition N_1, where measurable, seems to follow the conduction band rather than being fixed to the reference level.

In the atomic orbital description, as already mentioned in Section 3.1.2, the valence band maximum in chalcopyrites is dominated by the repulsive interaction between inner Cu d orbitals and the anion (Se, S) p orbitals [137,171,240]. Thus, since the valence band offset will mainly reflect the differences between anion p orbital energies, large valence band offsets are characteristic for common-cation chalcopyrites (S/Se alloys), while for common-anion chalcopyrites (Ga/In alloys) most of the band offset is in the conduction band [240].

Some notes are mandatory here, although. First, detailed analysis of the present data indicates a possible effect of gallium upon the valence band maximum in S-containing chalcopyrites (in contrast to S-free chalcopyrites). Down-shifts of the valence band edge of about 100 meV when the Ga/(Ga+In) ratio y increases from 0 to ~ 0.3 have been observed at moderate contents of incorporated sulphur. As already proposed [38], Ga could have a certain effect upon the valence band maximum in the presence of sulphur, whereas it does not influence the valence band energy in CuInSe$_2$. Second, the commutativity and transitivity (see Section 2.11) of band lineups have been tacitly assumed as holding properties in the present investigations. As a result of commutativity, the influence of the interface on the band offset is negligible compared to the bulk contribution. This is not ambiguous since in all heterojunctions the chalcopyrite material under investigation matches an identical CdS/ZnO partner structure. The transitivity implies in the present case that the band alignment of two different alloys in the chalcopyrite system can be entirely derived by referring independently every chalcopyrite alloy to the same (CdS/ZnO) semiconductor partner. This is further supported by a consistent use of the same measurement technique and evaluation procedure in the present investigations. Third, the very shallow defect levels as those investigated by photoluminescence spectroscopy in Chapter 5 behave quite differently than the deep defects investigated in this Chapter. This follows from the pinning of the former to the band edge,

while the latter are not pinned to either of the nearby band edges and therefore are taken as bulk reference levels [58,104]. Finally, for a more refined treatment we should consider that the Arrhenius plots provide the apparent capture cross section and the enthalpy term ΔH [109,112]. The energetic depth of the defect level in the band gap will be then related to the Gibbs free energy $\Delta G = \Delta H - T\Delta S$, where ΔS is the the entropy term [109,112]. Therefore, besides the determination of ΔH, additional sets of measurements are necessary in order to determine the defect level position in the band gap at a given temperature [109,112,245].

6.4.   Numerical values

To quantify the composition dependence of the band gap energy E_g, the data in Figure 20 (for S/Se alloys) and Figure 21 (for Ga/In alloys) are fitted to the quadratic equation [240]

$$E_g(y) = E_g(0) + \Delta E_g y - b_g y(1-y) \ . \tag{15}$$

For the series (a) of S/Se alloys, $E_g(0)$ is the band gap energy of $CuInSe_2$ (1000 meV from the fit in Figure 20(a)), ΔE_g is the band gap difference between $CuInS_2$ and $CuInSe_2$ (447 meV), and b_g (47 meV), the nonlinear coefficient, is a measure of the bowing [240]. In the case of Ga/In alloys we obtain from Figure 21 a similar value (1020 meV) for the band gap energy $E_g(0)$ of $CuInSe_2$, the values of ΔE_g (the band gap difference between $CuInSe_2$ and $CuGaSe_2$) and b_g being now 660 meV and 116 meV, respectively. Though the band gaps for $CuInSe_2$ and $CuInS_2$ from the quantum efficiency analysis appear slightly smaller as compared to literature values (1.04 and 1.53 eV, respectively in Ref. [138]), the difference ΔE_g as well as the bowing coefficients b_g are consistent also with theoretical data ($b_g = 0.04$ eV for $CuInSe_2/CuInS_2$ alloys in Ref. [240]).

In order to determine quantitatively the dependence of the band offsets on composition, we rewrite Eq. (15) for the valence band edge E_V and conduction band edge E_C

$$E_{V/C}(y) = E_{V/C}(0) + \Delta E_{V/C} y - b_{V/C} y(1-y) \ , \tag{16}$$

where b_V and b_C describe the bowing of the valence band edge and conduction band edge, respectively. In this way, the valence and conduction band offsets between $CuInSe_2$ and $CuInS_2$ are $\Delta E_V \approx -233$ meV and $\Delta E_C \approx 214$ meV, the corresponding values for $CuInSe_2/CuGaSe_2$ being now $\Delta E_V \approx 36$ meV and $\Delta E_C \approx 696$ meV, respectively.

Table IV. Differences ΔE_g of the band gap energies between the end-points of the mixed-anion and mixed-cation $Cu(In_{1-x}Ga_x)(Se_{1-y}S_y)_2$ chalcopyrite alloys, and the bowing coefficients b_g for the band gap dependence on the S/(S+Se) ratio y (for the series (a) and (b) of absorbers) and on the Ga/(Ga+In) ratio x. The valence and conduction band offsets ΔE_V and ΔE_C, as well as the bowing coefficients b_V and b_C of the respective systems are obtained by fitting the band energy data in Figure 20 and Figure 21. Literature values in parentheses are indicated for comparison. All values are in meV. An uncertainty of ± 150 meV is estimated for the valence band offsets between $CuInSe_2$ and $CuInS_2$ and between $Cu(In_{0.7}Ga_{0.3})Se_2$ and $Cu(In_{0.7}Ga_{0.3})S_2$, as discussed in Appendix D.

	Band gap		Valence band		Conduction band	
	ΔE_g	b_g	ΔE_V	b_V	ΔE_C	b_C
$CuIn(Se,S)_2$	+447 (+490[b])	+47 (+40[b], 0[c])	-233 (-280[b])	-262	+214 (+210[b])	-148
$Cu(In_{0.7}Ga_{0.3})(Se,S)_2$	+525	+117	-234	+230	+377	+572
$Cu(In,Ga)Se_2$[a]	+660 (+640[b])	+116 (210[b], 140[d], 108[e])	+36 (-40[b])	+126	+696 (+600[b])	+242

[a]fitted values based on data from Refs. [30,236,238]; [b]Ref. [240]; [c]Ref. [246]; [d]Ref. [247]; [e]Ref. [248].

The band gap energy values, the extrapolated band offsets and the corresponding bowing coefficients are summarized in Table IV. Notably, the bowing coefficients b_V and b_C are larger than the total bowing coefficient b_g of the band gap. Nevertheless, a fairly good agreement is seen between the fitted parameters and the recent theoretical first principle calculations of Wei and Zunger [240], or other published experimental values [246-248]. As it follows from the table, identical valence band offsets ΔE_V are found for the end-points of the Ga-free series (a) and Ga-containing series (b) of S/Se alloys in spite of the different signs of the corresponding bowing coefficients, supporting the conclusion that the valence band maximum does not shift under In/Ga alloying.

6.5.   Full width at half maximum

Besides the shift of defect distribution maxima towards higher energies, the defect density spectra indicate a supplementary feature related to the enlargement of the full width at half maximum (FWHM) of the bulk peak N_2 with increasing sulphur and gallium fraction in the absorber. This effect of compositional broadening of the defect peaks is similar to that

observed by photoluminescence or DLTS in $Al_xGa_{1-x}As$ [249], $GaAs_{1-x}P_x$ [250], or $Si_{1-x}Ge_x$ [109,251,252] alloys. As it follows from the Gaussian fits of the defect distributions, an increase of the FWHM of the acceptor peak N_2 in relation with the S content is already visible in Figure 18 for both series of Ga-free and Ga-containing S/Se alloys. However, the width of the donor-related peak N_1 as extracted from the Gaussian fit remains stable under S/Se alloying. A similar trend is found from fitting the data of Hanna et al. [30,236] for Ga/In alloys. Figure 22 reports the general behavior of the full width at half maximum in terms of S/(S+Se) ratio y and Ga/(Ga+In) ratio x.
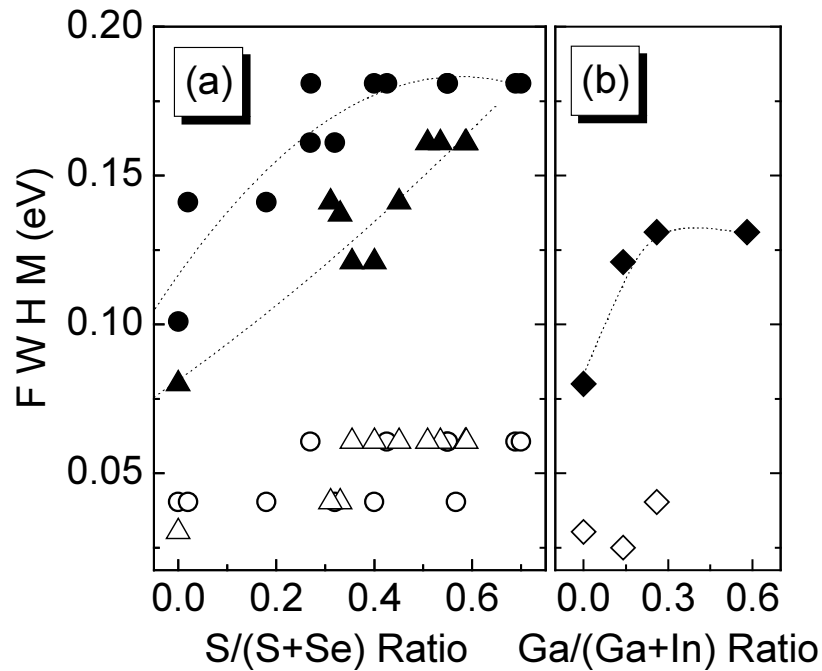
Figure 22. Full width at half maximum[(iii)] *of the acceptor related peak N_2 (full symbols) and of the donor related peak N_1 (open symbols) for $Cu(In_{1-x}Ga_x)(Se_{1-y}S_y)_2$ alloys as a function of the (a) sulphur fraction in the absorber and (b) gallium fraction in the absorber. The series of $Cu(In_{1-x}Ga_x)(Se_{1-y}S_y)_2$ absorbers with x = 0 and with x ≈ 0.3 are represented by triangles and circles, respectively. Values in (b) are obtained from fitting the data from Refs. [30,236]. The same reference data [30,236] corresponding to $CuInSe_2$ composition is used for sulphur-free composition in the series with x = 0 in (a), as the data for gallium-free composition in (b).*

The enlargement of the FWHM appears only in case of transitions related to the valence band (the same trend was reported by Mesli et al. for $Si_{1-x}Ge_x$ [109]). The defect distribution peak N_2 is approximately two times broader in $CuIn(Se_{0.5}S_{0.5})_2$ (or in $Cu(In_{0.5}Ga_{0.5})Se_2$) than its counterpart in $CuInSe_2$. The increased linewidth in alloys is likely to be caused by fluctuations in the band gap energy (e.g., due to variations of the valence band maximum) produced by local inhomogeneities in the alloy composition [109,251]. The statistical fluctuations of S/(S+Se) composition are expected to have a contribution $(\partial E_g / \partial y) \cdot [y(1-y)/(N_L V_0)]^{1/2}$ to the total broadening of spectra, where N_L is the density of

lattice sites and V_0 is the volume of the sphere determined by the Bohr radius of the acceptor [249,251]. This broadening will be maximum at an alloy composition y (or x) = 0.5. Changes of band gap energy with composition and of activation energy of detected maxima will also contribute to the measured linewidths. These considerations obviously do not hold for the defect distribution N_1 corresponding to transitions related to the conduction band at the CdS/absorber interface.

6.6.   Concluding discussion

The use of the dominant acceptor level as an internal reference for the band alignment within the chalcopyrite alloy system shows that the valence band offset $\Delta E_V(y)$ increases together with enlarging the band gap upon alloying CuInSe$_2$ with S. In contrast, $\Delta E_V(x)$ remains close to zero upon alloying CuInSe$_2$ with Ga. The extrapolated band offsets ΔE_V(CuInSe$_2$/CuInS$_2$) = 0.23 eV and ΔE_V(CuInSe$_2$/CuGaSe$_2$) = -0.036 eV, as summarized in Figure 23 and Table IV are in fairly good agreement with theoretical predictions (ΔE_V(CuInSe$_2$/CuInS$_2$) = 0.28 eV, ΔE_V(CuInSe$_2$/CuGaSe$_2$) = 0.04 eV [240]). This fact makes it probable that a strong level pinning of the acceptor state N_2 exists towards a bulk reference level common to the entire alloy system. The reference level sets the band structure on a common energy scale, thus establishing the natural band lineups within the alloy system automatically. The situation is similar to the case of IV-IV, III-V, and II-VI compounds [58,104,105]. In those materials, a level pinning for the transition metal impurities exists towards a bulk reference that is thought to be the 'average' dangling bond energy [64,253]. For the Cu-chalcopyrites, however, the physical nature of the bulk acceptor N_2 as well as of the interface donor N_1 has first to be considered. Analogous to the role of transition metal impurities in III-V and II-IV semiconductors one might think about the acceptor N_2 as a similar defect (Fe being a likely candidate). However, in Cu(In$_{1-x}$Ga$_x$)Se$_2$ this 300-meV acceptor is produced by high-energy electron as well as high-energy proton irradiation [8,19]. This fact makes an intrinsic defect or defect complex more likely. Obviously, alternative experimental approaches and more theoretical work could shed more light onto the physical nature of this defect which appears so important for the Cu-chalcopyrites. The pinning of the dominant acceptor level in Cu(In,Ga)(Se,S)$_2$ system to a constant energy position might be an important ingredient in explaining the outstanding photovoltaic performance and radiation resistance of this material class.
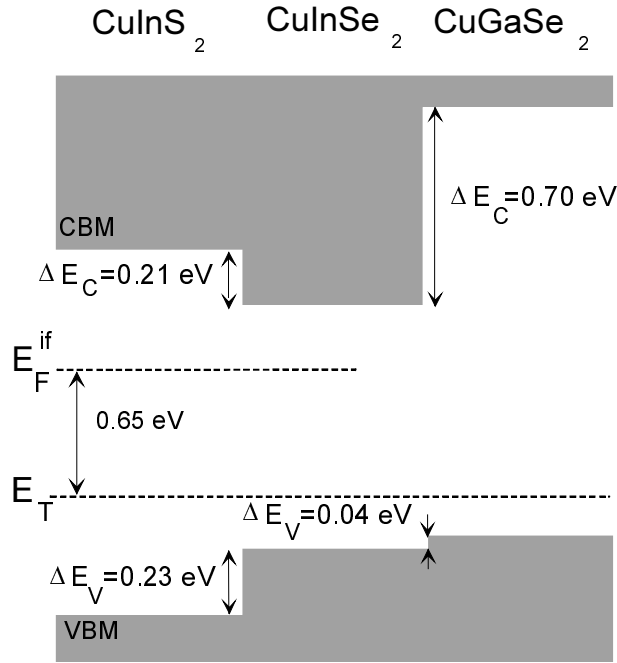
Figure 23. Valence and conduction band offsets ΔE_V and ΔE_C between CuInSe$_2$, CuGaSe$_2$, and CuInS$_2$ derived from the energy position E_T of the acceptor state N$_2$. The energy position E_F^{if} of the interface states N$_1$ is found to be a constant for the CuIn(Se,S)$_2$ system.

The interface donor N$_1$ is associated with (surface) anion (Se,S) vacancies, due to coordinatively unsaturated In or Ga cation states [190,203,205]. The experimental fact that the energy position of these vacancies does not change with S/Se alloying seems plausible as only the second nearest neighbor distance of anion vacancies depends on the S/Se-ratio. At this point, we have to bear in mind that the very surface region of Cu-poor Cu(In,Ga)(Se,S)$_2$ thin films (where the transition N$_1$ is measured) has a stoichiometry and physical properties significantly different from the bulk material (see Section 3.2.3) [190,200,201]. Furthermore, the energy position of the transition N$_1$ can change after exposition to air at elevated temperatures because of the neutralization of the (S,Se) vacancy by substitutional O [205]. Despite of these complications, if we accept the transition N$_1$ to be related to the anion vacancy, this defect would contribute to the 'average' dangling bond, i.e., to the true reference energy which dominates both the band alignments as well as the bulk defect levels. One might speculate that in case of S/Se alloying other contributions to the average dangling bond energy either are energetically constant or compensate each other so that the energy position of the (S,Se) vacancy is maintained as in the present experiments. This statement obviously does not hold for In/Ga alloying such that the energy position of the Se vacancy with respect to the reference level depends on the Ga-content.

On the other hand, the activation energy of transition N$_1$ indicates the energy position E_F^{if} of the Fermi level at the CdS/absorber interface: E_F^{if} remains pinned at an approximately

low energy position in the band gap upon alloying CuInSe$_2$ with S, whereas it rises on the energy scale following the conduction band edge upon alloying CuInSe$_2$ with Ga (similar compositional trends of interface Fermi energy position are found in the quaternary InGaAlAs alloy system from electrical transport analysis of Schottky contacts: the interface Fermi energy remains constant in case of (Ga,In)As alloys and increases under alloying with Al [99,134]). Thus, the interface recombination barrier ϕ_b^p (directly related to E_F^{if}, see Figure 7) increases under Ga addition minimizing interface recombination in Cu-poor Cu(In,Ga)Se$_2$ heterojunctions, and remains at a relatively low value in CuIn(Se,S)$_2$ devices which consequently become more critical to interface recombination. The compositional trends of recombination mechanisms are investigated in more detail in the next Chapter.

_____

[(i)] The data point corresponding to the activation energy $\Delta E_F^{if}(N_1) = 201.5$ meV of transition N$_1$ for the sample with $y = 0.271$ in Figure 19(b) had been excluded from the subsequent analysis in Figure 20(b) and the full width at half maximum for the peak N$_1$ of this sample is also not included in Figure 22(a). The data related to the peak N$_1$ for this sample is not considered in Figure 5(b), Figure 6(b), and Figure 9(a) in Ref. [283(b)].

[(ii)] The compositional S/(S+Se) ratio y of the absorber corresponding to the data points with $y = 0.1$ in Figure 5(b) and Figure 9(a) in Ref. [283(b)] was found to be not correct, thus the respective data points were removed from Figure 19(b) and Figure 22(a) in this thesis.

[(iii)] The full width at half maximum for the defect peaks related to the transitions N$_1$ and N$_2$ is obtained by fitting the respective peaks with Gaussian functions. The fits are not realised using an automatic procedure, but rather by manually superimposing the Gaussian function on the defect peak N$_1$ or N$_2$. For visualisation of the defect peak N$_1$, the defect spectra are scaled, with some possible exceptions, using the factor ξ_0 obtained from Arrhenius plots ($2\pi f_i/T^2$ vs. $1/T$) corresponding to the transition N$_1$. For the peak N$_2$, the values of ξ_0 from Arrhenius plots of the transition N$_2$ are used. In some cases, especially for the samples corresponding to the data points (open circles) with the S/(S+Se) ratio of $y = 0$, $y = 0.02$, and $y = 0.18$ within the series of Cu(In$_{1-x}$Ga$_x$)(Se$_{1-y}$S$_y$)$_2$ alloys with $x \approx 0.3$ shown in Figure 22(a) in this thesis, only one branch of the defect peak N$_1$ was visible for the evaluation of the full width at half maximum. For the sample with $y \approx 0$ used for the peak N$_1$ in Figure 9 in Ref. [283(b)] within the series of CuIn(Se$_{1-y}$S$_y$)$_2$ alloys (the open triangle at S/(S+Se) ratio $y \approx 0$), the evaluation procedure was unsatisfactorily, and the respective value was corrected in Figure 22(a) in this thesis. See also Figure 9 in Ref. [283(b)]).

7.   Electrical transport analysis

This Chapter uses current-voltage and capacitance-voltage analysis to determine the compositional trends of charge carrier recombination in Cu(In,Ga)(Se,S)$_2$ heterojunction solar cells. In contrast to the band offsets, the dominant recombination mechanism is not directly controlled by S/Se or Ga/In alloying, but rather is driven by changes in the Cu-stoichiometry. Whereas the electronic loss in Cu(In,Ga)(Se,S)$_2$ devices with a Cu-poor absorber composition is limited by bulk recombination, Cu-rich heterojunctions are dominated by recombination at the CdS/absorber interface.

7.1.   Basics

The short circuit current density j_{SC} of a solar cell is limited by optical losses because not all the incident photons generate electron-hole pairs, and by recombination losses since a fraction of photogenerated carriers recombine before they are collected [3]. These losses are especially important in wide-gap Cu(In,Ga)(Se,S)$_2$ solar cells which deliver considerably lower open circuit voltage when comparing to the band gap energy of the absorber [34]. It appears that the recombination mechanism changes either qualitatively or quantitatively upon alloying CuInSe$_2$ with high contents of Ga and/or S. Relevant recombination paths at the CdS/absorber interface and in the space charge region or neutral zone of the absorber are considered in Figure 24. Recombination at the back contact and at the grain boundaries might contribute as well to the total recombination loss [2,3], however these recombination paths are neglected in this work. In the presence of high electrical fields the tunneling contribution to recombination can also become important [3].

The recombination current density j_r is written in the form of a diode law [3]

$$j_r = j_0 \left[\exp\left(\frac{qV}{n_{id}\,k_B T} \right) - 1 \right] , \tag{17}$$

where V is the applied voltage, n_{id} is the ideality factor and $k_B T/q$ is the thermal voltage. The saturation current density j_0 generally is a thermally activated quantity [2,3]

$$j_0 = j_{00} \exp\left(\frac{-E_a}{n_{id}\, k_B T}\right) , \tag{18}$$

with j_{00} a weakly temperature-dependent pre-factor and E_a the activation energy. The quantities j_{00}, n_{id}, and E_a depend on the details of the recombination mechanism [3]. At open circuit no current flows across the device and the recombination current density j_r compensates the short circuit current density j_{SC} [3]. Considering only the exponential term in eq. (17), the open circuit voltage V_{OC} ($V_{OC} > 3\, n_{id}\, k_B T/q$) may be written as [2,3]

$$V_{OC} = \frac{E_a}{q} - \frac{n_{id}\, k_B T}{q} \ln\left(\frac{j_{00}}{j_{SC}}\right) . \tag{19}$$

If the interface recombination (path 1 in Figure 24) is the dominant recombination mechanism, the open circuit voltage is given by the expression [2]

$$V_{OC} = \frac{\phi_b^p}{q} - \frac{k_B T}{q} \ln\left(\frac{q S_{if} N_v}{j_{SC}}\right) , \tag{20}$$

where S_{if} is the interface recombination velocity for holes, N_v is the effective density of states in the valence band of the absorber, and ϕ_b^p is the interface barrier as indicated in Figure 24.
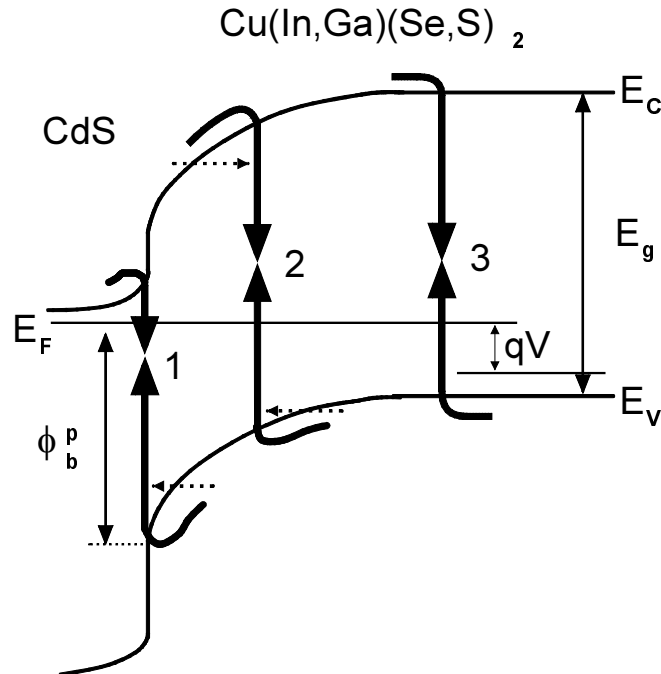

Figure 24. Band alignment at the interface between CdS and the high-gap Cu(In,Ga)(Se,S)$_2$ chalcopyrite, and possible recombination paths at the heterointerface (path 1), in the space charge region (path 2), or in the neutral zone of the absorber (path 3). The quantities E_C, E_V, E_g, and E_F denote the conduction band, valence band, band gap, and electron Fermi energy, respectively, and ϕ_b^p shows the potential barrier for interface recombination. The dotted arrows indicate the tunneling enhancement of the recombination paths 1 and 2.

The V_{OC} limitation due to space charge recombination (path 2), is given by [2]

$$V_{OC} = \frac{E_g}{q} - \frac{2k_B T}{q} \ln\left(\frac{k_B T D_e \pi \sqrt{N_c N_v}}{j_{SC} F_m L_e^2}\right),$$ (21)

where D_e and L_e are the diffusion constant and the diffusion length for electrons, and N_c is the effective density of states in the conduction band of the absorber. The quantity $F_m = (2qN_A V_{bi}/\varepsilon_s)^{1/2}$ denotes the electrical field at the position of maximum recombination and depends on the doping density N_A, on the band bending V_{bi}, and on the dielectric constant ε_s of the absorber [2]. In case of dominant recombination in the neutral zone of the absorber (path 3), the V_{OC} limitation [2] may be written in a form comparable to eq. (21)

$$V_{OC} = \frac{E_g}{q} - \frac{k_B T}{q} \ln\left(\frac{q D_e N_c N_v}{j_{SC} N_A L_e}\right).$$ (22)

Since mechanisms (1) - (3) in Figure 24 are connected in parallel, the strongest one will dominate the recombination loss [3]. This can be seen in Figure 25(a) which displays the calculated values of the open circuit voltage V_{OC} as a function of the electron diffusion length L_e for a CdS/chalcopyrite heterojunction, according to eqs. (20)-(22) [254].
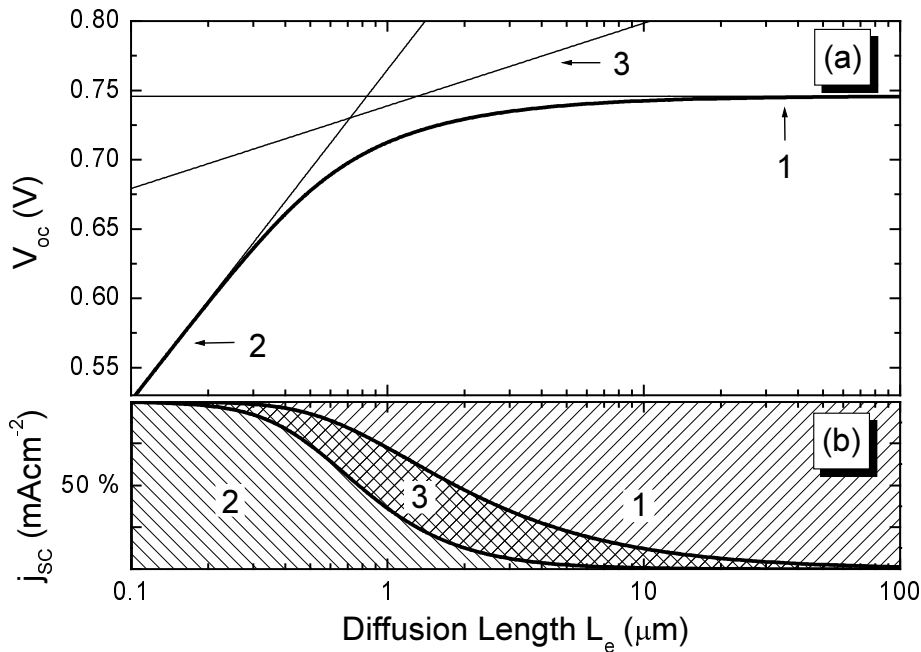

Figure 25. (a) Dependence of the open circuit voltage V_{OC} at 300K on the electron diffusion length L_e in the absorber according to eq. (20) for interface recombination (path 1), to eq. (21) for space charge region recombination (path 2), and to eq. (22) for recombination in the neutral bulk (path 3). (b) Contributions (dashed areas) of individual recombination currents to the total short circuit current j_{SC} for the mechanisms (1) - (3) in (a). The computation is made for a CdS/chalcopyrite device with $S_{if} = 10^4$ cm/s, $\phi_b^p = 1.1$ eV, $V_{bi} = 0.6$ V, $j_{SC} = 27.67$ mA/cm^2, and the bulk properties of the absorber are described by $D_e = 2.59$ cm^2/s, $N_c = 6.7 \times 10^{17}$ cm^{-3}, $N_v = 1.5 \times 10^{19}$ cm^{-3}, $N_A = 3.2 \times 10^{15}$ cm^{-3}, $\varepsilon_s = 8\varepsilon_0$, and $E_g = 1.256$ eV.

The corresponding contributions of individual recombination mechanisms to the total short circuit current of the junction are given as dashed areas in Figure 25(b). At low diffusion lengths, the recombination in the space charge region (path 2) dominates the recombination loss, whereas the limiting mechanism at high diffusion lengths is the recombination at the heterointerface (path 1). The recombination in the neutral zone (path 3) determines in this case a relatively narrow transition regime with a reduced contribution to the total recombination current. Since the recombination in the neutral zone and in the space charge region of the absorber may be in principle thought as similar processes acting in different regions, the corresponding recombination mechanisms are considered together in the following as a bulk recombination. Thus, the activation energy of recombination is considered to be either the band gap energy $E_a = E_g$ in case of recombination in the bulk of the absorber, or the interface barrier $E_a = \phi_b^p$ for recombination at the CdS/absorber interface [255].

Additional information about the recombination mechanisms is provided by the values of the ideality factor n_{id}, preferably over a wide temperature range. For the case of interface recombination and considering the tunneling enhancement, the following expression for the ideality factor is used in this work [255]

$$n_{id} = \frac{1}{\alpha_0} \frac{E_{00}}{k_B T} \coth\left(\frac{E_{00}}{k_B T}\right), \tag{23}$$

where α_0 is a coefficient which takes into account the proportion between the voltage drops on the n and p side of the junction, and the quantity

$$E_{00} = \frac{q\hbar}{2} \sqrt{\frac{N_A}{m^* \varepsilon_s}} \tag{24}$$

is the tunneling energy [3] which depends on the material parameters N_A, ε_s, and on the effective tunneling mass m^*. The ideality factor for tunneling enhanced recombination in the space charge region, considering a distribution of recombination centers with an exponential decay of the trap density from the band edge, is given by the expression [255,256]

$$\frac{1}{n_{id}} = \frac{1}{2}\left(1 + \frac{T}{T^*} - \frac{E_{00}^2}{3\left(k_B T\right)^2}\right), \tag{25}$$

where $k_B T^* = E^*$ is the characteristic energy of the defect distribution. In the limit $T^* \to \infty$, eq. (25) describes tunneling-enhanced recombination via midgap states, while for $E_{00} \to 0$ we obtain $n_{id}^{-1} = (1 + T/T^*)/2$ for the description of classical recombination via an exponential distribution of trap states [255,256].

7.2. Results

The dominant recombination paths in thin-film heterojunction solar cells based on $Cu(In,Ga)(Se,S)_2$ alloys are investigated by current-voltage[(i)] and capacitance-voltage measurements [257]. The absorbers are prepared by coevaporation from elemental sources with the experimental setup described in Section 4.1. A single step evaporation procedure with constant evaporation rates is designed for the preparation of absorbers. Additional samples [207] including absorbers with compositional gradient in the depth[(ii)] are included for the investigations in this chapter. Due to the geometrical arrangement of the evaporation sources, samples with overall Cu-poor and Cu-rich composition are obtained in the same preparation run. The absorber material with Cu-rich composition is etched, with possible exceptions,[(iii)] in KCN solution prior to heterojunction formation to remove the excess $Cu(Se,S)$ secondary phases [166]. The devices are realized according to Section 3.2.1 and the electrical characteristics are recorded with the experimental setup shown in Section 4.5.

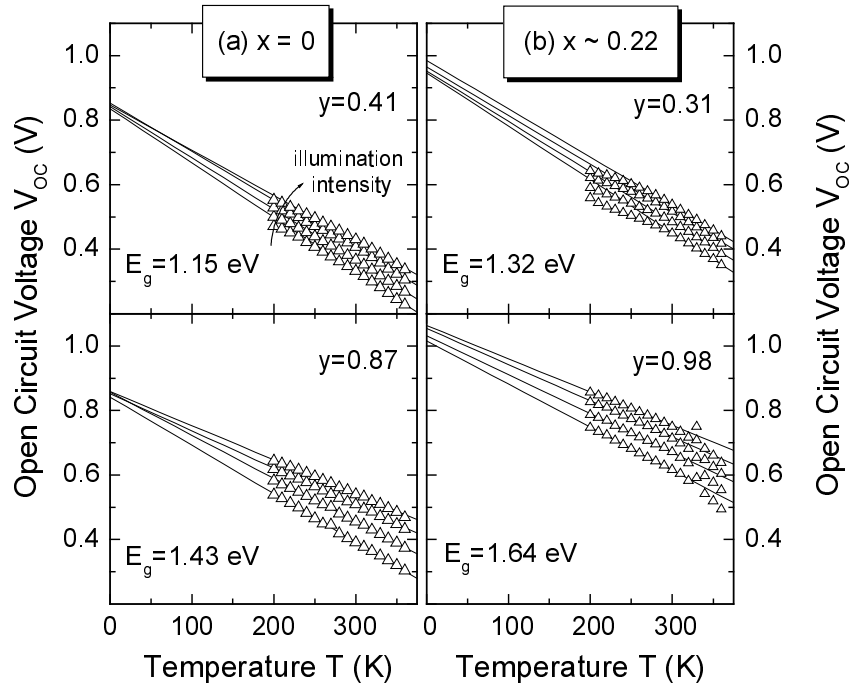### 7.2.1. Activation energy of recombination

Figure 26. Temperature dependence of the open circuit voltage V_{OC} under different illumination intensities (10, 20, 50, 100 mW/cm^2) for Cu-rich ZnO/CdS/Cu(In$_{1-x}$Ga$_x$)(Se$_{1-y}$S$_y$)$_2$ devices with different y ratios and with (a) x = 0, and (b) x $\approx$ 0.22. The extrapolation of V_{OC} towards 0 K leads to values substantially smaller than the band gap energy E_g/q of the absorbers. The extrapolated values increase with increasing x ratio and apparently are not considerably modified under different S/(S+Se) ratio y within each pair (a) and (b) of devices.

According to eq (19), if n_{id}, j_{SC}, and j_{00} are temperature-independent, the open circuit voltage V_{OC} should display a linear dependence on temperature and therefore the extrapolation of the V_{OC} vs. T plot to $T = 0$ K gives the activation energy E_a of recombination [255]. The procedure is illustrated in Figure 26(a),(b) for Cu-rich ZnO/CdS/Cu(In$_{1-x}$Ga$_x$)(Se$_{1-y}$S$_y$)$_2$ heterojunction solar cells with different y ratios and with (a) $x = 0$, and (b) $x \approx 0.22$. The open circuit voltages extrapolate to 0 K to values substantially smaller than the band gap energies E_g/q of the respective absorbers for all Cu-rich devices.

If the ideality factor n_{id} becomes strongly temperature dependent, a more refined evaluation scheme is required. In this case, the reorganization of eq. (18) yields the relationship [255]

$$n_{id} \ln(j_0) = \frac{-E_a}{k_B T} + n_{id} \ln(j_{00}) \ .$$ (26)

Thus, a plot of corrected saturation current density (or corrected saturation current) $n_{id} \, ln(j_0)$ vs. inverse thermal energy $1/k_B T$ should yield a straight line and the slope provides E_a [255].
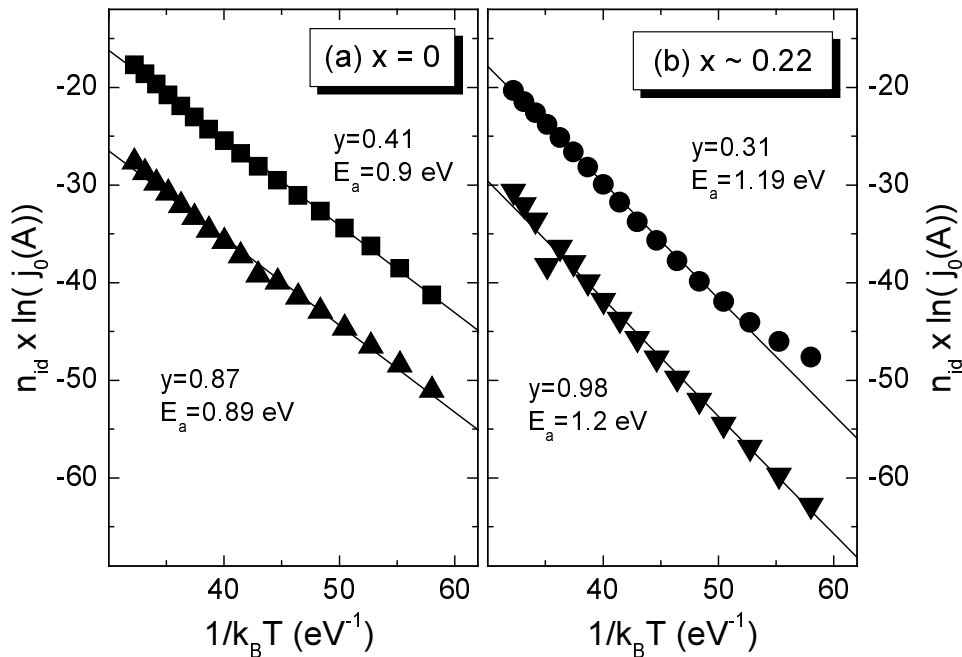

Figure 27. The corrected saturation current n_{id} ln(j_0) versus inverse thermal energy $1/k_B T$ for the Cu-rich ZnO/CdS/Cu(In$_{1-x}$Ga$_x$)(Se$_{1-y}$S$_y$)$_2$ heterojunctions in Figure 26, with different y parameters and with (a) x = 0, and (b) x ≈ 0.22. The slopes provide the activation energies E_a of the recombination process. Cell area is 0.5 cm^2.

In the present analysis, the saturation currents j_0 and the ideality factors n_{id} are obtained from the analysis of the illuminated current voltage characteristics by plotting $ln(j_{SC})$ vs. V_{OC} for different illumination intensities [29]. The modified Arrhenius plots of $n_{id} \, ln(j_0)$ vs. $1/k_B T$ for the same Cu(In$_{1-x}$Ga$_x$)(Se$_{1-y}$S$_y$)$_2$ - based heterojunctions of Cu-rich composition

as those in Figure 26 are shown in Figure 27. The slopes of the Arrhenius plots yield activation energies which are similar to the extrapolated values of V_{OC} to $T = 0$ in Figure 26. Thus, for the Cu-rich devices shown above, the dominant recombination mechanism is localized at the interface and the activation energy gives the barrier ϕ_b^p .
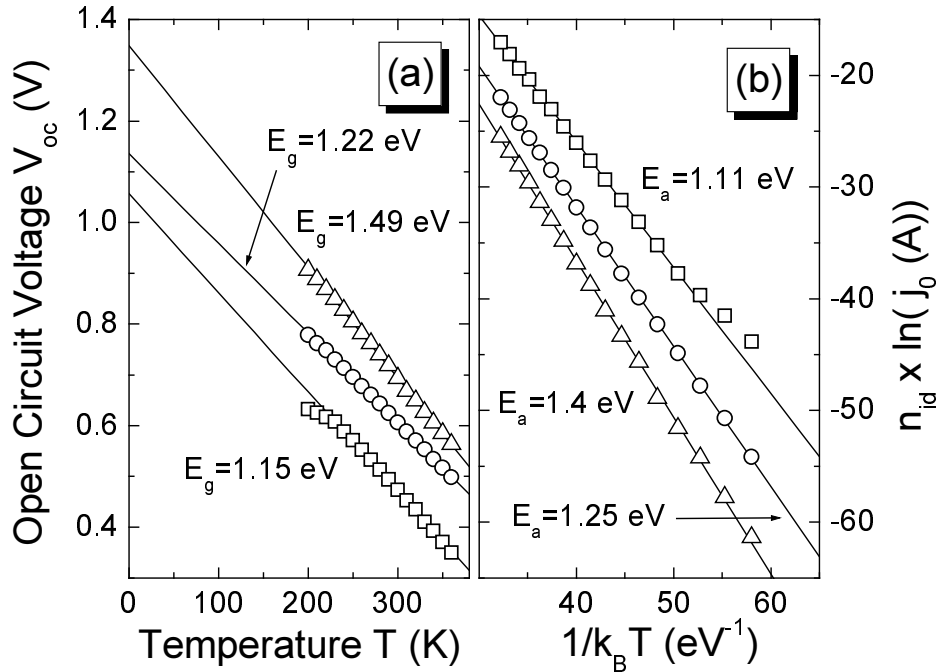

Figure 28. (a) Extrapolation of the open circuit voltage V_{OC} (measured under 100 mW/cm^2 illumination intensity) towards 0 K for Cu-poor ZnO/CdS/Cu(In$_{1-x}$Ga$_x$)(Se$_{1-y}$S$_y$)$_2$ devices with different band gap energies E_g of the absorber. (b) Arrhenius plots of the corrected saturation current $n_{id} ln(j_0)$ for the corresponding heterojunctions in (a). The activation energy E_a of recombination follows the band gap energy of the absorber; squares: x = 0, y = 0.39; circles: x = 0.25, y = 0.27; triangles: x = 0.31, y = 0.54. Cell area is 0.5 cm^2.

In turn, when investigating Cu-poor Cu(In$_{1-x}$Ga$_x$)(Se$_{1-y}$S$_y$)$_2$ - based heterojunctions, the electronic loss in these devices is dominated by bulk recombination. Figure 28(a),(b) displays the temperature dependence of the open circuit voltage V_{OC} and the corresponding modified Arrhenius plots of $n_{id} ln(j_0)$ vs. $1/k_BT$ for devices based on Cu-poor absorbers with different compositions and band gap energies. The activation energies extracted either from extrapolated values of V_{OC} to $T = 0$ (Figure 28(a)), or from the slopes of the Arrhenius plots (Figure 28(b)) follow the band gap energy of the respective absorbers, as expected for bulk recombination.

Figure 29 plots the activation energy E_a of recombination obtained from corrected Arrhenius plots as a function of the absorber band gap energy E_g for various devices based on Cu-poor and Cu-rich Cu(In$_{1-x}$Ga$_x$)(Se$_{1-y}$S$_y$)$_2$ absorbers with various y and with $x = 0$, and with $x \approx$ 0.25 ($x = 0.25 \pm 0.12$). The band gap values are determined in Appendix B from the

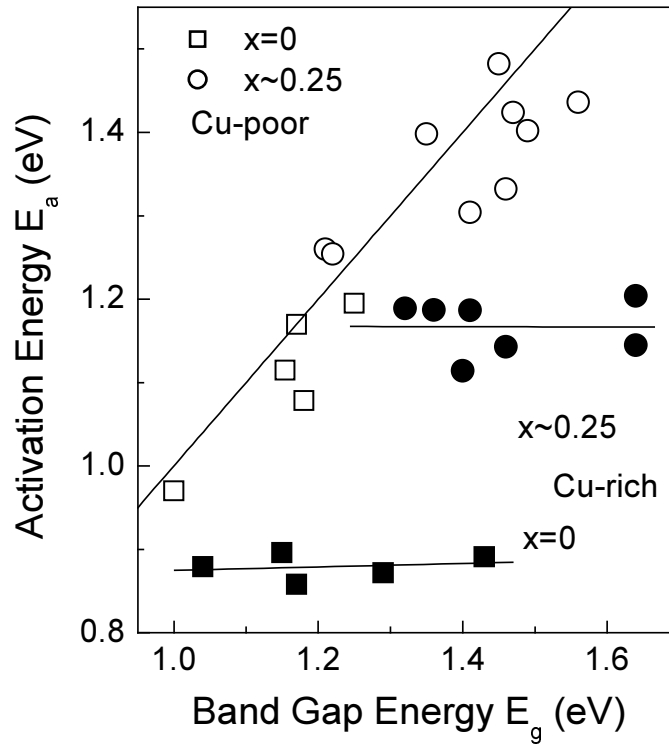absorption edge in the quantum efficiency spectra of the respective heterostructures.

Figure 29. Activation energy E_a of the recombination process as a function of the band gap energy E_g of Cu-poor (open symbols) and Cu-rich (full symbols) $Cu(In_{1-x}Ga_x)(Se_{1-y}S_y)_2$ absorbers with various y and with x = 0 (squares), and x $\approx$ 0.25 (x = 0.25 $\pm$ 0.12) (circles). The activation energy for the Cu-poor devices follows the band gap energy of the absorber material. In the case of Cu-rich devices, the activation energy is independent from the band gap energy E_g as long as the variation of E_g is achieved by varying the S/(S+Se) ratio y at a constant Ga/(Ga+In) ratio x. The correspondence $E_a = E_g$ is shown for the Cu-poor devices and the solid lines for the Cu-rich devices are fits to the data. The value of the absorber band gap energy $E_g = 1$ eV for the sample with E_a =0.97 eV is estimated using a different sample based on absorber material prepared in the same preparation run. For uncertainties in the determination of the activation energy of recombination see Appendix E.

Let us first evaluate the absorbers grown with a Cu-rich final composition. Here, the activation energy of all $CuIn(Se_{1-y}S_y)_2$ - devices is approximately 0.9 eV independently from E_g. The same statement remains valid for the Cu-rich $Cu(In_{1-x}Ga_x)(Se_{1-y}S_y)_2$ - devices with x $\approx$ 0.25 which exhibit activation energies E_a of around 1.1 eV again independent from E_g. Thus, $E_a < E_g$ holds in all Cu-rich devices which are therefore dominated by interface recombination and the measured E_a corresponds to the potential barrier ϕ_b^p (see Figure 24). Interestingly, this barrier is not affected by the S/Se ratio, whereas an increase of the Ga/(Ga+In) ratio x increases ϕ_b^p by about the same amount as E_g is increased by the Ga admixture. Apparently, the decrease of E_V in the bulk of the absorber under S/Se alloying

[240], as found for Cu-poor chalcopyrites in Chapter 6, is compensated by a decreasing Fermi energy position at the heterointerface such that the barrier ϕ_b^p remains constant. In turn, the increase of ϕ_b^p with increasing Ga/(Ga+In) ratio x must result from an upward shift of the Fermi level at the interface because the position of the valence band maximum E_V in the bulk remains constant when alloying CuInSe$_2$ with Ga [240].

On the other hand, the activation energies derived from the Cu-poor devices in Figure 29 follow the band gap energy E_g regardless whether the band gap variation is achieved by alloying with S or Ga. Thus, all Cu(In,Ga)(Se,S)$_2$ devices grown with a final Cu-poor composition are dominated by bulk recombination.
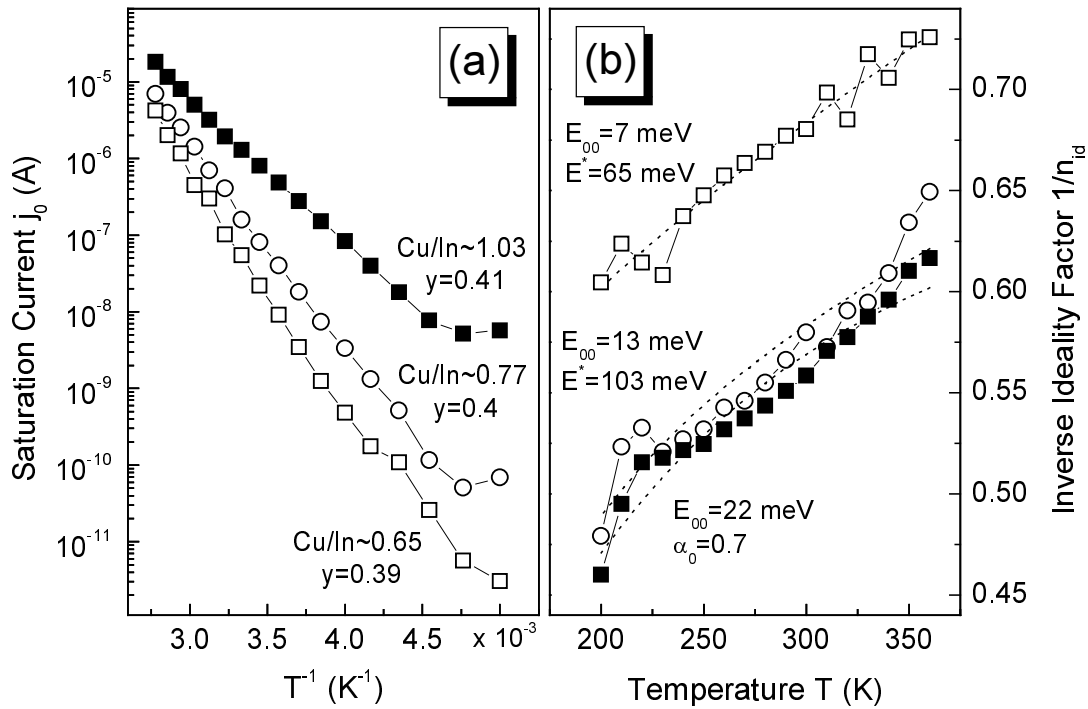
7.2.2. Tunneling contribution

Figure 30. (a) Temperature dependence of saturation current j_0 of CuIn(Se$_{1-y}$S$_y$)$_2$-based solar cells with Cu/In ratios of 0.65 (open squares, y = 0.39), 0.77 (open circles, y = 0.4), and 1.03 (full squares, y = 0.41). (b) Temperature dependence of the inverse ideality factors for the heterojunctions in (a). Numerical fits and the respective extracted parameters (the tunneling energy E_{00} and the characteristic energy $E^* = kT^*$ or the coefficient α_0) according to tunneling enhanced bulk recombination model [eq. (25)] are shown for the Cu-poor devices and to the tunneling enhanced interface recombination model [eq. (23)] for the Cu-rich devices. The tunneling energy increase with increasing Cu/In ratio. Cell area is 0.5 cm^2.

Having now determined the dominant recombination paths in relation with the Cu-stoichiometry, it is useful to consider the contribution of tunneling. As mentioned in Section

7.1, tunneling may enhance both the interface and the bulk recombination, especially in the presence of high electrical fields [3]. The dependencies on the temperature of the ideality factors and of the respective saturation currents are shown in Figure 30 for devices based on $CuIn(Se_{1-y}S_y)_2$ absorbers with y ratios close to 0.4 and with Cu-poor and Cu-rich compositions. Both the ideality factors and the saturation currents are obtained from illuminated characteristics using plots of short circuit current vs. open circuit voltage under different illumination intensities, as in the preceding section. The saturation currents j_0 and the ideality factors n_{id} of the devices in Figure 30 increase with increasing Cu/In ratio in the whole temperature range under investigation. The plots of inverse ideality factors in Figure 30(b) allow a quantitative evaluation [255] by fitting the experimental data for the Cu-poor devices (tunneling enhanced bulk recombination) to eq. (25) and for the Cu-rich device (tunneling enhanced interface recombination) to eq. (23). In both cases the tunneling energy E_{00} (eq. (24)) measures the contribution of tunneling to the specific recombination process [255]. Increasing E_{00} values with increasing Cu/In ratio in Figure 30(b) indicate a stronger contribution of tunneling to the recombination in the Cu-rich devices than in the Cu-poor counterparts. This finding is supported by the results of capacitance-voltage analysis, as discussed in the following.

7.2.3. *Doping densities*

In this section, capacitance-voltage measurements are used to estimate the doping density of the absorber for the heterojunctions under investigation [257]. In general, considering for example a n^+p junction, if the capacitance C of the device is measured as a function of the applied voltage V, a plot of $1/C^2$ vs. V should yield a straight line in the depletion layer approximation, and the doping density N_A of the p-type semiconductor is determined from the slope [72]

$$\frac{d\left(1/C^2\right)}{dV} = \frac{2}{q\varepsilon_s N_A} \quad . \tag{27}$$

Although at room-temperature both the net doping concentration and the deeper trap states contribute to the electrical field at the junction [255], the defect contribution is neglected in the following *C-V* analysis. Figure 31 shows capacitance-voltage measurements and $1/C^2$ vs. V plots for devices based on $CuIn(Se_{1-y}S_y)_2$ absorbers with $y \approx 0.4$ and with Cu-poor and Cu-rich compositions. As one can see in Figure 31, the doping density into the absorber increases with increasing Cu/In ratio.
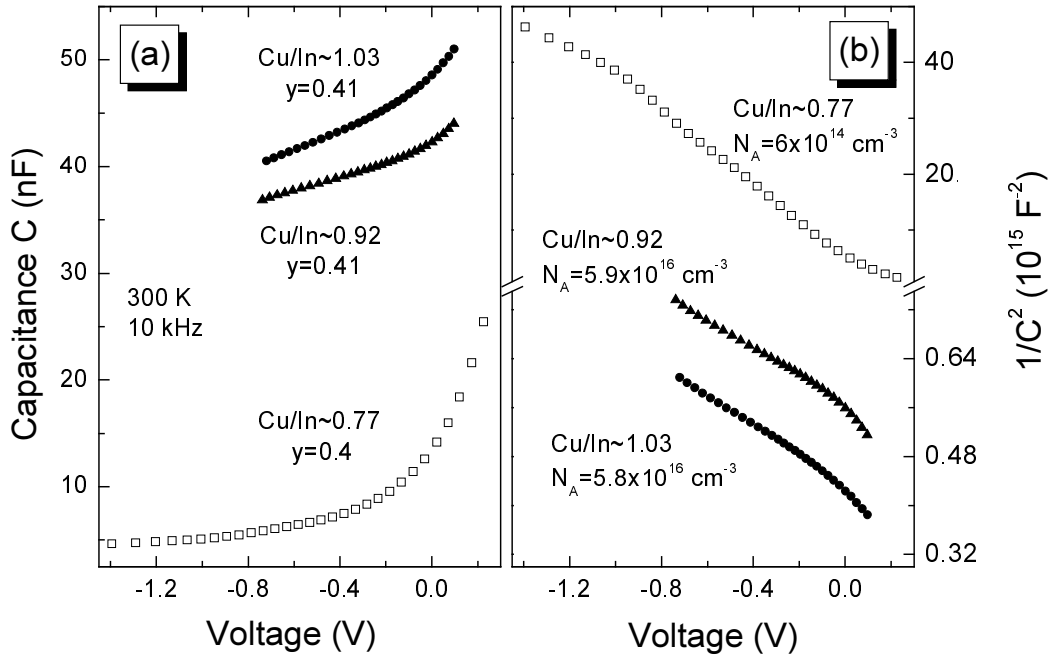
Figure 31. (a) Capacitance-voltage CV characteristics at 300 K and 10 kHz for devices based on CuIn(Se$_{1-y}$S$_y$)$_2$ absorbers with Cu/In ratios of 0.77 (open squares, y = 0.4), 0.92 (full triangles, y = 0.41), and 1.03 (full circles, y = 0.41). (b) Plots of 1/C^2 vs. V for the devices in (a) showing that the doping density extracted from the slope [257] increases with increasing Cu/In ratio. Device area is 0.5 cm^2.
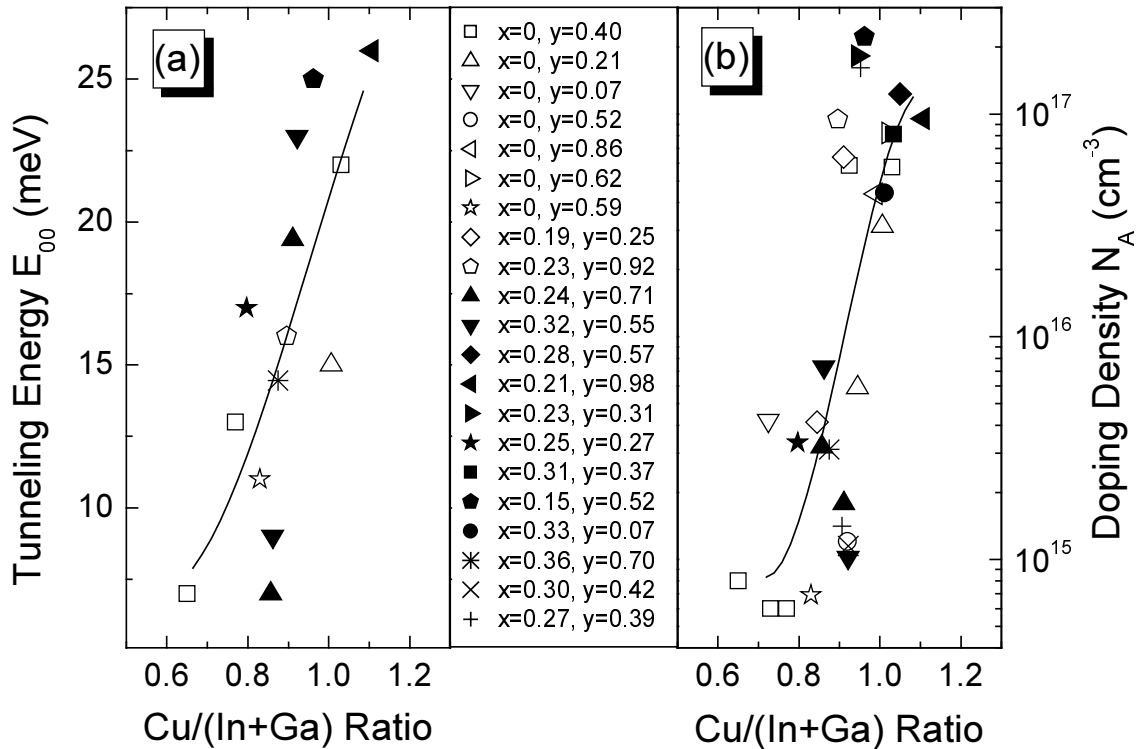

Figure 32. (a) Tunneling energy E$_{00}$ from current-voltage analysis and (b) doping density N$_A$ from capacitance-voltage analysis at 300 K and 10 kHz [257] as a function of Cu/(In+Ga) ratio for Cu(In$_{1-x}$Ga$_x$)(Se$_{1-y}$S$_y$)$_2$ heterojunctions with different x and y ratios [iv]. Both N$_A$ and E$_{00}$ display a strong increase at the Cu-poor/Cu-rich stoichiometry boundary.

The doping densities N_A obtained from the capacitance-voltage analysis [257] of $Cu(In_{1-x}Ga_x)(Se_{1-y}S_y)_2$ heterojunctions with various x and y ratios are summarized in Figure 32 together with the corresponding tunneling energies E_{00} extracted from current-voltage measurements. As mentioned in the preceding section, the tunneling energies E_{00} are obtained by fitting the temperature-dependence of the ideality factors to eq. (23) and to eq. (25) for the Cu-rich and for the Cu-poor devices, respectively. The fits also yield characteristic energies $E^* = k_B T^*$ between 54 meV and 680 meV (for the Cu-poor devices) and parameters α_0 between 0.17 and 0.74 (for Cu-rich devices) [iv]. Both N_A and E_{00} are plotted in Figure 32 versus Cu/(In+Ga) ratio which appears to be now the relevant compositional parameter. The data in Figure 32 (b) indicate that, irrespective of the x and y ratios, the doping density shows a sharp increase (more than two orders of magnitude) at the Cu-poor/Cu-rich stoichiometry boundary. The tunneling energy in (a) displays the same trend for the devices under consideration, as expected since the two quantities are related according to eq. (24).

7.3. Discussion

The results of the preceding sections show that the dominant recombination mechanism, including the tunneling contribution, is not directly controlled by Ga/In or S/Se alloying, but rather is driven by changes in the Cu-stoichiometry. As summarized in Figure 29, the electronic loss in Cu-poor devices is dominated by bulk recombination, whereas the main recombination path in Cu-rich heterojunctions involves defects at the CdS/absorber interface. Thus, the borderline between bulk and interface recombination in the investigated devices appears to follow the stoichiometry border between Cu-rich and Cu-poor alloys.

7.3.1. Band alignments at the CdS/absorber interface

Figure 33 displays the position of the energy bands at the CdS/absorber interface for (a) $CuInS_2$, (b) $CuInSe_2$, and (c) $CuGaSe_2$ heterojunctions, as inferred from the present results. The slight lowering of the interface position of the Fermi level E_F^{if} on the energy scale when turning from $CuInSe_2$ to $CuInS_2$, and the upward shift of E_F^{if} upon alloying $CuInSe_2$ with Ga are also suggested. Figure 33 sets the band diagrams on a common energy scale using the band offsets between bulk $CuInSe_2$, $CuInS_2$, and $CuGaSe_2$ absorbers, as found
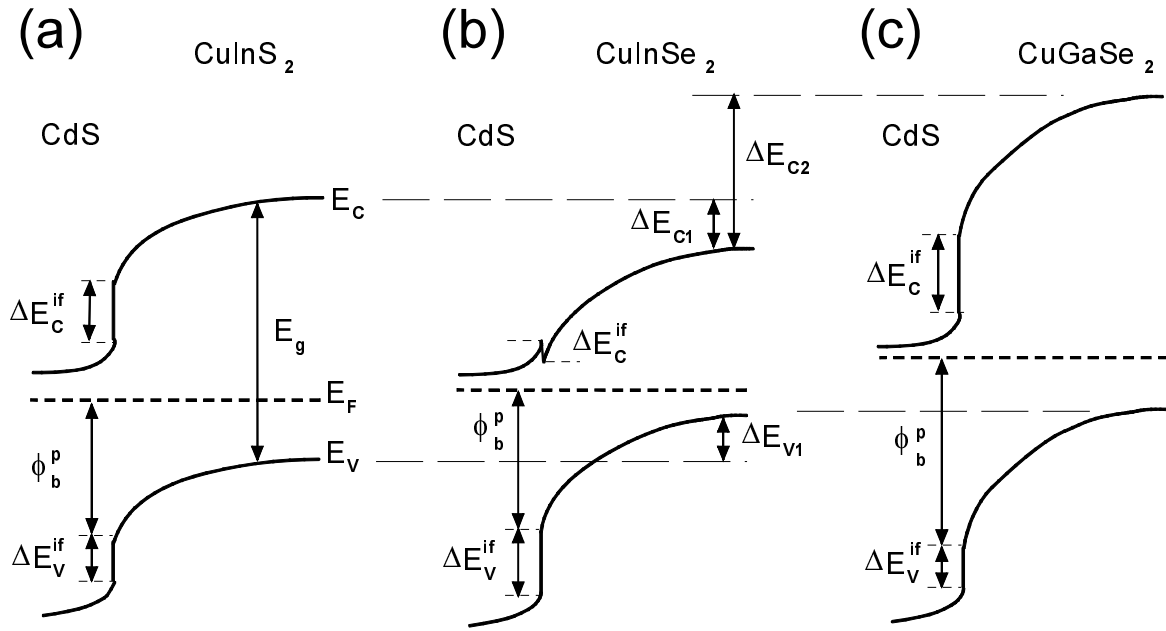
Figure 33. Relative position of the valence and conduction band edge E_V and E_C, and that of the Fermi energy E_F for (a) CuInS₂, (b) CuInSe₂, and (c) CuGaSe₂ heterojunctions. The interface recombination barrier ϕ_b^p, the valence and conduction band offsets ΔE_V^{if}, ΔE_C^{if} at the CdS/absorber interface, and the band offsets $\Delta E_{V1} = \Delta E_V(CuInSe_2/CuInS_2)$, $\Delta E_{C1} = \Delta E_C(CuInSe_2/CuInS_2)$, and $\Delta E_{C2} = \Delta E_C(CuInSe_2/CuGaSe_2)$ between bulk chalcopyrites ($\Delta E_V(CuInSe_2/CuGaSe_2) \approx 0$ is considered) are qualitatively indicated.

in Chapter 6 for Cu-poor compositions. The lowering of the Fermi energy E_F^{if} at the heterointerface under S alloying (deduced from the constancy of the interface barrier ϕ_b^p in Cu-rich devices) is to some extent in disagreement with the finding of an unchanged E_F^{if} (found in Chapter 6 from the energy of the interface donor N_1). A plausible explanation involves the difference in the Cu content of the samples since, as argued in Ref. [91], the pinning position of the Fermi energy at the absorber surface is substantially higher for Cu-poor films than for the Cu-rich counterparts. Nevertheless, a strong tendency of an upward shift of the interface Fermi energy position together with the conduction band upon alloying CuInSe₂ with Ga is consistently found in this Chapter and in Chapter 6, while this tendency is absent or even negative under alloying with S.

7.3.2. The effect of the surface layer

As already mentioned in Section 3.2.2, the discontinuity ΔE_C^{if} at the CdS/chalcopyrite interface is close to zero in case of the standard low-gap Cu(In₁₋ₓGaₓ)Se₂ but can become large in the case of wide-gap chalcopyrites [34,70]. The band alignments are in this case unfavorable for the electrical transport because the interface barrier ϕ_b^p between the Fermi

energy and the valence band edge of the absorber at the CdS/absorber interface is relatively small and electrons from the CdS can (cross)-recombine with holes from the absorber. Therefore, a high interface recombination current is considered as an important drawback of wide-gap chalcopyrite solar cells [34].

At this point, it is useful to consider the two different ways to grow a chalcopyrite thin film in terms of Cu-poor and Cu-rich deviations from stoichiometry. High-efficiency devices based on low-gap Cu(In,Ga)Se$_2$ absorbers [7] use an overall Cu-poor composition of the final film. High-gap materials, especially CuInS$_2$ [36], are grown with a final Cu-rich composition, where the excess CuS has to be removed by a KCN etch from the film before further device processing [166]. After this etching step the remaining film has a rather stoichiometric composition. For CuGaSe$_2$ both, the Cu-poor and the Cu-rich growth methods are used [255]. In all Cu-poor Cu(In$_{1-x}$Ga$_x$)Se$_2$ - based solar cells the limiting factor for the open circuit voltage V_{OC} is recombination in the bulk of the absorber material [29], while Cu(In,Ga)S$_2$ [38,258] and those CuGaSe$_2$ devices where the films are prepared under Cu-rich conditions [255] are dominated by interface recombination. Therefore, as the present results also show, it may well be possible that the borderline between bulk and interface recombination is a matter of Cu-poor and Cu-rich preparation rather than a result of the difference between small-gap and wide-gap materials as argued earlier [34].
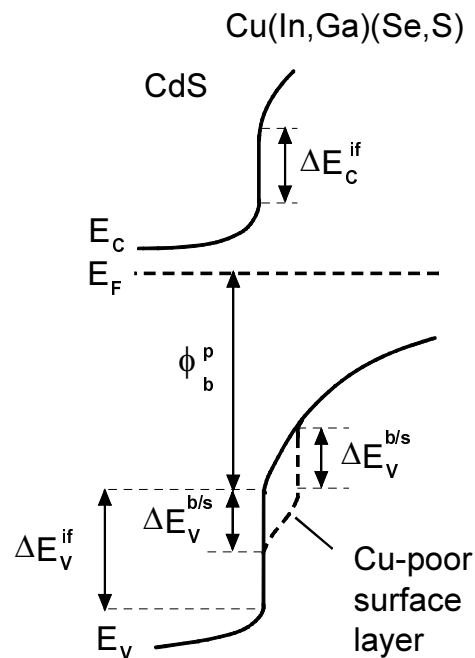

Figure 34. Band alignments at the CdS/Cu(In,Ga)(Se,S)$_2$ interface with an especial focus on the uppermost surface region of the Cu-poor absorber. A layer with a Cu-poorer composition and a larger band gap than the bulk of the absorber develops naturally on the top of such a film [201]. As a result the band gap of the absorber is enlarged towards the heterointerface and the barrier ϕ_b^p for interface recombination is increased.

The fact is, however, hard to explain for wide-gap chalcopyrites, as $\phi_b^p = E_g - \Delta E_C$ is much smaller than E_g for large ΔE_C and the interface recombination should prevail under these circumstances. The fundamentally different recombination behavior of Cu-poor chalcopyrite devices compared to their Cu-rich grown counterparts can be explained when taking into account the (still controversial) surface layer with a higher band gap energy than that of the bulk material [200-202]. As discussed in Section 3.2.3 and sketched in Figure 34, in the very surface region of those films a layer with a Cu-poorer composition and a larger band gap with respect to the bulk material develops naturally [201]. This band gap widening towards the surface is accommodated by a bulk/surface valence band offset $\Delta E_V^{b/s}$, which is around 0.4 eV in case of CuInSe$_2$ [70,201]. Figure 34 shows that such a band offset directly increases the barrier ϕ_b^p to a value $\phi_b^p + \Delta E_V^{b/s}$ which is now sufficiently large to eliminate interface recombination [38,259,260], and the recombination in the bulk is likely to be dominant under these circumstances.

7.4. Conclusion

Current-voltage[i] and capacitance-voltage analyses have revealed a close inter-dependence between absorber composition and charge carrier recombination in Cu(In,Ga)(Se,S)$_2$ heterojunction solar cells. The dominant recombination mechanism, including the tunneling contribution, is driven by changes in the Cu-stoichiometry. Whereas Cu-rich heterojunctions are dominated by recombination at the CdS/absorber interface, bulk recombination prevails in Cu-poor devices irrespective of the band gap energy of the absorber. The results indicate that the enlargement of the band gap energy towards the film surface is an important and operative element which reduces the interface recombination in Cu-poor Cu(In,Ga)(Se,S)$_2$ heterojunctions.

---

[i] When performing temperature-dependent current-voltage analysis in this work, the current is measured in Amperes (A) (cell area is 0.5 cm^2) and not in mAcm^{-2}, as initially considered (see also the related data in Ref. [283(c),(d),(e)] and explicitly the vertical axis of Figure 2(b) in Ref. [283(c)] where the units of j_0 are Amperes and not mAcm^{-2}). The units of j_0 in Figure 27(a),(b), Figure 28(b), Figure 30(a), and Figure 40 in this work have been corrected.

[ii] The samples mentioned in Ref. [207] include absorbers with compositional gradient in the depth. The compositional depth gradient of the absorber may be important especially with respect to Figure

29 where the activation energy of the recombination is plotted versus the band gap energy of the absorber. An increasing S content towards the absorber surface will determine the lowering of the valence band edge of the absorber in the surface region. This lowering superimposes in this case on the band gap widening towards the absorber surface due to natural segregation of the surface layer during the growth of Cu-poor absorber. The natural tendency of band gap widening towards the surface in Cu-poor absorbers, a trend inferred from Figure 29, is then enhanced by an increasing S/(S+Se) ratio towards the absorber surface. The analysis of the data in Ref. [207] indicate that such compositional depth gradient of the absorber is present in approximately three samples of the Cu-poor branch (at relatively high absorber band gap energies) and in at least one sample of the Cu-rich branch (with $x \approx 0.25$) of Figure 29. The same observations advert to Figure 3 of Ref. [283(c)], to Figure 3 of Ref. [283(d)], and to Figure 3 of Ref. [283(e)].

[iii] The analysis of the data in Ref. [207] indicate that approximately three absorbers of the Cu-rich branch (with $x \approx 0.25$) of Figure 29 may have not been etched prior to device processing (see also the corresponding Figure in Ref. [283(c),(d),(e)] as above).

[iv] The values of the doping densities used in Figure 31(b) and more important in Figure 32(b) are provided by O. Pakma according to Ref. [257]. When fitting the temperature dependence of the ideality factor for Figure 32(a), a set of data points including, with few exceptions, those cases where the fits were considered qualitatively unsatisfactorily was removed from the respective figure. As mentioned in Section 7.2.3, the temperature dependence of the ideality factor for the Cu-rich devices was analysed using eq. (23). The quantity α_0 was not considered fixed, but rather was assumed as free fitting parameter together with E_{00}. It can be considered that the values of α_0 (between 0.17 and 0.74, as mentioned in Section 7.2.3) obtained from fits are extremely small, however, the respective E_{00} values are used in Figure 32(a). For the sample illustrated in Figure 40 corresponding to the data point the with $E_{00} = 16$ meV ($\alpha_0 = 0.171$) and Cu/(In+Ga) ratio of 0.896 (considered Cu-rich composition) in Figure 32(a), a different evaluation of current-voltage data than shown in Figure 40 was used in Figure 32(a). The use of the evaluation in Figure 40 with eq. (23) gives higher values of E_{00} for this sample. The observations of this paragraph refer also to Figure 4(a),(b) in Ref. [283(d)].

8. Summary and outlook

One way to determine the band lineups within a chemically isovalent system of semiconductors and its alloys is the usage of a reference level which is common to the respective semiconductor materials. While shallow defects are typically hydrogenic and well described by effective mass aproximation, the deeper defect levels induced by extrinsic metal impurities in semiconductors are generally not effective masslike and are not strongly coupled to the band edges [104,111]. Due to this fact, transition metal-induced defects are extensively considered as bulk reference levels, and thus used in the band alignment procedure in heterojunctions [58,104-106]. This work has revealed that deep defect level energies can be used to determine the band alignments within the system of polycrystalline $Cu(In,Ga)(Se,S)_2$ chalcopyrites. Instead of employing extrinsic impurity levels as references, use is made of intrinsic defect energies which are commonly observed in this system [30,234]. A close interdependence between absorber composition and charge carrier recombination in $Cu(In,Ga)(Se,S)_2$ solar cells is also revealed.

The energetic depths of the dominant defect distributions in Cu-poor chalcopyrites involving donors at the CdS/absorber interface and acceptors in the chalcopyrite bulk, increase upon alloying $CuInSe_2$ with S. The use of the bulk acceptor as reference shows that the band gap difference ΔE_g is shared between comparable valence and conduction band offsets $(\Delta E_V \approx \Delta E_C \approx \Delta E_g/2)$ for the combination $CuInSe_2/CuInS_2$, and is almost exclusively accommodated in the conduction band offset $(0 \approx \Delta E_V \ll \Delta E_C \approx \Delta E_g)$ for the sequence $CuInSe_2/CuGaSe_2$. The Fermi energy position at the CdS/chalcopyrite interface shifts upwards closely following the conduction band upon increasing Ga content and remains essentially unchanged under anion S/Se alloying.

In contrast to the band discontinuities, the dominant recombination mechanism, including the tunneling contribution, is not directly controlled by S/Se or Ga/In alloying, but rather is driven by changes in the Cu-stoichiometry. The recombination barrier follows the band gap energy of the absorber irrespective of alloy composition in Cu-poor devices, indicating a dominant bulk recombination. In turn, interface recombination prevails in Cu-rich devices displaying substantially smaller barriers which are largely independent from the S/Se ratio and increase under Ga addition. The borderline between bulk and interface

recombination in the Cu(In,Ga)(Se,S)$_2$ heterojunctions under investigations appears to follow the stoichiometry border between Cu-poor and Cu-rich absorber compositions.

The band offsets, defect densities, and carrier recombination appear to be significant issues when using the full Cu(In,Ga)(Se,S)$_2$ alloy system as absorber material for high open circuit voltage solar cells. Although with a lesser photovoltaic performance than the low-gap absorbers, pentenary alloys seem to overcome the disadvantages of CuGaSe$_2$ which displays a high doping density enhancing the tunneling recombination and of Cu-poor CuInS$_2$ which shows an extremely low conductivity [3]. It seems that the overall positive features present in high-quality low-gap Cu(In,Ga)Se$_2$ material can be preserved at larger band gap energies if one uses the full chalcopyrite alloy system [3].

The band alignments are especially important when speaking about *graded-gap structures* based on pentenary Cu(In,Ga)(Se,S)$_2$ alloys [3]. An increasing Ga/(Ga+In) ratio towards the absorber/Mo interface leads to a gradual rise of the conduction band edge energy and the resulting back surface field drives away the photogenerated electrons from the absorber/Mo interface minimizing the back contact recombination [3] (for studies of Ga grading in Cu(In,Ga)Se$_2$ solar cells see e.g., Refs. [259,261]). On the other hand, under an increasing S/(S+Se) ratio towards the front heterointerface, part of the increasing band gap is accommodated in the lowering of the valence band edge energy, and the recombination at the buffer/absorber interface is minimized [3]. The results of Chapter 6 allow one to estimate in some cases the energy band gradients when the compositional depth profiles are known.

The deep level approach can be further applied to other compositional sections within the chalcopyrite alloy system. Figure 35 uses the intrinsic acceptor $E_T(N_2)$ from Chapter 6 and the extrinsic Co^{2+} deep acceptor from Refs. [120,262] to set the energy bands of CuIn(Se,S)$_2$, Cu(In,Ga)Se$_2$, and Cu(Ga,Al)Se$_2$ alloy systems on the same energy scale. The band offsets between CuGaSe$_2$ and CuAlSe$_2$ ($\Delta E_V = 0.64$ eV and $\Delta E_C = 0.35$ eV) conflict to the results of first-principle calculations ($\Delta E_V = 0.22$ eV and $\Delta E_C = 0.77$ eV in Ref. [240]), but agree to some extent with experimental values ($\Delta E_V = 0.7$ eV, $\Delta E_C = 0.3$ eV in Ref. [74], and $\Delta E_V = 0.8$ eV, $\Delta E_C = 0.2$ eV in Ref. [125]). Figure 35 also displays the deep defect level of Fe in CuInSe$_2$ [263], CuInS$_2$ [264], CuGaSe$_2$ [265], and CuAlSe$_2$ [266], which seems to have a constant energy position on the absolute energy scale. In addition, a deep defect level recently identified [267] in Cu(In,Ga)Se$_2$ alloys aligns at a constant energy distance of 0.8 eV from the valence band edge independently of the Ga content.

The trends of extrinsic dopability within the chalcopyrite system - closely related to those of band alignments - are systematized by Zhang et al. [107] in terms of *doping pinning*
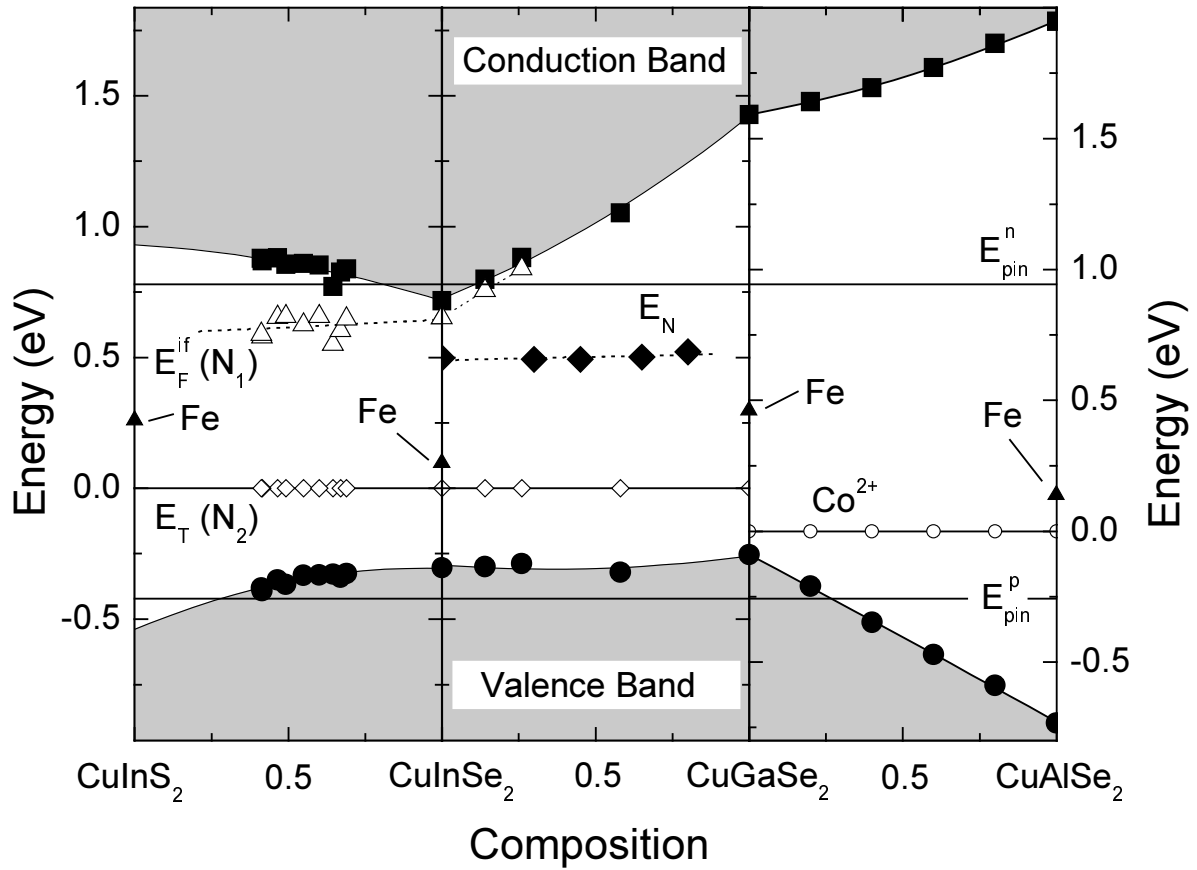
Figure 35. The alignment of the valence band edge E_V (full circles) and conduction band edge E_C (full squares) for the polycrystalline alloy systems CuIn(Se,S)$_2$, Cu(In,Ga)Se$_2$ (performed in Chapter 6 of this work with respect to the intrinsic acceptor level $E_T(N_2)$ (open diamonds)), and for the single crystals of Cu(Ga,Al)Se$_2$ (performed in Refs. [120,262] with respect to the extrinsic Co^{2+} acceptor level (open circles)). An energy distance of about 161 meV is found between the defect levels used as reference for the band alignment. The energy positions E_{Fe} of the Fe acceptor level (full triangles) in CuInSe$_2$ single crystals ($E_{Fe} - E_V = 0.4$ eV) [263], CuInS$_2$ single crystals ($E_{Fe} - E_V = 0.8$ eV) [264], CuGaSe$_2$ ($E_{Fe} - E_V = 0.55$ eV) [265], and CuAlSe$_2$ ($E_{Fe} - E_V = 0.87$ eV) [266], as well as the energy position E_N (full diamonds) of a deep defect level determined in devices based on polycrystalline Cu(In,Ga)Se$_2$ alloys [267] are also displayed. Solid horizontal lines show the composition-independent doping pinning levels E_{pin}^n and E_{pin}^p according to first principle calculations [107]. Open triangles denote the Fermi level position at the CdS/absorber interface as determined in Chapter 6. Figure 35 corresponds to Figure 2 in Ref. [283(d)]. The energetic depths of the Fe defect level with respect to the valence band edge plotted in Figure 2 in Ref. [283(d)] differ from the respective literature values within the ± 50 meV range, the differences improve the alignment of the energy positions of the Fe defect. In Figure 35 in this work this inconsistency is corrected. Additional inconsistencies related to the positions of the open diamonds on the abscissa axis for the CuIn(Se,S)$_2$ system in Figure 2 in Ref. [283(d)] were also corrected in Figure 35 in this work.

levels E_{pin}^n and E_{pin}^p which set an upper and a lower bound for the variation of Fermi energy

position under doping ($E_{pin}^p \leq E_F \leq E_{pin}^n$). If referred to an absolute reference (e.g., vacuum

level), the doping pinning levels are independent of the host material within a certain

semiconductor system (similarly to transition metal impurity levels, see Section 2.10) [107,268]. A specific composition for which $E_{pin}^{n} \ll E_{C}$ ($E_{pin}^{p} \gg E_{V}$) cannot be doped n-type (p-type) [107,268]. In addition to the experimental defect data, Figure 35 shows the energy position of E_{pin}^{n} and E_{pin}^{p} for chalcopyrites, according to first principle calculations [107]. While CuInSe$_2$ can be doped both p- and n-type, Cu(In,Ga)Se$_2$ alloys with a high Ga content can no longer be doped n-type [107] and the maximum dopability range is further reduced for CuAlSe$_2$.

A more detailed analysis could investigate the correlation between the barrier heights of Schottky structures based on chalcopyrite alloys and the band alignments derived from chalcopyrite heterojunctions in this work (characterizations of Schottky junctions involving chalcopyrite materials are found e.g., in Refs. [269-276]). A further analysis may also involve the comparison of the experimental reference level used in the present work for band alignments and the calculated charge neutrality level (or other equivalent reference) within the chalcopyrite alloy system (estimations of reference levels for ternary chalcopyrite compositions may be found e.g., in Ref. [91]). Further work on band alignments within the I-III-VI$_2$ alloy system may be an important ingredient in optimization of chalcopyrite heterojunction solar cells.

Appendices

A.   Defects and device performance

The electrical behavior and the performances of chalcopyrite thin film solar cells are influenced mainly by defect levels in the bulk of the space charge region and at the interface of the heterojunction [3,277]. The characterization of these levels is a necessary step for further improvement of the solar cells as well as for fundamental understanding of unusual defect physics of this class of compounds with respect to their binary analogs [171]. The performance of the $Cu(In_{1-x}Ga_x)(Se_{1-y}S_y)_2$ solar cells - in terms of open circuit voltage V_{OC}, short circuit current density j_{SC}, fill factor FF, and conversion efficiency η - depends strongly on the absorber composition. A moderate Ga addition (up to roughly $x \approx 0.3$) to $CuInSe_2$ has a beneficial effect upon the device performance, while higher Ga contents lead to a sharp decrease in efficiency [30,31]. The amount of Ga added to the alloy not only influences the band gap energy but also the defect distribution in the absorber material and the transport mechanism [29,255]. An increasing Ga content enhances the contribution of tunneling to recombination [29]. By increasing the donor formation energies, Ga favors the formation of acceptors [176,278]. Similar considerations hold for alloying $CuInSe_2$ with S [183].

Figure 36 displays the dependence of the standard photovoltaic parameters of the two series of $Cu(In_{1-x}Ga_x)(Se_{1-y}S_y)_2$ devices with (a) $x = 0$ and (b) $x \approx 0.3$ investigated in Chapter 6 as a function of the sulphur content into the absorber. By enlarging the band gap of the absorber under an increasing sulphur content, the open circuit voltage increases and the short circuit current decreases, this behavior being accompanied by a reduction in the conversion efficiency. Small contents of sulphur possibly have beneficial effects upon device performance, as the efficiency data tend to show maxima around $y \approx 0.2$ for both series (a) and (b) in Figure 36.

Besides the composition dependence, the open circuit voltage of the device is closely related to the concentration of the bulk acceptor N_2 [29,30], as mentioned in Section 6.1. The values of the acceptor concentrations N_T are also included in Figure 36 for both series (a) and (b) of $Cu(In_{1-x}Ga_x)(Se_{1-y}S_y)_2$ devices. The defect concentration is obtained by integration of the acceptor-related maxima over energy (see Figure 18 in Chapter 6). Apparently, the

conversion efficiency and the defect concentration are statistically anti-correlated over the whole investigated compositional range for both series of devices.
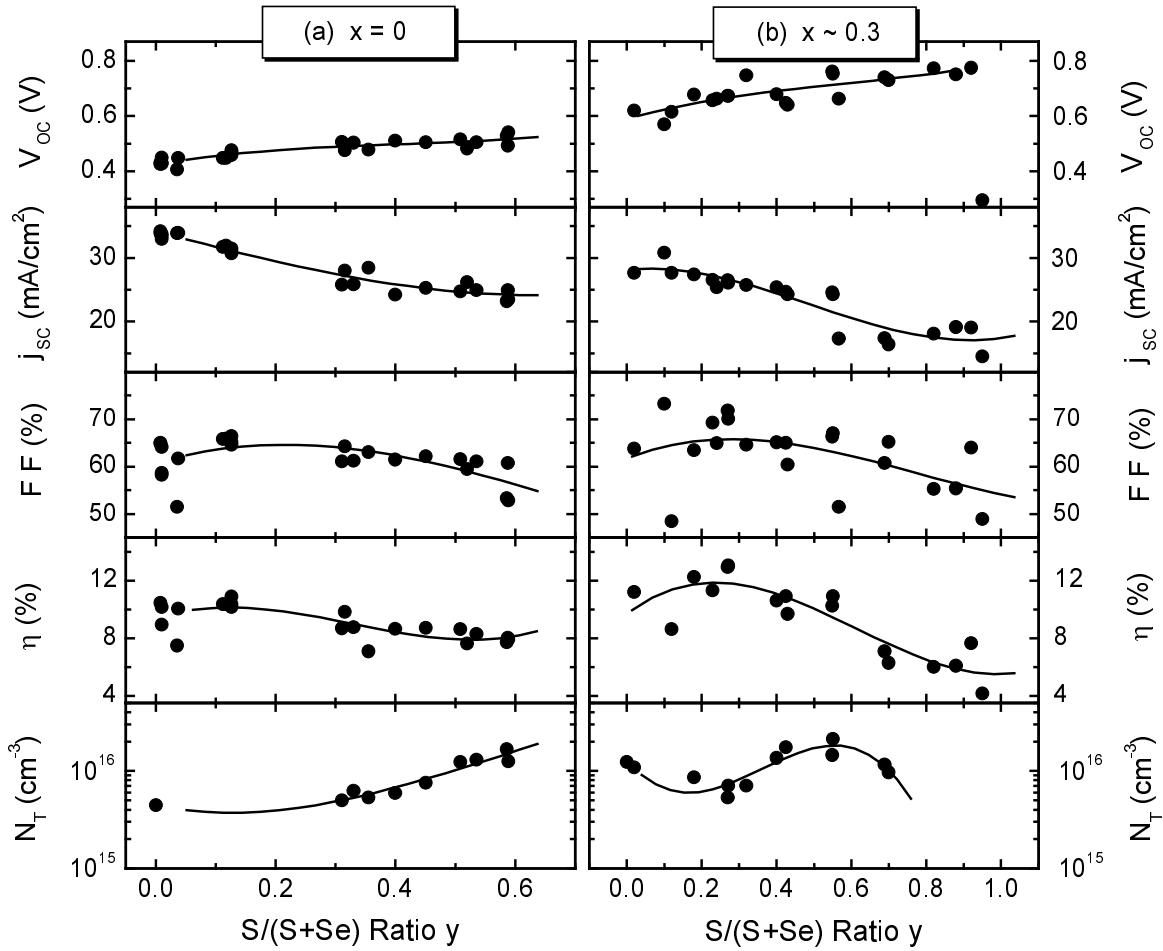

Figure 36. Device parameters open circuit voltage V_{OC}, short circuit current density j_{SC}, fill factor FF, and efficiency η measured under standard illumination conditions as a function of the S/(S+Se) ratio y for the two series of $Cu(In_{1-x}Ga_x)(Se_{1-y}S_y)_2$ heterojunction solar cells with (a) x = 0 and (b) x ≈ 0.3 investigated in Chapter 6. The efficiency data denote active area values corrected using quantum efficiency measurements. Also shown is the composition dependence of the defect concentration N_T of the bulk acceptor N_2, as extracted from the corresponding defect density spectra. Data from Refs. [207,236] are included.

For more insight, the open circuit voltage loss $E_g/q - V_{OC}$ should be considered as a convenient measure to compare V_{OC} of solar cells with different absorber band gap energies. If the open circuit voltage of the devices is limited by recombination in the space charge region of the absorber, the following dependence holds

$$E_g - qV_{OC} = n_{id}\, k_B T\, \ln\left(\frac{j_{00}}{j_{SC}}\right) \propto n_{id} \ln N_T \ , \qquad (28)$$

with the notations in Chapter 7, where the prefactor j_{00} is considered to be proportional to the concentration N_T of recombination centers N_2 [29,30]. Similarly to the case of Ga/In alloying

in chalcopyrites [30], lower efficiencies for high sulphur content in the absorber are a consequence of the fact that the open circuit voltage V_{OC} of the $Cu(In_{1-x}Ga_x)(Se_{1-y}S_y)_2$ - based devices does not increase proportionally to the increase of the band gap energy [34]. This is seen in Figure 37(a) which displays the dependence of the open circuit voltage V_{OC} on the band gap energy E_g for the series (a) of $CuIn(Se_{1-y}S_y)_2$ - based heterojunctions with different S/(S+Se) ratios in Figure 36. The same trend is found for the series of Ga-containing devices.
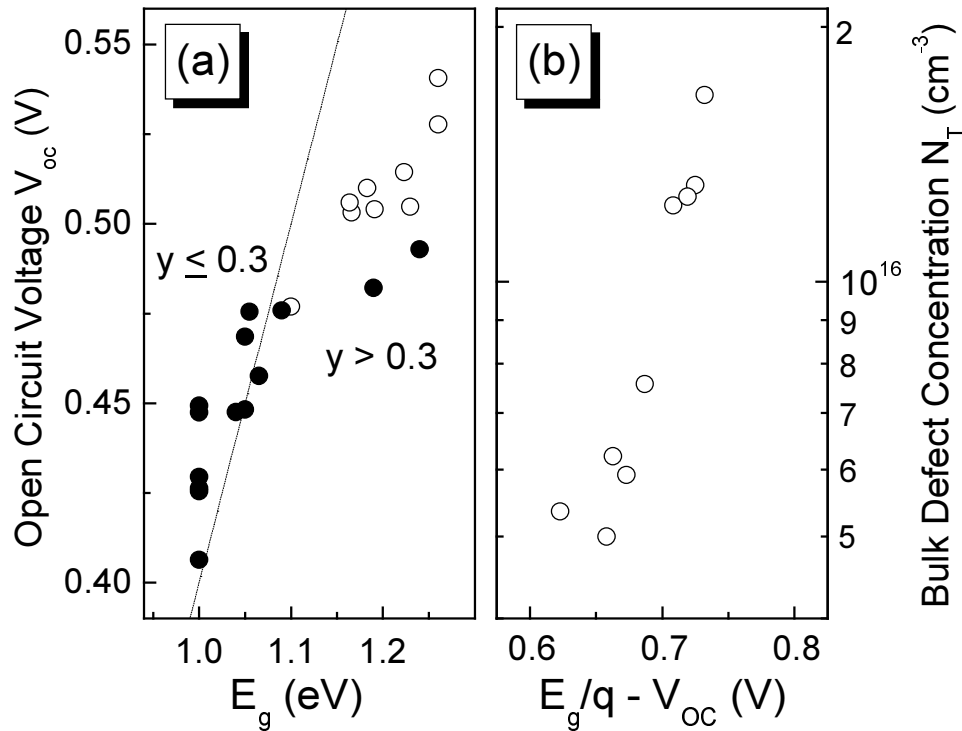

Figure 37. (a) Open circuit voltage V_{OC} vs. the band gap energy E_g of the absorber for the series (a) of $CuIn(Se_{1-y}S_y)_2$ - based devices in Figure 36. V_{OC} increases as the fraction y of incorporated sulphur in the absorber becomes larger. The dotted line shows the linear relationship $V_{OC} = E_g/q - 0.6$ V. (b) The reorganization of the data points represented by open circles in Figure 37(a) with the concentrations N_T of the bulk defect N_2 plotted vs. the open circuit voltage loss $E_g/q - V_{OC}$. Figure 37 corresponds to Figure 10 in Ref. [283(b)]. When considering Figure 10 in Ref. [283(b)], the sample corresponding to the data point with $V_{OC} = 0.47697$ V and $E_g = 1.1$ eV in Figure 10(a), although it is not enclosed by the indicating oval, is considered in Figure 10(b) (where $N_T = 5.35 \times 10^{15}$ cm^{-3} and $E_g/q - V_{OC} = 0.62303$ V for this sample). The sample in Figure 10(a) in Ref. [283(b)] corresponding to the data point with $V_{OC} = 0.49293$ V and $E_g = 1.24$ eV is not considered in Figure 10(b). For a more clear visualization, different symbols are used in Figure 37 in this work to denote the reorganized data.

For low y ratios ($y \lesssim 0.3$), V_{OC} increases slightly superlinear with E_g, whereas a sublinear increase is seen for higher sulphur fractions. The admittance spectra of Chapter 6 indicate that the electronic quality of the material deteriorates at high contents of incorporated sulphur (as reported in Refs. [29,30], the electronic quality of the material also deteriorates at high Ga

content). Figure 37(b) reorganizes the data represented by open circles in Figure 37(a), using the same method that was used for Ga/In alloys [29,30]. Here, the concentration N_T of the bulk defects N$_2$ is plotted versus the open circuit voltage loss $E_g/q - V_{OC}$. The correlation shows that the open circuit voltage losses result from high bulk defect concentrations in the absorber material, similarly to the case of In/Ga alloying [29,30]. However, a small S content in the absorber may maintain a linear dependence of V_{OC} on the band gap, decreasing the number of electronically active recombination centers [183].

B. Determination of band gap energies of Cu-chalcopyrite alloys

The band gap energies of Cu(In$_{1-x}$Ga$_x$)(Se$_{1-y}$S$_y$)$_2$ chalcopyrite alloys are determined throughout this work by external quantum efficiency (EQE) measurements on ZnO/CdS/chalcopyrite devices. The external quantum efficiency provides information on the photon absorption and carrier collection properties of the solar cell, and is defined as the ratio between the number of collected charge carriers and the number of photons of wavelength λ incident on the solar cell [279].
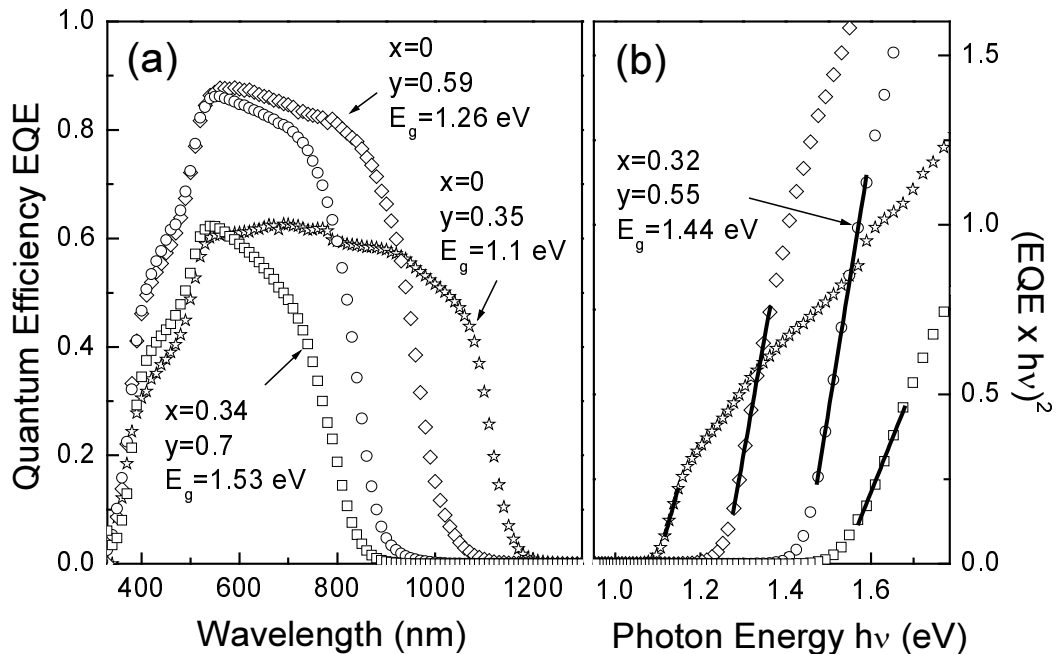

Figure 38. (a) External quantum efficiency EQE spectra plotted versus the wavelength of the incident light for ZnO/CdS/Cu(In$_{1-x}$Ga$_x$)(Se$_{1-y}$S$_y$)$_2$ heterostructures with different absorber compositions. (b) Determination of the band gap energy E_g of the absorber for the heterostructures in (a) from plots of (EQE·hv)^2 versus hv, where hv is the photon energy [280]; stars: x = 0, y = 0.35, E_g = 1.1 eV; diamonds: x = 0, y = 0.59, E_g = 1.26 eV; circles: x = 0.32, y = 0.55, E_g = 1.44 eV; squares: x = 0.34, y = 0.7, E_g = 1.53 eV.

The external quantum efficiency measurements are performed at room-temperature using the experimental setup described in Section 4.4. Figure 38(a) displays external quantum efficiency spectra of ZnO/CdS/Cu(In$_{1-x}$Ga$_x$)(Se$_{1-y}$S$_y$)$_2$ heterojunctions based on absorbers within the two series of alloys with $x = 0$ and $x \approx 0.3$ used for the band alignments in Chapter 6. At short wavelengths the EQE spectra are dominated by the CdS buffer layer, while in the long-wavelength range (at energies under the band gap energy of CdS) the photogeneration takes place mainly in the absorber [281]. The long-wavelength edge of the EQE spectra is related to the band gap energy E_g of the absorber. Assuming that the EQE signal is proportional to the absorption coefficient of the absorber in the wavelength range used for the determination of E_g, the absorber band gap energy can be determined from plots of $(EQE \cdot h\nu)^2$ vs. $h\nu$, where $h\nu$ is the photon energy, as performed e.g., in Ref. [282] for junctions based on CuIn$_3$Se$_5$ material. Figure 38(b) illustrates the determination of band gap energy of the absorber for the heterojunctions in Figure 38(a).

C.   Determination of absorber composition

This appendix and the next two sections give supplementary information upon the steps followed when analyzing the experimental data. The approximations and the related uncertainties of the results are also presented. The following observations refer also to Ref. [283] where results of the present work have been previously published. Where considered necessary, corrections were performed to certain figures in this work with respect to the corresponding initial figures in Ref. [283].

As mentioned in Section 4.2, the absorber composition in this work and in Ref. [283] is determined by energy dispersive X-ray (EDX) measurements. The absorber composition at a certain region on the preparation stripes is generally obtained by using an average value of the EDX measured compositions which are available at points situated in the vicinity of the investigated region. This averaging procedure introduces additional errors at the determination of absorber composition, besides the uncertainty of the measurement technique.

Superimposed signals corresponding to molybdenum and sulphur can be found in the energy dispersive X-ray analysis. For a reduced absorber thickness, it may be assumed that the S/(S+Se) ratio of the absorber grown on Mo coated glass substrate is overestimated by the compositional EDX analysis due to the possible penetration of the electrons from the electron beam down to the Mo film. At the preparation runs of the series (a) of CuIn(Se$_{1-y}$S$_y$)$_2$

absorbers used in Chapter 6 (excepting the reference data for $CuInSe_2$ from Ref. [236]) and in Chapter 7, reference bare glass substrates were used together with the standard Mo coated glass substrates. For thinner $CuIn(Se_{1-y}S_y)_2$ absorbers in the series, the S/(S+Se) compositional ratio y of the absorber was considered with respect to the bare glass substrate, rather than with respect to the Mo coated glass substrate. This adjustment was especially applied in Chapter 6 to the abscissa (S/(S+Se) ratio) values of the data points with $y = 0.31$ and of those with $y = 0.33$ in Figure 19(a), Figure 20(a), and Figure 22(a), and to the abscissa values of data points with y between 0.11 and 0.13 in Figure 19(a). No such adjustments were performed in the case of the series (b) of $Cu(In_{1-x}Ga_x)(Se_{1-y}S_y)_2$ absorber alloys with $x \approx 0.3$ in Chapter 6. Such adjustments of absorber composition were not performed in Chapter 7, despite the samples were generally similar to those of Chapter 6. See also the corresponding Figures in Ref. [283(a),(b),(d)].

D.   Determination of inflexion frequencies in the capacitance spectra

As performed in Chapter 6, the activation energies of defect transitions N_1 and N_2 are determined from Arrhenius plots of $2\pi f_i / T^2$ versus $1/T$ and the inflexion frequencies f_i are determined from the derivative of capacitance spectra. Figure 39 shows the derivative $dC/d\omega$ of the junction capacitance C with respect to the angular frequency ω of the applied signal as a function of the frequency f of the applied signal for two $ZnO/CdS/Cu(In_{1-x}Ga_x)(Se_{1-y}S_y)_2$ heterostructures investigated within the series (a) and (b) in Chapter 6 for the band alignments. The inflexion frequency at each temperature is determined as maximum of the respective graph in Figure 39 and is indicated by vertical dotted lines. The Arrhenius plots of the inflexion frequencies give the respective activation energy of the defect transition N_2 for both samples in Figure 39. For the sample in Figure 39(b), only the indicated temperatures were used for the determination of the activation energies, although maxima of the $dC/d\omega$ vs. f curves are visible at lower and higher temperatures. This selection of temperature range was also performed for the determination of the activation energy of the transition N_1 for the respective sample, as well as for the transitions N_1 or N_2 for other samples (not shown). The noise of the curves in Figure 39(b) was removed by manually smoothing the respective capacitance vs. frequency spectra. This smoothing procedure was performed for at least one additional sample (not shown).
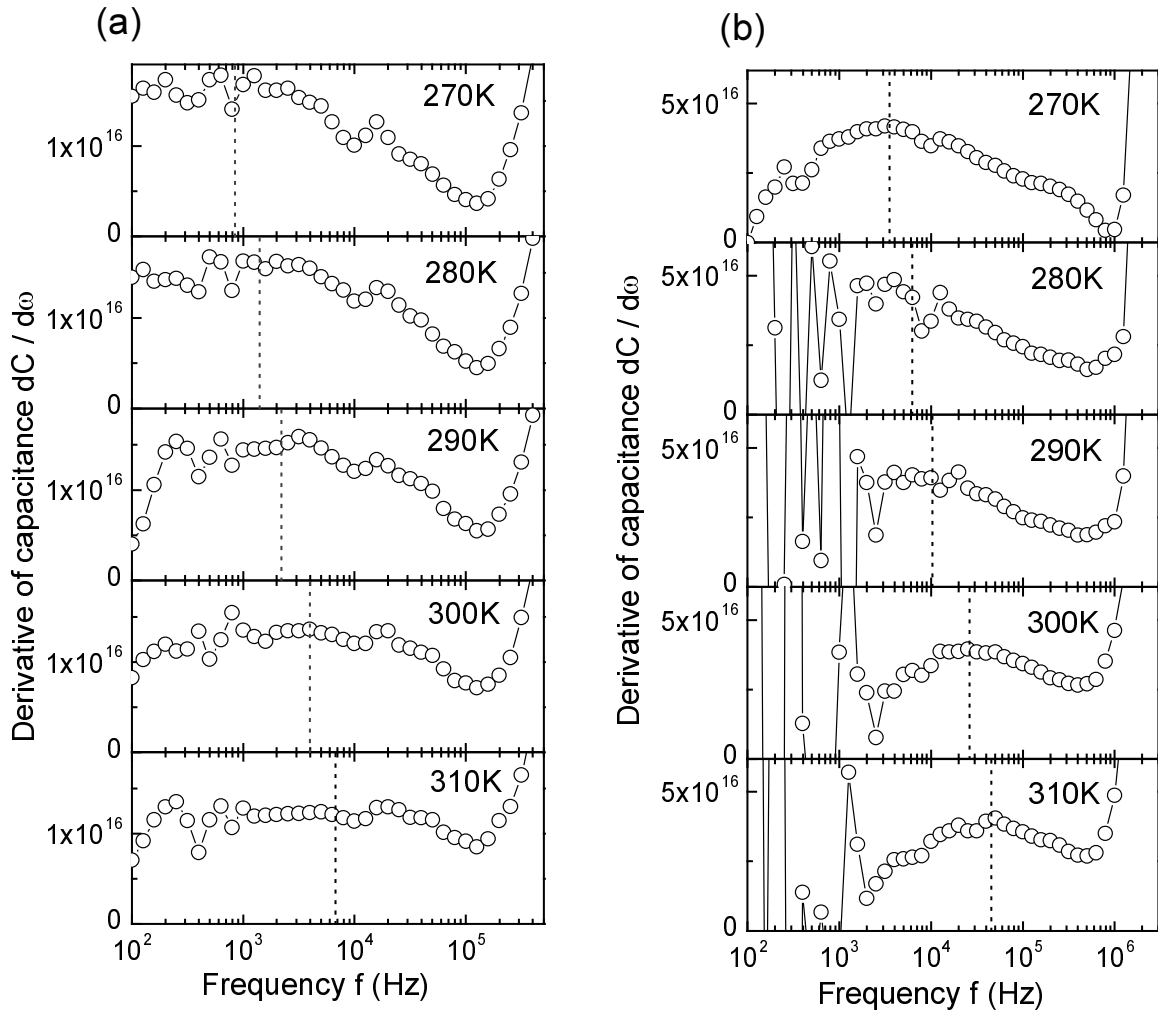
Figure 39. The derivative dC/dω (open circles) of the device capacitance plotted at different temperatures versus the frequency f of the applied signal for (a) a heterojunction based on $CuIn(Se_{1-y}S_y)_2$ absorber with y = 0.31 and (b) a heterojunction based on $Cu(In_{1-x}Ga_x)(Se_{1-y}S_y)_2$ absorber with x = 0.29 and y = 0.43. The vertical dotted lines indicate the chosen maxima in the graphs. The lines connecting the open circles are guides to the eye. The nominal temperature is indicated on the right side for each graph and ω is the angular frequency of the applied signal.

As seen in Figure 39, no fitting procedure was involved for the determination of maxima in the $dC/d\omega$ vs. f curves. This fact determines uncertainties in the values of the defect activation energies and in the related analysis in Chapter 6. An additional estimation of the activation energy of transition N_2 for heterojunctions within the series (a) and (b) investigated in Chapter 6 (see the branches $E_A(N_2)$ in Figure 19(a),(b)) was subsequently performed by fitting the $dC/d\omega$ vs. f curves with Gaussian functions for the determination of inflexion frequencies. For each investigated sample, this latter fitting analysis concentrated exclusively on the capacitance curves at those temperatures which were considered in the initial analysis without fits in Chapter 6. However, from the respective temperature ranges, selected portions of the Arrhenius plots of inflexion frequencies were generally used for

determination of activation energy. By comparing the activation energies obtained as above with the respective values in Chapter 6, an uncertainty of ± 100 meV is estimated for the activation energies of transition N_2 in Figure 19(a),(b). For the sample with $y = 0.689$ in Figure 19(b), strong approximations were made in choosing the inflexion frequencies in the initial analysis, and the error of the respective activation energy value is larger than the uncertainty range given above (data from this sample is also considered in Figure 20(b) which includes the respective activation energy of transitions N_1 and N_2, and in Figure 22(a) which includes the respective full width at half maximum for the defect peaks N_1 and N_2). This sample is excluded from further estimation of the uncertainty in the valence band discontinuities. The valence band offsets in Chapter 6 (see Table IV) are determined by extrapolating the composition dependence of the valence band edge which is directly related in the assumed model to the defect activation energy of transition N_2. An uncertainty of ± 150 meV is estimated for the valence band offsets in Table IV between $CuInSe_2$ and $CuInS_2$ (series (a) in Chapter 6) and between $Cu(In_{0.7}Ga_{0.3})Se_2$ and $Cu(In_{0.7}Ga_{0.3})S_2$ (series (b) with $x \approx 0.3$). For the bowing coefficients of the valence band of the respective alloy systems, the errors appear to be larger. The above fitting analysis predicts even a bowing coefficient with an opposite sign when compared to the respective value in Table IV for the series (b) of $Cu(In_{1-x}Ga_x)(Se_{1-y}S_y)_2$ alloys with $x \approx 0.3$ in Chapter 6. The uncertainties of the values related to the conduction band or to the band gap given in Table IV for series (a) and (b) of alloys in Chapter 6 have not been investigated. The activation energies of transition N_1 in Figure 19(a),(b) were not re-investigated using the fitting analysis. The above observations are mandatory when considering the results of Chapter 6 and the related data in Ref. [283(a),(b),(d)].

E.   Determination of activation energy of recombination

The activation energy E_a of recombination in $Cu(In_{1-x}Ga_x)(Se_{1-y}S_y)_2$-based heterojunctions is determined in Chapter 7 from current-voltage analysis. Figure 40 illustrates the evaluation procedure for the heterojunction with the absorber band gap energy $E_g = 1.64$ eV and the activation energy $E_a = 1.145$ eV in Figure 29. The saturation current and the ideality factor at different temperatures are determined by plotting the short circuit current I_{SC}
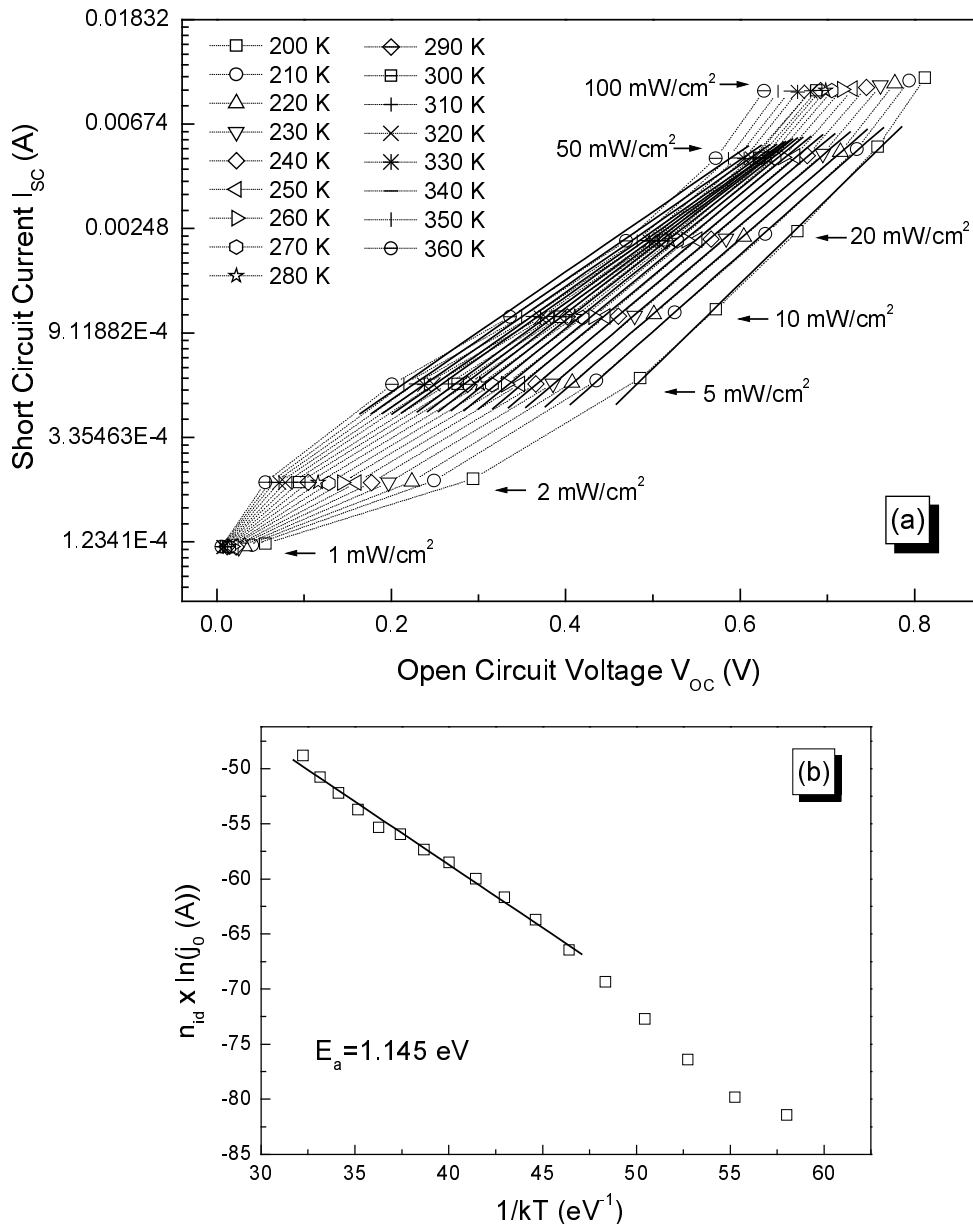
Figure 40. Determination of the activation energy E_a of recombination for the sample with the absorber band gap energy E_g = 1.64 eV and the activation energy E_a =1.145 eV in Figure 29. (a) Plots of short circuit current (natural logarithmic scale) vs. open circuit voltage of the device at different illumination intensities and at different temperatures. The dotted lines which connect the data points are guides to the eye. The solid lines are linear fits to the data points in the indicated range. For each group of data points indicated by arrows, the approximate illumination intensity is also given. (b) Arrhenius plot of corrected saturation current vs. inverse thermal energy as obtained from the linear fits in (a). The linear fit to the data using the indicated selected range gives the activation energy E_a =1.145 eV which is used in Figure 29. The linear fit to the data for the complete Arrhenius plot gives E_a =1.272 eV. Cell area is 0.5 cm^2.

(in natural logarithmic scale) vs. open circuit voltage V_{OC} for different illumination intensities, as shown in Figure 40(a). Only the data points at 50 mW/cm^2, 20 mW/cm^2, 10 mW/cm^2, and 5 mW/cm^2 are chosen in this case for linear fitting at different temperatures. For many other

samples in Figure 29, only three data points at each temperature were used for linear fitting of the respective I_{SC} vs. V_{OC} plots. The activation energy considerably varies depending on the range which is used for linear fitting in the I_{SC} vs. V_{OC} plots, e.g., the activation energy E_a =1.079 eV considered in Figure 29 for the sample with E_g = 1.18 eV is smaller with almost 200 meV if a different range is chosen for linear fitting in the respective I_{SC} vs. V_{OC} plots.

Figure 40(b) shows the determination of the activation energy E_a = 1.145 eV for the sample considered in Figure 40(a) (this activation energy value is used in Figure 29). Only the indicated range was selected for linear fit in Figure 40(b). The linear fit over all points in Figure 40(b) gives E_a = 1.272 eV for this sample. This selection of the range in the Arrhenius plots at the determination of the activation energy was performed for many samples used in Figure 29 in order to make more evident the inferred trends. If the linear fits are applied to the complete Arrhenius plots instead of using the selected regions, the variation of the activation energy values for the other samples in Figure 29 is smaller than the corresponding variation for the sample illustrated above and in Figure 40. The fits applied to the complete Arrhenius plots give generally lower activation energies for the samples on the Cu-poor branch in Figure 29, and a more pronounced scatter of the activation energies for the samples on the Cu-rich branch with $x \approx 0.25$ in the respective figure. For the samples on the Cu-rich branch with $x = 0$ in Figure 29, fits over the complete Arrhenius plots were considered for the determination of activation energies, although curvatures, especially considerably pronounced for the sample with E_g = 1.29 eV and E_a =0.872 eV, may be seen in some Arrhenius plots. The above observations are also important when considering the respective data in Ref. [283(c),(d),(e)], where results from Chapter 7 are also published.

The activation energies of recombination determined in Figure 29 from Arrhenius plots of corrected saturation current can be considerably different when compared to the respective values determined from extrapolation of the open circuit voltage to $T = 0$ K. This observation adverts to the related comments in Chapter 7 and in Ref. [283(c)], and to the corresponding data in Ref. [283(c),(d),(e)].

References

[1] R. L. Anderson, Solid State Electronics **5**, 341 (1962).

[2] U. Rau and H. W. Schock, Appl. Phys. A **69**, 131 (1999).

[3] U. Rau and H. W. Schock, *Cu(In,Ga)Se₂ solar cells*, in *Clean Electricity from Photovoltaics*, edited by M. D. Archer and R. Hill (Imperial College Press, London, UK, 2001), p. 277.

[4] J. L. Shay, S. Wagner, and H. M. Kasper, Appl. Phys. Lett. **27**, 89 (1975).

[5] W. E. Devaney, R. A. Mickelsen, and W. S. Chen, *Proceedings of the 18th IEEE Photovoltaic Specialists Conference* (IEEE, New York, 1985), p. 1733.

[6] K. Mitchell, C. Eberspracher, J. Ermer, and D. Pier, *Proceedings of the 20th IEEE Photovoltaic Specialists Conference* (IEEE, New York, 1988), p. 1384.

[7] M. A. Contreras, B. Egaas, K. Ramanathan, J. Hiltner, A. Swartzlander, F. Hasoon, and R. Noufi, Prog. Photovoltaics: Res. Appl. **7**, 311 (1999).

[8] A. Jasenek and U. Rau, J. Appl. Phys. **90**, 650 (2001).

[9] G. Voorwinden and M. Powalla, Thin Solid Films **387**, 37 (2001).

[10] H. W. Schock and R. Noufi, Prog. Photovoltaics: Res. Appl. **8**, 151 (2000).

[11] M. Powalla and B. Dimmler, Sol. Energy Mater. Sol. Cells **67**, 337 (2001).

[12] B. Dimmler and H. W. Schock, Prog. Photovoltaics: Res. Appl. **4**, 425 (1996).

[13] B. Dimmler and H. W. Schock, Prog. Photovoltaics: Res. Appl. **6**, 193 (1998).

[14] W. H. Bloss, F. Pfisterer, M. Schubert, and T. Walter, Prog. Photovoltaics: Res. Appl. **3**, 3 (1995).

[15] J. R. Tuttle, A. Szalaj, and J. Keane, in *Proceedings of the 28th IEEE Photovoltaic Specialists Conference* (IEEE, New York, 2000), p. 1042.

[16] J. F. Guillemoles, L. Kronik, D. Cahen, U. Rau, A. Jasenek, and H. W. Schock, J. Phys. Chem. B **104**, 4849 (2000).

[17] J. F. Guillemoles, Thin Solid Films **361-362**, 338 (2000).

[18] M. Hartmann, M. Schmidt, A Jasenek, H. W. Schock, F. Kessler, K. Herz, and M. Powalla, in *Proceedings of the 28th IEEE Photovoltaic Specialists Conference* (IEEE, New York, 2000), p. 638.

[19] A. Jasenek, U. Rau, T. Hahn, G. Hanna, M. Schmidt, M. Hartmann, H. W. Schock, J. H. Werner, B. Schattat, S. Kraft, K. H. Schmid, and W. Bolse, Appl. Phys. A **70**, 677 (2000).

[20] U. Rau, A. Jasenek, H. W. Schock, J. H. Werner, G. La Roche, A. Robben, and K. Bogus, in *Proceedings of the 28th IEEE Photovoltaic Specialists Conference* (IEEE, New York, 2000), p. 1032.

[21] D. J. Schroeder, J. L. Hernandez, and A. A. Rockett, Inst. Phys. Conf. Ser. **152**, 749 (1998).

[22] A. Jasenek, H. W. Schock, J. H. Werner, and U. Rau, Appl. Phys. Lett. **79**, 2922 (2001).

[23] V. Probst, F. Karg, J. Rimmasch, W. Riedl, W. Stetter, H. Harms, and O. Eibl, Mat. Res. Soc. Symp. Proc. **426**, 165 (1996).

[24] I. Luck, J. Kneisel, K. Siemer, J. Bruns, R. Scheer, R. Klenk, N. Janke, and D. Bräunig, Sol. Energy Mater. Sol. Cells **67**, 151 (2001).

[25] J. Klaer, K. Siemer, I. Luck, and D. Bräunig, Thin Solid Films **387**, 169 (2001).

[26] Y. Onuma, K. Takeuchi, S. Ichikawa, M. Harada, H. Tanaka, A. Koizumi, and Y. Miyajima, Sol. Energy Mater. Sol. Cells **69**, 261 (2001).

[27] Y. Nagoya, K. Kushiya, M. Tachiyuki, and O. Yamase, Sol. Energy Mater. Sol. Cells **67**, 247 (2001).

[28] R. Scheer, T. Walter, H. W. Schock, M. L. Fearheiley, and H. J. Lewerenz, Appl. Phys. Lett. **63**, 3294 (1993).

[29] U. Rau, M. Schmidt, A. Jasenek, G. Hanna, and H. W. Schock, Sol. Energy Mater. Sol. Cells **67**, 137 (2001).

[30] G. Hanna, A. Jasenek, U. Rau, and H. W. Schock, Phys. Stat. Solidi (a) **179**, R7 (2000); G. Hanna, A. Jasenek, U. Rau, and H. W. Schock, Thin Solid Films **387**, 71 (2001).

[31] W. N. Shafarman, R. Klenk, and B. E. McCandless, J. Appl. Phys. **79**, 7324 (1996).

[32] F. H. Karg, Sol. Energy Mater. Sol. Cells **66**, 645 (2001).

[33] J. Klaer, I. Luck, K. Siemer, R. Klenk, and D. Bräunig, in *Proceedings of the 28th IEEE Photovoltaic Specialists Conference* (IEEE, New York, 2000), p. 559.

[34] R. Herberholz, V. Nadenau, U. Rühle, C. Köble, H. W. Schock, and B. Dimmler, Sol. Energy Mater. Sol. Cells **49**, 227 (1997).

[35] V. Nadenau, D. Hariskos, and H. W. Schock, *Proceedings of the 14th European Photovoltaic Solar Energy Conference*, edited by H. A. Ossenbrink, P. Helm, and H. Ehmann (H. S. Stephens & Assoc., Bedford, 1997), p. 1250.

[36] J. Klaer, J. Bruns, R. Henninger, K. Siemer, R. Klenk, K. Ellmer, and D. Bräunig, Semicond. Sci. Technol. **13**, 1456 (1998).

[37] K. Siemer, J. Klaer, I. Luck, J. Bruns, R. Klenk, and D. Bräunig, Sol. Energy Mater. Sol. Cells **67**, 159 (2001).

[38] R. Klenk, Thin Solid Films **387**, 135 (2001).

[39] J. Reiß, J. Malmström, A. Werner, I. Hengel, R. Klenk, and M. Ch. Lux-Steiner, Mat. Res. Soc. Symp. Proc. **668**, H9.4.1 (2001).

[40] J. Malmström, J. Wennerberg, M. Bodegård, and L. Stolt, *Proceedings of the 17th European Photovoltaic Solar Energy Conference 2001*, edited by B. McNelis, W. Palz, H. A. Ossenbrink, and P. Helm (WIP-Munich and ETA-Florence), p. 1265.

[41] G. Margaritondo, *Electronic Structure of Semiconductor Heterojunctions* (Kluwer, Lundon, 1988).

[42] H. Kroemer, J. Vac. Sci. Technol. B **2(3)**, 433 (1984).

[43] H. Kroemer, Surf. Science **132**, 543 (1983).

[44] H. Kroemer, Appl. Phys. Lett. **46**, 504 (1985).

[45] L. Y. Leu and S. R. Forrest, J. Appl. Phys. **65**, 4818 (1989).

[46] Y. H. Cho, B. D. Choe, and H. Lim, Appl. Phys. Lett. **69**, 3740 (1996).

[47] D. H. Chow, J. O. McCaldin, A. R. Bonnefoi, T. C. McGill, I. K. Sou, and J. P. Faurie, Appl. Phys. Lett. **51**, 2230 (1987).

[48] D. V. Lang, M. B. Panish, F. Capasso, J. Aliam, R. A. Hamm, A. M. Sergent, and W. T. Tsang, Appl. Phys. Lett. **50**, 736 (1987).

[49] D. V. Lang, A. M. Sergent, M. B. Panish, and H. Temkin, Appl. Phys. Lett. **49**, 812 (1986).

[50] G. Margaritondo, Surf. Science **132**, 469 (1983).

[51] E. A. Kraut, R. W. Grant, J. R. Waldrop, and S. P. Kowalczyk, Phys. Rev. Lett. **44**, 1620 (1980).

[52] G. Abstreiter, U. Prechtel, G. Weimann, and W. Schlapp, Physica B **134**, 433 (1985).

[53] M. Heiblum, M. I. Nathan, and M. Eizenberg, Appl. Phys. Lett. **47**, 503 (1985); M. Eizenberg, M. Heiblum, M. I. Nathan, N. Braslau, and P. M. Mooney, J. Appl. Phys **61**, 1516 (1987).

[54] C. L. Chang, L. P. Rokhinson, and J. C. Sturm, Appl. Phys. Lett. **73**, 3568 (1998).

[55] R. Dingle, W. Wiegmann, and C. H. Henry, Phys. Rev. Lett. **33**, 827 (1974).

[56] H. Temkin, M. B. Panish, P. M. Petroff, R. A. Hamm, J. M. Vandenberg, and S. Sumski, Appl. Phys. Lett. **47**, 394 (1985).

[57] J. L. Freeouf and J. M. Woodall, Surf. Science **168**, 518 (1986).

[58] J. M. Langer, C. Delerue, M. Lannoo, and H. Heinrich, Phys. Rev. B **38**, 7723 (1988).

[59] J. Tersoff, Phys. Rev. Lett. **52**, 465 (1984).

[60] J. Tersoff, Phys. Rev. B **30**, 4874 (1984).

[61] F. Flores and C. Tejedor, J. Phys. C: Solid State Phys. **12**, 230 (1979).

[62] J. Tersoff and W. A. Harrison, Phys. Rev. Lett. **58**, 2367 (1987).

[63] M. Cardona and N. E. Christensen, Phys. Rev. B **35**, 6182 (1987).

[64] I. Lefebre, M. Lannoo, C. Priester, G. Allan, and C. Delerue, Phys. Rev. B **36**, 1336 (1987).

[65] A. D. Katnani and G Margaritondo, Phys. Rev. B **28**, 1944 (1983).

[66] M. Turowski, G. Margaritondo, M. K. Kelly, and R. D. Tomlinson, Phys. Rev. B **31**, 1022 (1985).

[67] A. Bauknecht, U. Blieske, T. Kampschulte, J. Albert, H. Sehnert, M. Ch. Lux-Steiner, A. Klein, and W. Jaegermann, Appl. Phys. Lett. **74**, 1099 (1999).

[68] A. J. Nelson, C. R. Schwerdfeger, S. H. Wei, A. Zunger, D. Rioux, R. Patel, and H. Höchst, Appl. Phys. Lett. **62**, 2557 (1993).

[69] A. Klein, J. Fritsche, W. Jaegermann, J. H. Schön, Ch. Kloc, and E. Bucher, Appl. Surf. Science **166**, 508 (2000).

[70] M. Morkel, L. Weinhardt, B. Lohmüller, C. Heske, E. Umbach, W. Riedl, S. Zweigart, and F. Karg, Appl. Phys. Lett. **79**, 4482 (2001).

[71] A. Klein, T. Löher, Y. Tomm, C. Pettenkofer, and W. Jaegermann, Appl. Phys. Lett. **70**, 1299 (1997).

[72] S. M. Sze, *Physics of Semiconductor Devices*, (John Wiley & Sons, New York, 1981).

[73] S. H. Wei and A. Zunger, Appl. Phys. Lett. **63**, 2549 (1993).

[74] M. Sugiyama, H. Nakanishi, and S. F. Chichibu, Jpn. J. Appl. Phys. **40**, L428 (2001).

[75] R. K. Swank, Phys. Rev. 153, 844 (1967).

[76] M. J. Adam and A. Nussbaum, Solid State Electron. **22**, 783 (1979).

[77] O. von Ross, Solid State Electron. **23**, 1069 (1980).

[78] W. R. Frensley and H. Kroemer, Phys. Rev. B **16**, 2642 (1977).

[79] W. R. Frensley and H. Kroemer, J. Vac. Sci. Technol. **13**, 810 (1976).

[80] W. A. Harrison, J. Vac. Sci. Technol. **14**, 1016 (1977).

[81] W. A. Harrison, J. Vac. Sci. Technol. B **3(4)**, 1231 (1985).

[82] H. Flietner, Surf. Science **46**, 251 (1974).

[83] V. Heine, Phys. Rev. **138**, A1689 (1965).

[84] W. Mönch, *Semiconductor surfaces and interfaces* (Springer, Heidelberg, 2001).

[85] H. Flietner, Phys. Stat. Solidi (b) **54**, 201 (1972).

[86] J. Bardeen, Phys. Rev. **71**, 717 (1947).

[87] G. Margaritondo, Phys. Rev. B **31**, 2526 (1985).

[88] R. Hunger, Chr. Pettenkofer, and R. Scheer, J. Appl. Phys. **91**, 6560 (2002).

[89] S. Zott, K. Leo, M. Ruckh, and H. W. Schock, J. Appl. Phys. **82**, 356 (1997).

[90] K. Yoshino, T. Ikari, S. Shirakata, H. Miyake, and K. Hiramatsu, Appl. Phys. Lett. **78**, 742 (2001).

[91] R. Scheer, Jpn. J. Appl. Phys. **39**, Suppl. 39-1, 371 (2000).

[92] C. Tejedor and F. Flores, J. Phys. C: Solid State Phys. **11**, L19 (1978).

[93] C. Tejedor, F. Flores, and E. Louis, J. Phys. C: Solid State Phys. **10**, 2163 (1977).

[94] I. H. Choi and P. Y. Yu, Phys. Rev. B **55**, 9642 (1997).

[95] I. H. Choi and P. Y. Yu, Phys. Stat. Solidi (b) **211**, 143 (1999).

[96] L. M. Claessen, J. C. Maan, M. Altarelli, P. Wyder, L. L. Chang, and L Esaki, Phys. Rev. Lett. **57**, 2556 (1986).

[97] D. R. Penn, Phys. Rev. **128**, 2093 (1962).

[98] A. Anselm, *Introduction to semiconductor theory* (Mir Publishers, Moscow, 1981).

[99] W. Mönch, J. Appl. Phys. **80**, 5076 (1996).

[100] A. Baldereschi, Phys. Rev. B **7**, 5212 (1973).

[101] O. F. Sankey, R. E. Allen, S. F. Ren, and J. D. Dow, J. Vac. Sci. Technol. B **3(4)**, 1162 (1985).

[102] W. A. Harrison and J. Tersoff, J. Vac. Sci. Technol. B **4**, 1068 (1986).

[103] O. F. Sankey, R. E. Allen, and J. D. Dow, J. Vac. Sci. Technol. B **2(3)**, 491 (1984).

[104] A. Zunger, Phys. Rev. Lett. **54**, 849 (1985).

[105] J. M. Langer and H. Heinrich, Phys. Rev. Lett. **55**, 1414 (1985); J. M. Langer and H. Heinrich, Physica B **134**, 444 (1985).

[106] M. J. Caldas, A. Fazzio, and A. Zunger, Appl. Phys. Lett. **45**, 671 (1984).

[107] S. B. Zhang, S. H. Wei, and A. Zunger, J. Appl. Phys. **83**, 3192 (1998).

[108] J. Tersoff, Phys. Rev. Lett. **56**, 675 (1986).

[109] A. Mesli, P. Kringhøj, and A. Nylandsted Larsen, Phys. Rev. B **56**, 13202 (1997).

[110] M. Mamor, F. D. Auret, S. A. Goodman, and G. Myburg, Appl. Phys. Lett. **72**, 1069 (1998).

[111] P. N. Grillot and S. A. Ringel, Appl. Phys. Lett. **69**, 2110 (1996).

[112] P. Kringhøj and A. Nylandsted Larsen, Phys. Rev. B **52**, 16333 (1995).

[113] L. Samuelson, S. Nilsson, Z-G Wang, and H. G. Grimmeis, Phys. Rev. Lett. **53**, 1501 (1984).

[114] M. Zafar Iqbal, H. G. Grimmeis, and L. Samuelson, J. Phys. C: Solid State Phys. **18**, 1017 (1985).

[115] Qisheng Huang, H. G. Grimmeis, and L Samuelson, J. Phys. C: Solid State Phys. **18**, 5445 (1985).

[116] M. Sugawara, M. Kondo, T. Takanohashi, and K. Nakajima, Appl. Phys. Lett. **51**, 834 (1987).

[117] J. Baur, K. Maier, M. Kunzer, U. Kaufmann, and J. Schneider, Appl. Phys. Lett. **65**, 2211 (1994).

[118] A. Mycielski, P. Dzwonkowski, B. Kowalski, B. A. Orlowski, M. Dobrowolska, M. Arciszewska, W. Dobrowolski, and J. M. Baranowski, J. Phys. C: Solid State Phys. **19**, 3605 (1986).

[119] H. L. Park, Y. L. Lee, J. E. Kim, H. Y. Park, C. K. Choi, W. T. Kim, Jpn. J. Appl. Phys. **32**, Suppl. 32-3, 549 (1993); I. Hwang, N. Y. Lee, H. Kim, J. E. Kim, H. Y. Park, H. G. Kim, C. D. Kim, and W. T. Kim, Jpn. J. Appl. Phys. **32**, Suppl. 32-3, 552 (1993).

[120] S. K. Chang, H. L. Park, H. K. Kim, J. S. Hwang, C. H. Chung, and W. T. Kim, Phys. Stat. Solidi (b) **158**, K115 (1990).

[121] A. D. Katnani and R. S. Bauer, Phys. Rev. B **33**, 1106 (1986).

[122] T. M. Duc, C. Hsu, and J. P. Faurie, Phys. Rev. Lett. **58**, 1127 (1987).

[123] J. R. Waldrop and R. W. Grant, Phys. Rev. Lett. **43**, 1686 (1979).

[124] M. Ruckh, D. Schmid, and H. W. Schock, J. Appl. Phys. **76**, 5945 (1994).

[125] S. Chichibu, R. Sudo, N. Yoshida, Y. Harada, M. Uchida, S. Matsumoto, and H. Higuchi, Jpn. J. Appl. Phys. **33** (2), L286 (1994).

[126] J. Tersoff, Phys. Rev. Lett. **56**, 2755 (1986).

[127] D. W. Niles, E. Colavita, G. Margaritondo, P. Perfetti, C. Quaresima, and M. Capozi, J. Vac. Sci. Technol. A **4**, 962 (1986).

[128] P. Perfetti, C. Quaresima, C. Coluzza, C. Fortunato, and G. Margaritondo, Phys. Rev. Lett. **57**, 2065 (1986).

[129] D. W. Niles, M. Tang, G. Margaritondo, C. Quaresima, and P. Perfetti, J. Vac. Sci. Technol. A **6**, 1337 (1988).

[130] D. W. Niles, M. Tang, J. McKinley, R. Zanoni, and G. Margaritondo, Phys. Rev. B **38**, 10949 (1988).

[131] D. W. Niles, G. Margaritondo, P. Perfetti, C. Quaresima, and M. Capozi, Appl. Phys. Lett. **47**, 1092 (1985).

[132] Th. Gleim, C. Heske, E. Umbach, C. Schumacher, W. Faschinger, Ch. Ammon, M. Probst, and H. P. Steinrück, Appl. Phys. Lett. **78**, 1867 (2001).

[133] M Pan, S. P. Wilks, P. R. Dunstan, M. Pritchard, R. H. Williams, D. S. Cammack, and S. A. Clark, Appl. Phys. Lett. **72**, 2707 (1998).

[134] W. Mönch, Appl. Phys. Lett. **67**, 2209 (1995).

[135] W. Mönch, Phys. Rev. B **37**, 7129 (1988).

[136] W. Mönch, Phys. Rev. Lett. **58**, 1260 (1987).

[137] J. E. Jaffe and A. Zunger, Phys. Rev. B **28**, 5822 (1983).

[138] J. E. Jaffe and A. Zunger, Phys. Rev. B **29**, 1882 (1984).

[139] C. Lárez, C. Bellabarba, and C. Rincón, Appl. Phys. Lett. **65**, 1650 (1994).

[140] (a) J. J. M. Binsma, L. J. Giling, and J. Bloem, J. Luminescence **27**, 35 (1982); (b) J. J. M. Binsma, L. J. Giling, and J. Bloem, J. Luminescence **27**, 55 (1982).

[141] B. K. Meyer, M. Wagner, I. Dirnstorfer, D. M. Hofmann, F. Karg, Materials Science Forum **258-263**, 1467 (1997).

[142] I. H. Choi and P. Y. Yu, J. Phys. Chem. Solids **57**, 1695 (1996).

[143] E. I. Rogacheva, Cryst. Res. Technol. **1**, 1 (1996).

[144] T. Haalboom, T. Gödecke, F. Ernst, M. Rühle, R. Herberholz, H. W. Schock, C. Beilharz, and K. W. Benz, Inst. Phys. Conf. Ser. **152**, 249 (1998).

[145] R. Herberholz, H. W. Schock, U. Rau, J. H. Werner, T. Haalboom, T. Gödecke, F. Ernst, C. Beilharz, K. W. Benz, and D. Cahen, *Proceedings of the 26th IEEE Photovoltaic Specialists Conference* (IEEE, New York, 1998), p. 323.

[146] R. Herberholz, U. Rau, H. W. Schock, T. Haalboom, T. Gödecke, F. Ernst, C. Beilharz, K. W. Benz, and D. Cahen, Eur. Phys. J. AP **6**, 131 (1999).

[147] J. C. Mikkelsen, J. Electron. Mater. **10**, 541 (1981).

[148] J. J. Binsma, L. J. Giling, and J. Bloem, J. Cryst. Growth **50**, 429 (1980).

[149] S. Niki, Y. Makita, A. Yamada, A. Obara, S. Misawa, O. Igarashi. K. Aoki, and N. Kutsuwada, Jpn. J. Appl. Phys. **32**, 161 (1993); T. Matsumoto, Y. Miyaki, K. Kiuchi, and T. Kato, Jpn. J. Appl. Phys. **32**, 142 (1993).

[150] Ch. Hack, D. Wolf, and G. Müller, Inst. Phys. Conf. Ser. **152**, 285 (1998).

[151] Y. Tomm, S. Fischer, and C. Fisher, Inst. Phys. Conf. Ser. **152**, 181 (1998); L Roa, P

Grima, J. Gonzalez, J. C. Chervin, J. P. Itie, and A. Chevy, Cryst. Res. Technol. **31**, 49 (1996).

[152] N. Yamamoto, Y. Kikuno, M. Yamaguchi, and K. Wakita, Inst. Phys. Conf. Ser. **152**, 71 (1998); V. Lyahovitskaya, S. Richter, Y. Manassen, and D. Cahen, Inst. Phys. Conf. Ser. **152**, 103 (1998); H. Miyake and K Sugiyama, Jpn. J. Appl. Phys. **32**, 156 (1993).

[153] M. Hornung, K. W. Benz, L. Margulis, D. Schmid, and H. W. Schock, J. Cryst. Growth **154**, 315 (1995); Z. A. Shukri, C. H. Champness, and I. Shih, J. Cryst. Growth **129**, 107 (1993); H. Matsushita, A. Iwabuchi, T. Takizawa, and S. Endo, Cryst. Res. Technol. **31**, 77 (1996).

[154] A. Rockett and R. W. Birkmire, J. Appl. Phys. **70**, R81 (1991).

[155] R. Klenk, T. Walter, D. Schmid, and H. W. Schock, Jpn. J. Appl. Phys. **32**, 57 (1993).

[156] S. Zweigart, D. Schmid, J. Kessler, H. Dittrich, and H. W. Schock, J. Cryst. Growth **146**, 233 (1995).

[157] T. Nakada, K. Migita, and A. Kunioka, Jpn. J. Appl. Phys. **32**, 48 (1993).

[158] J. Levoska, A. E. Hill, S. Leppävuori, O. Kusmartseva, R. D. Tomlinson, and R. D. Pilkington, Jpn. J. Appl. Phys. **32**, 43 (1993).

[159] J. Vedel, Inst. Phys. Conf. Ser. **152**, 261 (1998).

[160] T. Murakami, S. Shirakata, and S. Isomura, Jpn. J. Appl. Phys. **32**, 71 (1993).

[161] C. Eberspracher, C. Fredric, K. Pauls, and J. Serra, Thin Solid Films, **387**, 18 (2001); B. M. Başol, Thin Solid Films, **361-362**, 514 (2000).

[162] M. R. Balboul, U. Rau, G. Bilger, M. Schmidt, H. W. Schock, and J. H. Werner, J. Vac. Sci. Techn. A **20**, 1247 (2002).

[163] V. Nadenau, G. Lippolt, U. Rau, and H. W. Schock, J. Crystal Growth **233**, 13 (2001).

[164] K. Fukuzaki, S. Kohiki, H. Yoshikawa, S. Fukushima, T. Watanabe, and I. Kojima, Appl. Phys. Lett. **73**, 1385 (1998).

[165] R. Klenk, T. Walter, H. W. Schock, and D. Cahen, Polycrystalline Semiconductors: Solid State Phenomena **37-38**, 509 (1994).

[166] T. Walter, A. Content, K. O. Velthaus, and H. W. Schock, Sol. Energy Mater. Sol. Cells **26**, 357 (1992).

[167] R. Klenk, T. Walter, H. W. Schock, and D. Cahen, Advanced Materials **5**,114 (1993).

[168] R. A. Mickelsen and W. S. Chen, Appl. Phys. Lett. **36**, 371 (1980).

[169] J. Kessler, D. Schmid, S. Zweigart, H. Dittrich, and H. W. Schock, *Proceeding of the 12th European Photovoltaic Solar Energy Conference*, edited by R. Hill, W. Palz, and

P. Helm (Stephens, Bedford, 1994), p. 648.

[170] A. M. Gabor, J. R. Tuttle, D. S. Albin, M. A. Contreras, R. Noufi, and A. M. Hermann, Appl. Phys. Lett. **65**, 198 (1994).

[171] S. B. Zhang, S. H. Wei, A. Zunger, and H. Katayama-Yoshida, Phys. Rev. B **57**, 9642 (1998).

[172] A. A. Rockett, F. Abou-Elfotouh, D. Albin, M. Bode, J. Ermer, R. Klenk, T. Lommasson, T. W. F. Russell, R. D. Tomlinson, J. Tuttle, L. Stolt, T. Walter, and T. M. Peterson, Thin Solid Films **237**, 1 (1994).

[173] P. Migliorato, J. L. Shay, H. M. Kasper, and S. Wagner, J. Appl. Phys. **46**, 1777 (1975).

[174] R. Noufi, R. Axton, C. Herrington, and S. K. Deb, Appl. Phys. Lett. **45**, 668 (1984).

[175] S. B. Zhang, S. H. Wei, and A. Zunger, Phys. Rev. Lett. **78**, 4059 (1997).

[176] S. H. Wei, S. B. Zhang, and A. Zunger, Appl. Phys. Lett. **72**, 3199 (1998).

[177] S. H. Wei, S. B. Zhang, and A. Zunger, J. Appl. Phys. **85**, 7214 (1999).

[178] T. Yamamoto and H. Katayama-Yoshida, Sol. Energy Mater. Sol. Cells **49**, 391 (1997).

[179] T. Yamamoto and H. Katayama-Yoshida, Cryst. Res. Technol. **31**, 97 (1996).

[180] L. Stolt, J. Hedström, J. Kessler, M. Ruckh, K. O. Velthaus, and H. W. Schock, Appl. Phys. Lett. **62**,597 (1993).

[181] M. Bodegård, K. Granath, and L. Stolt, Thin Solid Films **361-362**, 9 (2000).

[182] D. J. Schroeder and A. A. Rockett, J. Appl. Phys. **82**, 4982 (1997).

[183] U. Rau, M. Schmitt, F. Engelhardt, O. Seifert, J. Parisi, W. Riedl, J. Rimmasch, and F. Karg, Solid State Commun. **107**, 59 (1998).

[184] D. Braunger, D. Hariskos, G. Bilger, U. Rau, and H. W. Schock, Thin Solid Films **361-362**, 161(2000).

[185] L. Kronik, D. Cahen, and H. W. Schock, Adv. Mater. **10**, 31 (1998).

[186] V. Lyahovitskaya, Y. Feldman, K. Gartsman, H. Cohen, C. Cytermann, and D. Cahen, J. Appl. Phys. **91**, 4205 (2002).

[187] S. Ashour, S. Alkuhaimi, H. Moutinho, R. Matson, and F. Abou-Elfotouh, Thin Solid Films **226**, 129 (1993).

[188] R. Takei, H. Tanino, S. Chichibu, and H. Nakanishi, J. Appl. Phys. **79**, 2793 (1996).

[189] T. Wada, N. Kohara, S. Nishiwaki, and T. Negami, Thin Solid Films **387**, 118 (2001).

[190] U. Rau, Jpn. J. Appl. Phys. **39**, Suppl. 39-1, 389 (2000).

[191] T. Nakada and A. Kunioka, Appl. Phys. Lett. **74**, 2444 (1999).

[192] C. Heske, D. Eich, R. Fink, E. Umbach, T. van Buuren, C. Bostedt, L. J. Terminello, S.

Kakar, M. M. Grush, T. A. Calcott, F. J. Himpsel, D. L. Ederer, R. C. C. Perera, W. Riedl, and F. Karg, Appl. Phys. Lett. **74**, 1451 (1999).

[193] T. Nakada and M. Mizutani, Jpn. J. Appl. Phys. **41**, L165 (2002).

[194] D. Braunger, D. Hariskos, T. Walter, and H. W. Schock, Sol. Energy Mater. Sol. Cells **40**, 97 (1996).

[195] Y. Ohtake, T. Okamoto, A. Yamada, M. Konagai, and K. Saito, Sol. Energy Mater. Sol. Cells **49**, 269 (1997).

[196] A. Shimizu, S. Chaisitsak, T. Sugiyama, A. Yamada, and M. Konagai, Thin Solid Films **361-362**, 193 (2000).

[197] R. Schäffler and H. W. Schock, *Proceedings of the 23rd IEEE Photovoltaic Specialists Conference* (IEEE, New York, 1993), p. 1026.

[198] L. Kronik, L. Burstein, M. Leibovitch, Y. Shapira, D. Gal, E. Moons, G. Hodes, D. Cahen, D. Hariskos, R. Klenk, and H. W. Schock, Appl. Phys. Lett. **67**, 1405 (1995).

[199] A. Niemegeers, M. Burgelman, R. Herberholz, U. Rau, D. Hariskos, and H. W. Schock, Prog. Photovoltaics: Res. Appl. **6**, 407 (1998).

[200] D. Schmid, M. Ruckh, and H. W. Schock, Sol. Energy Mater. Sol. Cells **41/42**, 281 (1996).

[201] D. Schmid, M. Ruckh, F. Grunwald, and H. W. Schock, J. Appl. Phys. **73**, 2902 (1993).

[202] D. Schmid, M. Ruckh, and H. W. Schock, Appl. Surf. Science, **103**, 409 (1996).

[203] D. Cahen and R. Noufi, Appl. Phys. Lett. **54**, 558 (1989).

[204] K. Otte, T. Chassé, G. Lippold, B. Rauschenbach, and R. Szargan, J. Appl. Phys. **91**, 1624 (2002).

[205] U. Rau, D. Braunger, R. Herberholz, H. W. Schock, J. F. Guillemoles, L. Kronik, and D. Cahen, J. Appl. Phys. **86**, 497 (1999).

[206] A. Klein and W. Jaegermann, Appl. Phys. Lett. **74**, 2283 (1999).

[207] A set of absorbers (including samples with compositional gradient in the depth), the respective preparation and energy dispersive X-ray compositional data, and complete heterojunction devices together with the measured standard device parameters are provided by I. M. Kötschau.

[208] S. Klein, Diploma Thesis, University of Stuttgart (1999), p. 28.

[209] D. Bäder, Student Research Project, University of Stuttgart (2000), p. 11.

[210] R. Herberholz, PhD Thesis, University of Stuttgart (1998), p.25.

[211] J. I. Pankove, *Optical processes in semiconductors* (Dover Publications, New York, 1975).

[212] A. Bauknecht, S. Siebentritt, J. Albert, and M. Ch. Lux-Steiner, J. Appl. Phys. **89**, 4391 (2001).

[213] M. Wagner, I. Dirnstorfer, D. M. Hofmann, M. D. Lampert, F. Karg, and B. K. Meyer, Phys. Stat. Solidi (a) **167**, 131 (1998).

[214] K. Zeaiter, Y. Llinares, and C. Llinarès, Sol. Energy Mater. Sol. Cells **61**, 313 (2000).

[215] J. H. Schön, Ch. Kloc, and E. Bucher, Thin Solid Films **361-362**, 411 (2000).

[216] J. R. Botha, M. S. Branch, A. G. Chowles, A. W. R. Leitch, and J. Weber, Physica B **308-310**, 1065 (2001).

[217] I. Aksenov, T. Kai, N. Nishikawa, and K. Sato, Jpn. J. Appl. Phys. **32**, Suppl. 32-3, 153 (1993).

[218] T. Schmidt, K. Lishka, and W. Zulehner, Phys. Rev. B **45**, 8989 (1992).

[219] S. Zott, K. Leo, M. Ruckh, and H. W. Schock, Appl. Phys. Lett. **68**, 1144 (1996).

[220] I. Dirnstorfer, M. Wagner, D. M. Hofmann, M. D. Lampert, F. Karg, and B. K. Meyer, Phys. Stat. Solidi (a) **168**, 163 (1998).

[221] G. A. Medvedkin and M. A. Magomedov, J. Appl. Phys. **82**, 4013 (1997).

[222] F. Schlicht, W. Stadler, D. Kovalev, B. K. Meyer, R. Krause-Rehberg, A. Polity, T. Staab, M. Hornung, K. W. Benz, and Ch. Kloc, Cryst. Res. Technol. **31**, 745 (1996).

[223] H. Miyake and K. Sugiyama, J. Appl. Phys. **72**, 3697 (1992).

[224] R. Bacewicz and M. Igalson, Cryst. Res. Technol. **31**, 725 (1996).

[225] U. Fiedeler, J. Albert, S. Siebentritt, and M. Ch. Lux-Steiner, *Proceedings of the 17th European Photovoltaic Solar Energy Conference 2001*, edited by B. McNelis, W. Palz, H. A. Ossenbrink, and P. Helm (WIP-Munich and ETA-Florence), p. 1143.

[226] T. Kurafuji, S. Niki, H. Shibata, P. J. Fons, A. Yamada, Y. Makita, S. Chichibu, and H. Nakanishi, Cryst. Res. Technol. **31**, 709 (1996).

[227] S. Zott, K. Leo, M. Ruckh, and H. W. Schock, Cryst. Res. Technol. **31**, 729 (1996).

[228] P. W. Yu, J. Appl. Phys. **47**, 677 (1976).

[229] J. H. Schön, O. Schenker, H. Riazi-Nejad, K. Friemelt, Ch. Kloc, and E. Bucher, Phys. Stat. Solidi (a) **161**, 301 (1997).

[230] B. Eisener, D. Wolf, and G. Müller, Thin Solid Films **361-362**, 126 (2000).

[231] S. Shirakata, S. Chichibu, and S. Isomura, Cryst. Res. Technol. **31**, 717 (1996).

[232] R. C. C. Leite and A. E. DiGiovanni, Phys. Rev. **153**, 841 (1967).

[233] T. Walter, R. Herberholz, C. Müller, and H. W. Schock, J. Appl. Phys. **80**, 4411 (1996).

[234] R. Herberholz, M. Igalson, and H. W. Schock, J. Appl. Phys. **83**, 318 (1998).

[235] J. Kneisel, K. Siemer, I. Luck, and D. Bräunig, J. Appl. Phys. **88**, 5474 (2000).

[236] Admittance spectroscopy data corresponding to reference heterojunctions based on $CuInSe_2$ material and on $Cu(In_{1-x}Ga_x)Se_2$ alloys with different x ratios, as well as the respective absorber band gap energies are provided by G. Hanna.

[237] M. Igalson and H. W. Schock, J. Appl. Phys. **80**, 5765 (1996).

[238] A. Jasenek, U. Rau, V. Nadenau, and H. W. Schock, J. Appl. Phys. **87**, 594 (2000).

[239] K. Siemer, J. Klaer, I. Luck, and D. Bräunig, Thin Solid Films **387**, 222 (2001).

[240] S. H. Wei and A. Zunger, J. Appl. Phys. **78**, 3846 (1995).

[241] J. O. McCaldin, T. C. McGill, and C. A. Mead, Phys. Rev. Lett. **36**, 56 (1976).

[242] S. H. Wei and A. Zunger, Phys. Rev. B **37**, 8958 (1988).

[243] M. W. Wang, J. F. Swenberg, M. C. Phillips, E. T. Yu, J. O. McCaldin, R. W. Grant, and T. C. McGill, Appl. Phys. Lett. **64**, 3455 (1994).

[244] D. G. Kilday, G. Margaritondo, T. F. Ciszek, S. K. Deb, S. H. Wei, and A. Zunger, Phys. Rev. B. **36**, 9388 (1987).

[245] M. Mamor, unpublished.

[246] I. V. Bodnar, B. V. Korzun, and A. I. Lukomskii, Phys. Stat. Solidi (b) **105**, K143 (1981).

[247] W. S. Chen, J. M. Stewart, B. J. Stanbery, *Proceedings of the 19th IEEE Photovoltaic Specialists Conference* (IEEE, New York, 1987), p. 1445.

[248] B. Dimmler, H. Dittrich, R. Menner, and H. W. Schock, *Proceedings of the 19th IEEE Photovoltaic Specialists Conference* (IEEE, New York, 1987), p. 1454.

[249] E. F. Schubert, E. O. Göbel, Y. Horikoshi, K. Ploog, and H. J. Queisser, Phys. Rev. B **30**, 813 (1984).

[250] P. Ommling, L. Samuelson, and H. G. Grimmeis, J. Appl. Phys. **54**, 5117 (1983).

[251] J. Weber and M. I. Alonso, Phys. Rev. B **40**, 5683 (1989).

[252] G. S. Mitchard and T. C. McGill, Phys. Rev. B **25**, 5353 (1982).

[253] C. Delerue, M. Lannoo, and J. M. Langer, Phys. Rev. Lett. **61**, 199 (1988).

[254] Fruitful information on the theoretical model of calculation kindly provided by K. Taretto is acknowledged.

[255] V. Nadenau, U. Rau, A. Jasenek, and H. W. Schock, J. Appl. Phys. **87**, 584 (2000).

[256] U. Rau, Appl. Phys. Lett. **74**, 111 (1999).

[257] The evaluation of capacitance-voltage data (Section 7.2.3) as well as substantial help in performing the current-voltage, capacitance-voltage, and quantum efficiency measurements provided by O. Pakma are acknowledged.

[258] I. Hengel, A. Neisser, R. Klenk, and M. Ch. Lux-Steiner, Thin Solid Films **361-362**, 458 (2000).

[259] T. Dullweber, G. Hanna, U. Rau, and H. W. Schock, Sol. Energy Mater. Sol. Cells **67**, 145 (2001).

[260] H. W. Schock and U. Rau, Physica B **308-310**, 1081 (2001).

[261] T. Dullweber, G. Hanna, W. Shams-Kolahi, A. Schwartzlander, M. A. Contreras, R. Noufi, and H. W. Schock, Thin Solid Films **361-362**, 478 (2000).

[262] M. S. Jin, W. T. Kim, and C. S. Yoon, J. Phys. Chem. Solids **54**, 1509 (1993).

[263] G. Sánchez Porras and S. M. Wasim, Phys. Stat. Solidi (a) **133**, 509 (1992).

[264] K. Sato, M. Isawa, N. Takahashi, and H. Tsunoda, Jpn. J. Appl. Phys. **27**, 1359 (1988).

[265] C. Rincon and S. M. Wasim, in Ternary and Multinary Compounds, edited by S. K. Deb and A. Zunger (Material Research Society, Pittsburg, 1987), p. 443.

[266] K. Sato, H. Tsunoda, and T. Teranishi, in Ternary and Multinary Compounds, edited by S. K. Deb and A. Zunger (Material Research Society, Pittsburg, 1987), p. 459.

[267] J. T. Heath, J. D. Cohen, W. N. Shafarman, D. X. Liao, and A. A. Rockett, Appl. Phys. Lett. **80**, 4540 (2002).

[268] S. B. Zhang, S. H. Wei, and A. Zunger, Phys. Rev. Lett. **84**, 1232 (2000).

[269] A. L. Li and I. Shih, J. Electron. Mat. **22**, 195 (1993).

[270] (a) A. Opanowicz, and B. Kościelniak-Mucha, Acta Phys. Pol. A **75**, 289 (1989); (b) B. Kościelniak-Mucha and A. Opanowicz, Phys. Stat. Solidi (a) **141**, K67 (1994); (c) B. Kościelniak-Mucha and A. Opanowicz, Phys. Stat. Solidi (a) **130**, K55 (1992).

[271] F. Leccabue, D. Seuret, and O. Vigil, Appl. Phys. Lett. **46**, 853 (1985).

[272] A. J. Nelson, S. Gebhard, L. L. Kazmerski, E. Colavita, M. Engelhardt, and H. Höchst, J. Vac. Sci. Technol. A **9**, 978 (1991).

[273] C. L. Chan and I. Shih, J. Appl. Phys. **68**, 156 (1990).

[274] D. W. Niles, A. J. Nelson, C. R. Schwerdtfeger, H. Höchst, and D. Rioux, Mat. Res. Soc. Symp. Proc. **260**, 299 (1992).

[275] I. Shih, C. X. Qiu, S. N. Qiu, and J. F. Huang, J. Appl. Phys. **63**, 439 (1988).

[276] N. Ishibashi, T. Nishi, N. Hayashi, C. Furuhashi, and K. Sato, Jpn. J. Appl. Phys. **38**, L626 (1999).

[277] A. Jasenek, U. Rau, V. Nadenau, D. Thiess, and H. W. Schock, Thin Solid Films **361-362**, 415 (2000).

[278] A. A. Rockett, Thin Solid Films, **361-362**, 330 (2000).

[279] F. Engelhardt, L. Bornemann, M. Köntges, Th. Meyer, J. Parisi, E. Pschorr-Schoberer, B. Hahn, W. Gebhardt, W. Riedl, and U. Rau, Prog. Photovoltaics: Res. Appl. **7**, 423 (1999).

[280] T. A. Magorian Friedlmeier, PhD Thesis, University of Stuttgart (2001), p. 62.

[281] J. Parisi, D. Hilburger, M. Schmitt, and U. Rau, Sol. Energy Mater. Sol. Cells **50**, 79 (1998).

[282] J. Kessler, D. Schmid, R. Schäffler, H. W. Schock, S. Menezes, *Proceedings of the 23rd IEEE Photovoltaic Specialists Conference* (IEEE, New York, 1993), p. 549.

[283] (a) M. Turcu, I. M. Kötschau, and U. Rau, Appl. Phys. A: Mater. Sci. Process. **73**, 769 (2001); (b) M. Turcu, I. M. Kötschau, and U. Rau, J. Appl. Phys. **91**, 1391 (2002); (c) M. Turcu, O. Pakma, and U. Rau, Appl. Phys. Lett. **80**, 2598 (2002); (d) M. Turcu and U. Rau, Thin Solid Films **431-432**, 158 (2003); (e) see also M. Turcu and U. Rau, J. Phys. Chem. Solids, in print (2003), which, besides additional theoretical considerations, presents again the experimental results of (c) this reference.

Versicherung

Hiermit versichere ich, dass ich die vorliegende Arbeit ohne unzulässige Hilfe Dritter und ohne Benutzung anderer als der angegebenen Hilfsmittel angefertigt habe; die aus fremden Quellen direkt oder indirekt übernommenen Gedanken sind als solche kenntlich gemacht. Die Arbeit wurde bisher weder im Inland noch im Ausland in gleicher oder ähnlicher Form einer anderen Prüfungsbehörde vorgelegt.

Diese Arbeit wurde am Institut für Physikalische Elektronik der Universität Stuttgart unter der wissenschaftlichen Betreuung von Dr. Uwe Rau (Universität Stuttgart) und Prof. Dr. Karl Leo (Technische Universität Dresden) angefertigt.

Stuttgart, den 01.09.2003

(Mircea Cassian Turcu)